



ISSN 1343-2230

CNS-REP-102
March, 2024

Annual Report 2022

Center for Nuclear Study,
Graduate School of Science, the University of Tokyo

Editors

Noritaka Kitamura

Hiroki Nagahama

Shin'ichiro Michimasa

Center for Nuclear Study

CNS Reports are available from:

Wako-Branch at RIKEN

Center for Nuclear Study,

Graduate School of Science, the University of Tokyo

2-1 Hirosawa, Wako

351-0198, Japan

Tel: +81-48-464-4191

Fax: +81-48-464-4554

Annual Report 2022

Center for Nuclear Study,
Graduate School of Science, the University of Tokyo

Preface

This is the annual report of the Center for Nuclear Study (CNS), Graduate School of Science, the University of Tokyo, for the fiscal year 2022 (April 2022 through March 2023). During this period, a lot of research activities in various fields of nuclear physics have been carried out and a wide variety of fruitful results have been obtained at CNS. This report summarizes such research activities. I hereby mention some highlights of the report.

The Center for Nuclear Study (CNS) aims to elucidate the nature of nuclear system by producing the characteristic states where the Isospin, Spin and Quark degrees of freedom play central roles. These researches in CNS lead to the understanding of the matter based on common natures of many-body systems in various phases. We also aim at elucidating the explosion phenomena and the evolution of the universe by the direct measurements simulating nuclear reactions in the universe. In order to advance the nuclear science with heavy-ion reactions, we develop ECR ion source, CRIB and SHARAQ facilities in the large-scale accelerators laboratories RIBF. The OEDO facility has been developed as an upgrade of the SHARAQ, where a RF deflector system has been introduced to obtain a good quality of low-energy beam. A new project for fundamental symmetry using heavy RIs has been starting to install new experimental devices in the RIBF. We promote collaboration programs at RIBF as well as RHIC-PHENIX and ALICE-LHC with scientists in the world, and host international meetings and conferences. We also provide educational opportunities to young scientists in the heavy-ion science through the graduate course as a member of the department of physics in the University of Tokyo and through hosting the international summer school.

The Low Energy Nuclear Reaction group studies exotic structures in high-isospin and/or high-spin states in nuclei. In the spring of 2022, two nuclear reactions, $^{130}\text{Sn}(d, p)$ and $^{56}\text{Ni}(d, p)$, SHARAQ18 and 19, respectively, were performed at the OEDO-SHARAQ system in inverse kinematics by employing the surrogate technique, where the decay channels of the unbound states were identified directly from the measurement of reaction residues. Prior to the SHARAQ18, MS22-01 was carried out to establish a new optics for transporting the ion beam with better transmission. In winter 2022, another OEDO experiment, SHARAQ12, for the single particle structure in ^{51}Ca was partially performed. The analyses of the experiments, ImPACT17-02-01, -02, and SHARAQ11, $^4\text{He}(^8\text{He}, ^8\text{Be})4n$ reaction, are in progress. The analysis of the groundbreaking experiment on the inelastic decay from the isobaric analog resonances is almost finished. The CNS GRAPE (Gamma-Ray detector Array with Position and Energy sensitivity) is a major instrument for high-resolution in-beam gamma-ray spectroscopy. The digital signal processing equipment for the GRAPE is under development.

The Exotic Nuclear Reaction group studies various exotic reactions induced by heavy-ion beams. We proceeded with the data reduction of the double charge exchange ($^{12}\text{C}, ^{12}\text{Be}$) reaction taken in the previous year for a search of double Gamow-Teller resonance.

The OEDO/SHARAQ group pursues experimental studies with RI beams by using the high-resolution beamline and the SHARAQ spectrometer, and the OEDO for the decelerated RI beams. The uniqueness of the OEDO-SHARAQ system is its versatile performance in low-energy RI production and high-resolution spectroscopy. In FY2022, taking advantage of this feature, two low-energy RI experiments for (d, p) -type surrogate reactions and a high-resolution direct mass measurement for two-proton radioactivity were performed. Through the measurements, we were able to demonstrate a smooth re-arrangement of the beamline and experimental detector setups. In addition, we installed an active stopper detector and γ -ray detectors for the in-flight isomeric tagging of exotic nuclei in the mass measurement program. Data analysis of performed experiments is ongoing. The experimental study of 0^- strength in nuclei using the parity-transfer charge exchange ($^{16}\text{O}, ^{16}\text{F}$) is in the final stage. The results of the first and second experiments with the OEDO system for LLFPs will be completed and reported soon.

The main activity of the nuclear astrophysics group is to study astrophysical reactions and special

nuclear structure, such as clusters, using the low-energy RI beam separator CRIB. In Oct. 2022, a ${}^6\text{He}$ radioactive beam was produced for the second time at CRIB, with improved beam intensity and purity by introducing wire chambers (MWDC) and a degrader. In Mar 2023, we performed a direct measurement of astrophysical ${}^{14}\text{O}(\alpha, p)$ reaction in an international collaboration with the groups in IBS (Korea), Texas A&M University (US) and others. An active-target system developed in Texas (TexAT) was brought to Japan to perform this measurement with the thick-target method using the ${}^{14}\text{O}$ radioactive beam at CRIB. This was the first experiment at CRIB with participants from foreign countries after the pandemic.

Main goal of the quark physics group is to understand the properties of hot and dense nuclear matter created by colliding heavy nuclei at relativistic energies. The group has been involved in the PHENIX experiment at Relativistic Heavy Ion Collider (RHIC) at Brookhaven National Laboratory, and the ALICE experiment at Large Hadron Collider (LHC) at CERN. As for ALICE, the group has involved in the data analyses, which include the measurement of low-mass lepton pairs in Pb-Pb collisions, the measurement of long range two particle correlations in p-Pb collisions, searches for thermal photons in high multiplicity pp collisions. The group has involved in the ALICE-TPC upgrade using a Gas Electron Multiplier (GEM), where the group is very active in the development and benchmarking of the online space-charge distortion corrections using machine learning techniques running on the Graphical Processing Unit (GPU). The group has started simulation studies for the ALICE 3 future upgrade.

One of the major tasks of the accelerator group is the development of ion sources and the optimization of the beam transport system for the experimental devices installed in the E7 experiment room. In 2022, HyperECR ion source was operated for 2,151 hours. A new method for sustainable magnesium beam production was put into practical use for CRIB. The ${}^{24}\text{Mg}^{8+}$ beam was successfully produced for 18 days with four breaks to refill the sample crucible. In a university-industry collaboration, a magnetic design for a new ECR ion source was proposed for industrial applications. For the development of the pepper-pot emittance monitor to diagnose the beam extracted from AVF cyclotron, an optical system with a digital camera was completed. Then, the required angular accuracy was estimated to be less than 0.3 mrad. The beam test for the prototype was planned and the preparation was started.

The development of the quantum sensor to search for a permanent electric dipole moment (EDM) with an optical lattice interferometer is in progress at RIKEN. The RF filter was newly developed and installed to the beam transport system to obtain the secondary beam of the Fr ion with a high purity, which was used to improve the trapping efficiency of the magneto-optical trap. The parameter tuning to get high intensity cold Fr atoms in the MOT is continued. Furthermore, a homemade Yb-doped fiber amplifier (YDFA) is developed, required to generate a deep optical lattice potential that would enable a long interrogation time for the EDM measurement.

The nuclear theory group is conducting large-scale shell-model calculations, having a strong relationship to the project “Program for Promoting Researches on the Supercomputer Fugaku”. One of the key achievements in FY2022 is finding the mechanism of the strongly hindered $E0$ transition from the superdeformed 0^+ state to the ground state in ${}^{40}\text{Ca}$. We are also performing shell-model calculations for the structure of neutron-rich nuclei in collaboration with experiments carried out in RIBF, RIKEN, focusing on the region around ${}^{54}\text{Ca}$. Another important direction of our activity is application to the fundamental physics. In this year, we have found that the nuclear Schiff moment is strongly correlated to nuclear magnetic moments, which enables providing reliable Schiff moments in comparison to existing data.

The 21st CNS International Summer School (A3F-CNSSS22) was held from August 20th to 24th, 2022. The school was organized by CNS in collaboration with the JSPS A3F program and the Super Heavy Element Center at Kyushu University. We shifted to a hybrid format following previous online editions. The event, relocated to Shinrin-koen Heritage Resort, featured 8 lecturers and a total of

99 attendees, including 51 on-site participants and online attendees from Malaysia, Vietnam, Korea, China, and India. We also welcomed participants from Oslo University for the first time.

Finally, I thank Ms. Shimane and other administrative staff members for their contributions throughout the year.

Yasuhiro Sakemi

Director of CNS

A handwritten signature in black ink, reading "Yasuhiro Sakemi". The signature is written in a cursive style with a prominent initial 'Y' and 'S'.

Table of Contents

1a. Experimental Nuclear Physics: Low and Intermediate Energies

Data Analysis of OEDO day-0 Experiment Measuring $^{93}\text{Zr} + d$ Transmutation Reactions for the Study of Deuteron Breakup	1
<i>T. Chillery, J. W. Hwang, M. Dozono, N. Imai, S. Michimasa, T. Sumikama, N. Chiga, S. Ota, S. Nakayama</i>	
Surrogate reaction of $^{130}\text{Sn}(n, \gamma)$ at OEDO	3
<i>N. Imai, S. Michimasa, T. Chillery, D. Suzuki, D.S. Ahn, A. Chae, S. Cherubini, M. La Cognata, M. Dozono, M. Egeta, F. Endo, N. Fukuda, T. Haginouchi, S. Hanai, S. Hayakawa, J.W. Hwang, Y. Hijikata, S. Ishio, N. Iwasa, K. Kawata, S. Kubono, R. Kojima, L. Lamia, J. Li, N. Nishimura, K. Okawa, H.J. Ong, S. Ota, S. Palmerini, R.G. Pizzone, T. Saito, Y. Shimizu, S. Shimoura, T. Sumikama, H. Suzuki, H. Takeda, A. Tumino, X. Tang, H. Tanaka, M. Tanaka, T. Teranishi, Y. Togano, R. Yokoyama, R. Yoshida, K. Yoshida, M. Yoshitomo, Y. Wang, Z. Xiao</i>	
Report on OEDO-SHARAQ experiments in FY 2022	5
<i>S. Michimasa, T. Chillery, N. Imai, R. Yokoyama, N. Kitamura, S. Hanai, R. Kojima, J. W. Hwang, T. Sumikama, M. Dozono, S. Ota, D. S. Ahn, Y. Hijikata, K. Kawata, K. Kusaka, J. Li, M. Ohtake, D. Suzuki, H. Suzuki, H. Takeda, K. Yako, Y. Yanagisawa, K. Yoshida, M. Yoshimoto, S. Shimoura</i>	
Study of νp -process nucleosynthesis at OEDO	7
<i>D. Suzuki, B. Mauss, N. Imai, S. Michimasa, D. Beaumel, K.Y. Chae, S. Cherubini, T. Chillery, M. Dozono, M. Egeta, F. Endo, N. Fukuda, T. Haginouchi, S. Hanai, S. Hayakawa, Y. Hijikata, J.W. Hwang, S. Ishio, N. Iwasa, S. Kawase, K. Kawata, R. Kojima, S. Kubono, M. La Cognata, J. Li, N. Nishimura, K. Okawa, M. Oishi, H.J. Ong, S. Ota, S. Palmerini, R. Pizzone, T. Saito, H. Sakurai, S. Shimoura, Y. Shimizu, T. Sumikama, H. Suzuki, H. Takeda, H. Tanaka, M. Tanaka, X. Tang, T. Teranishi, Y. Togano, A. Tunimo, Y. Wang, K. Yako, K. Yahiro, H. Yamaguchi, R. Yokoyama, K. Yoshida, R. Yoshida, M. Yoshimoto</i>	
Half-life measurement of 107-keV isomeric state in ^{45}Cr	9
<i>M. Amitani, Y. Nakamura, C. Fukushima, T. Tomiyama, S. Hanai, K. Kawata, S. Michimasa, D. Nishimura, K. Okawa, T.Y. Saito, R. Yokoyama, D.S. Ahn, H. Baba, T. Chillery, M. Dozono, F. Endo, M. Fukuda, N. Fukuda, M. Fukutome, T. Haginouchi, S. Hayakawa, Y. Hijikata, J. W. Hwang, E. Ideguchi, N. Imai, S. Ishio, N. Iwasa, K. Kameya, R. Kojima, K. Kusaka, J. Li, H. Nishibata, S. Ota, D. Suzuki, H. Suzuki, Y. Shimizu, S. Shimoura, T. Sumikama, H. Takahashi, H. Takeda, H. Tanaka, M. Tanaka, T. Teranishi, T. Uesaka, R. Urayama, K. Yako, Y. Yanagisawa, K. Yoshida, M. Yoshimoto</i>	
Direct mass measurement of proton-rich Fe isotopes	11
<i>S. Hanai, S. Michimasa, N. Imai, R. Yokoyama, D.S. Ahn, M. Amitani, H. Baba, T. Chillery, M. Dozono, F. Endo, M. Fukuda, N. Fukuda, C. Fukushima, M. Fukutome, T. Haginouchi, S. Hayakawa, Y. Hijikata, J.W. Hwang, E. Ideguchi, S. Ishio, N. Iwasa, K. Kameya, K. Kawata, R. Kojima, K. Kusaka, J. Li, Y. Nakamura, H. Nishibata, D. Nishimura, K. Okawa, S. Ota, D. Suzuki, H. Suzuki, T. Saito, Y. Shimizu, S. Shimoura, T. Sumikama, H. Takahashi, H. Takeda, H. Tanaka, M. Tanaka, T. Teranishi, T. Tomiyama, T. Uesaka, R. Urayama, K. Yako, Y. Yanagisawa, K. Yoshida, M. Yoshimoto</i>	
Isomeric gamma-ray measurement system at $S2+$ in SHARAQ13 experiment	13
<i>Y. Nakamura, M. Amitani, C. Fukushima, T. Tomiyama, S. Hanai, K. Kawata, S. Michimasa, D. Nishimura, K. Okawa, T.Y. Saito, R. Yokoyama, D.S. Ahn, H. Baba, T. Chillery, M. Dozono, F. Endo, M. Fukuda, N. Fukuda, M. Fukutome, T. Haginouchi, S. Hayakawa, Y. Hijikata, J. W. Hwang, E. Ideguchi, N. Imai, S. Ishio, N. Iwasa, K. Kameya, R. Kojima, K. Kusaka, J. Li, H. Nishibata, S. Ota, D. Suzuki, H. Suzuki, Y. Shimizu, S. Shimoura, T. Sumikama, H. Takahashi, H. Takeda, H. Tanaka, M. Tanaka, T. Teranishi, T. Uesaka, R. Urayama, K. Yako, Y. Yanagisawa, K. Yoshida, M. Yoshimoto</i>	
Measurement of double charge exchange ($^{12}\text{C}, ^{12}\text{Be}(0_2^+)$) reaction aiming for the observation of double Gamow–Teller giant resonance	15

A. Sakaue for the RIBF-141R1 collaboration

Measurement of fusion-evaporation cross sections in $^{136}\text{Xe}+^{64}\text{Zn}$ system using inverse kinematics	17
<i>J. T. Li, N. Imai, R. Yokoyama, T. Chillery, S. Michimasa, S. Hanai, T. Saito, R. Kojima, H. Yamaguchi, S. Shimoura, D. Nishimura, S. Sugawara, M. Dozono, K. Hagino, D. Suzuki, Y. Watanabe, Y. Aritomo, S. Sakaguchi, S. Ota, M. Shiraishi, E. Takada</i>	
In-beam γ -ray spectroscopy of ^{32}Mg	19
<i>N. Kitamura, K. Wimmer, T. Miyagi, A. Poves, N. Shimizu, J. A. Tostevin, V. M. Bader, C. Bancroft, D. Barofsky, T. Baugher, D. Bazin, J. S. Berryman, V. Bildstein, A. Gade, N. Imai, T. Kröll, C. Langer, J. Lloyd, E. Lunderberg, F. Nowacki, G. Perdikakis, F. Recchia, T. Redpath, S. Saenz, D. Smalley, S. R. Stroberg, Y. Utsuno, D. Weisshaar, A. Westerberg</i>	
Direct measurement of the $^{14}\text{O}(\alpha, p)^{17}\text{F}$ reaction with the TexaAT_v2 detector	21
<i>S. Ahn, C. Park, D. Kim, K.I. Hahn, M. Avila, S. Bae, M. Barbui, D.W. Bardayan, J. Bishop, S.M. Cha, K.Y. Chae, A. Chen, T. Chillery, S. Do, N.N. Duy, G.M. Gu, S. Hayakawa, B. Hong, N. Imai, N. Iwasa, A. Kim, C.H. Kim, M.J. Kim, S.H. Kim, Y. Kim, N. Kitamura, Y. Koshchiy, S. Kubono, M.L. Cognata, H. Lee, B. Moon, T. Nakamura, K. Okawa, C.E. Parker, A. Psaltis, G.V. Rogachev, M. Roosa, M. Sasano, M. Sferrazza, H. Yamaguchi Q. Zhang</i>	
Direct measurement of the $^{26}\text{Si}(\alpha, p)^{29}\text{P}$ reaction at CRIB for the nucleosynthesis in the X-ray bursts	24
<i>K. Okawa, M. J. Kim, K. Y. Chae, S. Hayakawa, S. Adachi, S. M. Cha, T. Chillery, N. N. Duy, T. Furuno, G. M. Gu, S. Hanai, N. Imai, D. Kahl, T. Kawabata, C. H. Kim, D. Kim, S. H. Kim, S. Kubono, M. S. Kwag, J. Li, N. R. Ma, S. Michimasa, K. Sakanashi, H. Shimizu, O. Sirbu, N. K. Uyen, H. Yamaguchi, R. Yokoyama, Q. Zhang</i>	
Investigation of the ^6He beam for the $^6\text{He}+p$ reaction at CRIB	26
<i>Q. Zhang, M. Sferrazza, H. Yamaguchi, S. Hayakawa, K. Okawa, S. Cherubini, M. La Cognata, G. Pizzone, T. Chillery, S. Hanai, N. Imai, S. Masuoka, K. Yako</i>	

1b. Experimental Nuclear Physics: PHENIX Experiment at BNL-RHIC and ALICE Experiment at CERN-LHC

Multiplicity dependence of direct photon production in pp collisions at $\sqrt{s} = 13$ TeV	29
<i>H. Murakami and T. Gunji</i>	
Measurement of long-range two-particle correlation and pseudorapidity dependence of v_2 with ALICE	31
<i>Y. Sekiguchi for the ALICE Collaboration</i>	
Production of direct photons via internal conversions in Pb–Pb collisions at $\sqrt{s_{\text{NN}}} = 5.02$ TeV with ALICE at the LHC	33
<i>D. Sekihata and T. Gunji</i>	
Space-charge distortion correction for the ALICE-TPC using machine learning methods	35
<i>H. Baba, D. Sekihata, T. Gunji</i>	

2. Accelerator and Instrumentation

Development and commissioning of a mosaic type array formed by Si photodiodes	37
<i>J. T. Li, N. Imai, R. Kojima, R. Yokoyama, T. Chillery, S. Michimasa, S. Hanai, T. Saito, M. Shiraishi</i>	
Recent activities with an active target CAT-M	39
<i>S. Ota M. Dozono, F. Endo, S. Hanai, S. Hayakawa, N. Imai, K. Kawata, R. Kojima, J. Li, S. Michimasa, A. Sakaue, R. Yokoyama, Y. Hijikata, T. Isobe, D. Suzuki, T. Uesaka, S. Fracassetti, M. Latif, R. Raabe, N. Zhang, T. Harada, J. Zenihiro, E. Takada,</i>	
New implantation detectors for decay spectroscopy at fragmentation facilities	41

R. Yokoyama, S. Nishimura, V.H. Phong, S. Kurosawa

Cathode-readout self-triggering system on a multi-wire drift chamber	42
<i>S. Hayakawa, K. Okawa, Q. Zhang, H. Yamaguchi, M. Sferrazza, S. Cherubini, T. Chillery S. Hanai N. Imai M. La Cognata, S. Masuoka R. G. Pizzone, K. Yako</i>	
Improved ${}^6\text{He}$ beam production at CRIB with MWDC and degraders	44
<i>H. Yamaguchi, M. Sferrazza, S. Hayakawa, K. Okawa, Q. Zhang, S. Cherubini, M. La Cognata, R.G. Pizzone, T. Chillery, S. Hanai, N. Imai, S. Masuoka, K. Yako</i>	
Development of a Radio Frequency Dipole Mass Filter for the Francium Permanent Electric Dipole Moment Search .	45
<i>M. Fukase, H. Nagahama, K. Nakamura, N. Ozawa, M. Sato, T. Nakashita, S. Nagase, D. Uehara, Y. Kotaka, K. Kamakura, T. Aoki, H. Haba, A. Takamine, H. Ueno, Y. Sakemi</i>	
Optical system for the optical lattice trapping of heavy alkali atoms	47
<i>N. Ozawa, K. Nakamura, S. Nagase, T. Nakashita, H. Nagahama, Y. Sakemi</i>	
Development of sustainable ${}^{24}\text{Mg}^{8+}$ beam production at HyperECR	49
<i>K. Kamakura, Y. Kotaka, T. Nakagawa, J. Ohnishi, K. Hatanaka, A. Goto, H. Yamaguchi, Y. Sakemi</i>	
Current status of the development of the emittance monitor for high-intensity ion beams accelerated by AVF Cyclotron	51
<i>Y. Kotaka, K. Kamakura, H. Yamaguchi, N. Imai, Y. Sakemi, J. Ohnishi, K. Hatanaka</i>	

3. Theoretical Nuclear Physics

Gamow-Teller transition described by the Monte-Carlo shell model	53
<i>K. Yanase, N. Shimizu, Y. Tsunoda, Y. Utsuno</i>	

4. Other Activities

The 21th CNS International Summer School CNSSS22	55
<i>N. Aoi, T. Gunji, N. Imai, H. Liang, S. Michimasa, H. Nagahama, T. Otsuka, H. Sakai, Y. Sakemi, H. Sakurai, N. Shimizu, S. Shimoura, H. Ueno, T. Uesaka, Y. Utsuno, T. Wakasa, K. Yako, H. Yamaguchi, K. Yoneda</i>	
Laboratory Exercise for Undergraduate Students	57
<i>H. Nagahama, S. Nagao, K. Yako, S. N. Nakamura, M. Fukase, K. Okawa, K. Kawata, R. Mizuno, K. Kokubun, S. Michimasa, N. Imai, Y. Yamaguchi, H. Sakemi, M. Niikura</i>	

Appendices

Symposium, Workshop, Seminar, and PAC	59
CNS Reports	60
Publication List	61
Talks and Presentations	67
Press Releases	72
Personnel	73

Experimental Nuclear Physics: Low and Intermediate Energies

Data Analysis of OEDO day-0 Experiment Measuring $^{93}\text{Zr} + d$ Transmutation Reactions for the Study of Deuteron Breakup

T. Chillery, J. W. Hwang^a, M. Dozono^b, N. Imai, S. Michimasa,

T. Sumikama^c, N. Chiga^c, S. Ota^d, S. Nakayama^e

for the ImPACT Collaboration

Center for Nuclear Study, Graduate School of Science, University of Tokyo

^a *Center for Exotic Nuclear Studies, Institute for Basic Science (IBS), Daejeon 34126, Rep. of Korea*

^b *Graduate School of Science, Kyoto University, Sakyo, Kyoto 606-8501, Japan*

^c *RIKEN Nishina Center for Accelerator-Based Science, Wako, Saitama 351-0198, Japan*

^d *Research Center for Nuclear Physics, Osaka University, Ibaraki, Osaka 567-0047, Japan*

^e *Nuclear Data Center, Japan Atomic Energy Agency, Ibaraki, Japan*

Radioactive high level waste (HLW) treatment remains a challenge in achieving long-term sustainability of nuclear power generation [1]. In particular, long-lived fission products (LLFPs) with half lives reaching millions of years continue to pose a problem to waste management. A promising alternative is using nuclear transmutation, whereby the LLFP is bombarded by energetic light particles to form stable and short-lived products for simpler management. Early transmutation studies [2] used neutron-capture processes on HLW, however LLFP ^{93}Zr with a half life 1.61 million years remains an exception. The neutron-capture cross sections are relatively small compared to other LLFPs, also the small isotopic abundance (about 14% [2]) of ^{93}Zr in waste means additional ^{93}Zr may be produced by neutron-capture on stable $^{90,91,92}\text{Zr}$ isotopes [3] thereby diminishing the technique's effectiveness. Recent experimental studies were performed for deuteron-induced reactions on ^{93}Zr , notably previous ImPACT studies across 50 – 210 MeV/nucleon [4–6], the results of which suggest a promising alternative in the transmutation of this LLFP. In particular, deuteron-induced reaction cross sections for LLFPs are enhanced by deuteron breakup mechanisms at energies above 50 MeV/nucleon [7, 8].

Theoretical models TALYS [9] and DEURACS [8] are under development to model reaction mechanisms in deuteron breakup. However, additional cross-section data is needed at energies below 50 MeV/nucleon to further investigate the enhancement of production cross sections from breakup channels, and benchmark current deuteron-breakup models at lower energies. In October 2017 the $^{93}\text{Zr} + d$ reaction was studied under inverse kinematics at 27.7 MeV/nucleon using the OEDO beamline and SHARAQ spectrometer, housed at RIBF, RIKEN in Japan. This report covers the analysis performed between April 2022 – March 2023 to obtain clear particle identification (PID) of the reaction products, necessary to extract production cross sections.

The ^{93}Zr secondary beam was produced in the BigRIPS separator from in-flight fission of 345 MeV/nucleon ^{238}U with a ^9Be 5 mm thick target. The beam energy was degraded to approximately 32 MeV/nucleon using a 3.5 mm thick Al wedge-shaped (3.68 mrad) degrader. The beam

was transported down to the OEDO beamline, where it bombarded a cryogenically-cooled deuterium gas target installed at focal plane S0. Downstream of the D_2 target, the SHARAQ spectrometer was operated in QQD mode to collect and momentum-analyze the reaction products. A diagram of the setup around S0 may be found in Fig. 4 of Ref. [10]. Parallel plate avalanche counters (PPACs) were installed at focal planes FE12 and S1 to measure position, timing, and magnetic rigidity ($B\rho$) of the beam and products. Near the back of S1, a 30 pad ionization chamber (IC) with 750 mm active depth (1000 mm total depth from S1) was filled with 130 Torr CF_4 gas to successfully stop the beam and products, thereby measuring their Bragg peaks. The SHARAQ D1 dipole was set to one of five settings $\Delta B\rho/B\rho_0 = -9.5\%$, -5.5% , -1.5% , $+2.5\%$, and $+6.0\%$ where 0% is the central beam trajectory ($B\rho_0 = 1.6210 \text{ Tm}$).

Beam entering the gas target was counted using the time-of-flight (TOF) measured by diamond and PPAC detectors installed in the BigRIPS separator and OEDO beamline. Reaction products were identified at S1 using their $B\rho$, flight-path-length (FPL), TOF, Bragg peak energy, and range information. The tracking information of FE12 and S1 PPACs was fitted to extract the $B\rho$ and FPL through SHARAQ. The TOF between S0 - S1 was calculated as the difference between S1 PPACs' anode timing and timing extrapolated to S0 using FE12 PPACs' tracking and anode timing. The mass-to-charge (A/Q) was calculated from $B\rho$ as:

$$\frac{A}{Q} = \frac{B\rho}{\gamma\beta} \frac{e}{c \cdot m_u},$$

where γ is the Lorentz factor, β is velocity (FPL/TOF) scaled to the speed of light c , and $\frac{e}{c \cdot m_u}$ is a constant ($0.3214 \text{ C}\cdot\text{s}\cdot\text{kg}^{-1}\cdot\text{m}^{-1}$). The Bragg peak structure was fit event-by-event using a spline normalized to SRIM-2013 stopping-power data to extract the peak and range information. Sample fits are shown in Fig. 1. The mass number (A) was extracted from the fitted range, assuming the energy per nucleon is the same as beam, and the ion's atomic number (Z) is proportional to peak energy. The Z -resolution was improved by correcting the fitted peak energy for high order dependencies on S1 x,y positions due to the IC response.

The atomic number vs IC depth of ions with $\beta = 0.212$

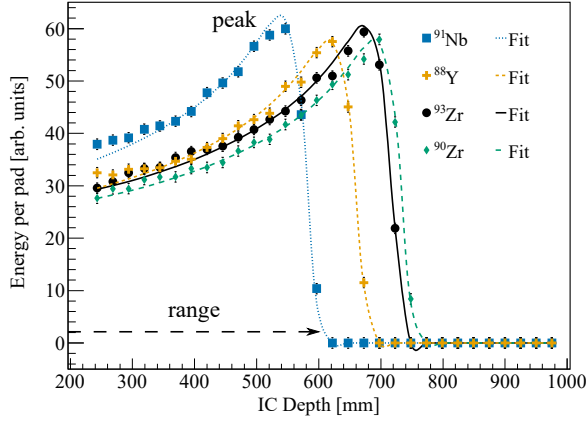


Figure 1: Sample Bragg peaks collected by the ionization chamber at S1 using the measured energy deposited in each pad (markers) with complementary spline fits (lines)

at setting $\Delta B\rho/B\rho_0 = -1.5\%$ is plotted in Fig. 2. Beam contamination present at approximate range 755 mm extends towards the $Z = 41$ region, and to resolve this the Z-identification used two-dimensional cuts on atomic number vs range, represented by the dashed lines, thus clearly separating each fragment; Nb, Zr, and Y.

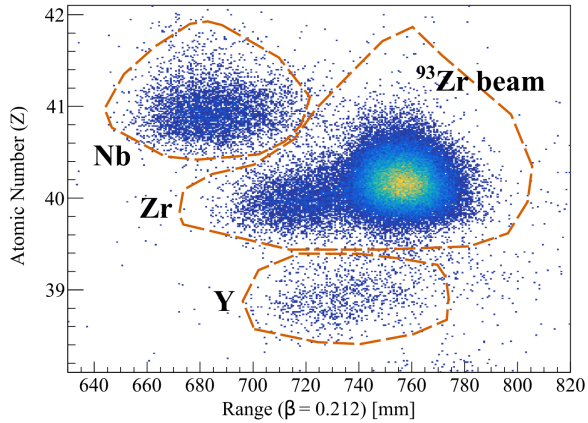


Figure 2: Atomic number (Z) vs range of ion (at $\beta = 0.212$) deposited in IC chamber at SHARAQ setting $\Delta B\rho/B\rho_0 = -1.5\%$. Dashed lines represent the two-dimensional cuts applied to select each Z.

Final PID was achieved using the mass number vs mass-to-charge gated on each Z locus. The PID at setting $\Delta B\rho/B\rho_0 = -1.5\%$ is shown in Fig. 3. Each isotope has multiple loci due to the wide charge-state distribution at this measurement's low energy: 23.2 MeV/nucleon at S1. In the near future the clear PID from this analysis will be used to count the number of each reaction product, allowing the extraction of production cross sections from the data. The final cross sections with discussion of their impact on nuclear transmutation and understanding deuteron breakup will be submitted for publication in the near future.

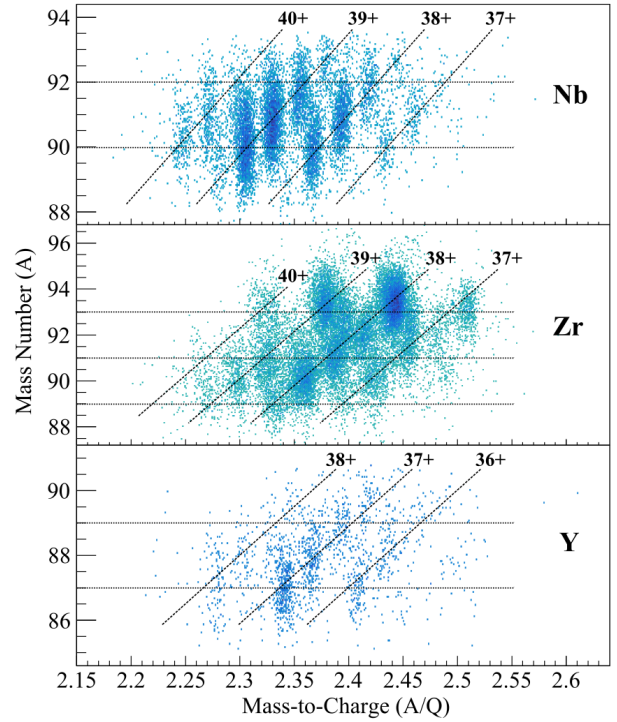


Figure 3: Mass number (A) vs mass-to-charge (A/Q) for SHARAQ setting $\Delta B\rho/B\rho_0 = -1.5\%$, gated on Z-loci in Fig. 2. Dashed lines are to guide the eye.

References

- [1] IAEA, Nuclear Energy Series. Status and Trends in Spent Fuel and Radioactive Waste Management, No. NW-T-1.14 (Rev. 1), 2022, Vienna, ISBN 978-92-0-130721-7
- [2] P. Wydler and L. H. Baetsle, In 6th information exchange meeting on actinide and fission product partitioning and transmutation, Technical report, OECD/NEA (2001).
- [3] A. Hermanne, J. Nucl. Sci. Technol. **39:sup2** 1202–1205 (2002).
- [4] S. Kawase *et al.* PTEP **2017** 093D03 (2017).
- [5] S. Kawase *et al.* In JAEA-Conf, **2018-001** 111 (2018).
- [6] K. Nakano *et al.* In EPJ Web of Conferences, **239** 20006 (2020).
- [7] H. Wang *et al.* Commun. Phys. **2** 78 (2019).
- [8] S. Nakayama *et al.* PRC **98** 044606 (2018).
- [9] A. Koning *et al.* User Manual of TALYS-1.96, <https://www-nds.iaea.org/talys/> (2021) Accessed 2nd Jun 2023.
- [10] S. Michimasa *et al.* NIM B **540** 194–198 (2023).

Surrogate reaction of $^{130}\text{Sn}(n, \gamma)$ at OEDO

N. Imai, S. Michimasa, T. Chillery, D. Suzuki^a, D.S. Ahn^b, A. Chae^c, S. Cherubini^d, M. La Cognata^e, M. Dozono^f, M. Egeta^g, F. Endo^g, N. Fukuda^a, T. Haginouchi^g, S. Hanai, S. Hayakawa, J.W. Hwang^b, Y. Hijikata^{a,f}, S. Ishio^g, N. Iwasa^g, K. Kawata, S. Kubono^a, R. Kojima, L. Lamia^d, J. Li, N. Nishimura^a, K. Okawa, H.J. Ong^h, S. Otaⁱ, S. Palmerini^j, R.G. Pizzone^d, T. Saito, Y. Shimizu^a, S. Shimoura^a, T. Sumikama^a, H. Suzuki^a, H. Takeda^a, A. Tumino^{d,k}, X. Tang^h, H. Tanaka^l, M. Tanaka^a, T. Teranishi^l, Y. Togano^a, R. Yokoyama, R. Yoshida^f, K. Yoshida^a, M. Yoshitomo^a, Y. Wang^m, Z. Xiao^m

Center for Nuclear Study, Graduate School of Science, University of Tokyo

^aRIKEN Nishina Center

^bCENS, Institute of Basic Science

^cDepartment of Physics, Sungkyunkwan University

^dDepartment of Physics, University of Catania

^eIstituto Nazionale di Fisica Nucleare (INFN) Laboratori Nazionali del Sud

^fDepartment of Physics, Kyoto Univ.

^gDepartment of Physics, Tohoku Univ.

^hInstitute of Modern Physics (IMP), Chinese Academy of Sciences

ⁱRCNP, Osaka Univ.

^jDepartment of Physics, University of Perugia

^kFaculty of Engineering and Architecture, Kore University of Enna

^lDepartment of Physics, Kyushu Univ.

^lDepartment of Physics, Tsinghua Univ.

The r -process nucleosynthesis is a major origin of heavy elements beyond iron. Because of high neutron densities in explosive astrophysical conditions, neutron-rich radioactive isotopes (RIs) are involved in the r -process. Though possible scenarios of the r -process were proposed more than fifty years ago, the astrophysical sites of the r -process are still one of the biggest problems in physics. Nucleosynthesis simulations require precise nuclear-physics inputs such as β decay rates, masses of the nuclei, and neutron capture rates, which can constrain the astrophysical conditions. However, as the neutron targets are not available yet, it is impossible to measure the capture cross sections and related rates directly. Most neutron-capture rates rely on statistical model calculations in particular to describe the compound processes. There are significant uncertainties on level densities and γ -ray emission probabilities from the highly excited states, causing theoretical cross sections to differ by several orders of magnitude between the models.

We evaluated the neutron capture reaction rate on ^{79}Se with the surrogate reaction of $^{79}\text{Se}(d, p)$ in inverse kinematics, where the γ emission probabilities in the unbound states of ^{80}Se were determined by measuring the residual nuclei without detecting the γ rays [1]. The present study aims to determine the neutron capture rate on ^{130}Sn via (d, p) reaction with a ^{130}Sn beam. The surrogate ratio technique was employed by also measuring the $^{130}\text{Te}(d, p)$ reaction. In addition, the systematic error was evaluated by measuring $^{124}\text{Sn}(d, p)$.

The experiment was conducted at the OEDO beamline at RIBF. The cocktail beam including ^{130}Sn was produced by the in-flight fission of ^{238}U at 345 MeV/nucleon. The TOF

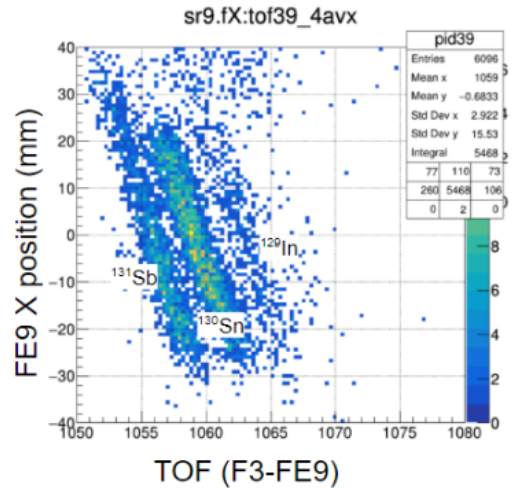


Figure 1: PID map of the secondary beams at FE9. See the text for details.

of the beam measured between F3 and FE9 indicates the energy of around 170 MeV/nucleon. RI beams were identified by the $B\rho$ -TOF method. Figure 1 shows the particle identification (PID) map of the secondary beam, demonstrating that ^{130}Sn beam is well separated from the other isotopes. Thanks to the new optics developed in the MS22-1 and described in the report by S. Michimasa *et al.*, in this volume, the transmission between F3 and FE9 was improved to be 85% for the beam with the F1 momentum slit of $\pm 0.5\%$. The energy of the cocktail beam was further degraded to around 20 MeV/nucleon by a combination of the

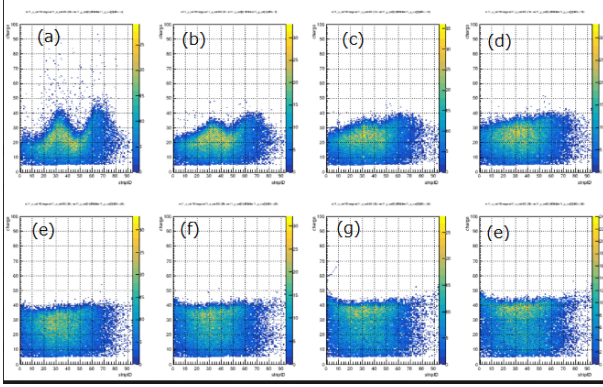


Figure 2: The correlation between the charge and the horizontal (x) position for each y position. Panels of (a)~(f) indicate the correlation for every 5 electrodes from the top.

angle-tunable degrader and a flat degrader. The energy of the beam was determined event-by-event by measuring the TOF between FE9 and FE12.

The ^{130}Sn beam of around 150 kcps was focused on the secondary target of $287 \mu\text{g}/\text{cm}^2$ -thick deuterated polyethylene. The recoil protons were detected by the TiNA2 array which was composed of four TTT double-sided square-shape Si detectors, six YY1 single-sided sector-shape Si detectors, and sixteen CsI(Tl) detectors. TTTs were placed in a cubic-configuration and YY1 were in a lampshade-like configuration. The four CsI(Tl) were placed behind each TTT to measure the ΔE - E correlation of the charged particles. The outgoing residual nuclei were momentum-analyzed by the D1 magnet of the SHARAQ spectrometer. Two SR-PPACs [2] and an ionization chamber were installed at the final focal plane to identify the residual nuclei.

The analysis of TTT, YY1 and CsI(Tl) detectors has been developed to select the protons and to reconstruct the missing mass spectrum. Also, the data from the beam-line detectors have been analyzed. It turned out that the x position of the SR-PPAC largely depends on the y position as presented in Figs 2. The x position was compensated by selecting every 5 electrodes in y. After correcting the x position at S1, the ions were identified. The PID plot was shown in Fig. 3. The Bragg curve is being analyzed.

References

- [1] N. Imai *et al.*, submitted to Phys. Lett. **B**.
- [2] S. Hanai *et al.*, NIMB 541, 194 (2023).

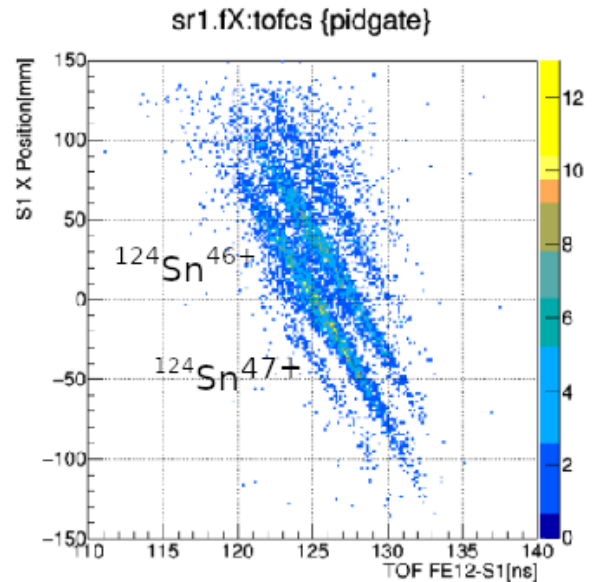


Figure 3: S1 PID plot for ^{124}Sn beam. Five loci can be seen. The lowest locus is the Li-like ion, i.e. three electrons are attached to the ^{124}Sn beam.

Report on OEDO-SHARAQ experiments in FY 2022

S. Michimasa, T. Chillery, N. Imai, R. Yokoyama, N. Kitamura, S. Hanai, R. Kojima, J. W. Hwang^a, T. Sumikama^b, M. Dozono^c, S. Ota^d, D. S. Ahn^a, Y. Hijikata^c, K. Kawata^d, K. Kusaka^b, J. Li, M. Ohtake^b, D. Suzuki^b, H. Suzuki^b, H. Takeda^b, K. Yako, Y. Yanagisawa^b, K. Yoshida^b, M. Yoshimoto^b, and S. Shimoura^b

Center for Nuclear Study, Graduate School of Science, the University of Tokyo

^a *Center for Exotic Nuclear Studies, Institute of Based Science, Korea*

^b *RIKEN Nishina Center for Accelerator-Based Science*

^c *Department of Physics, Kyoto University*

^d *RCNP, Osaka University*

Operation of the OEDO-SHARAQ system commenced with the SHARAQ spectrometer [1] and a dispersion-matched beamline, called High-Resolution Beamline (HRB) [2] in 2009. Before the installation of the OEDO device, we had two types of ion optics modes for high-resolution spectroscopic experiments, which were named by High-Resolution Achromatic (HRA) transport and Dispersion Matching (DM) transport, respectively. In 2014, the development of the OEDO system was launched for nuclear experiments with radioactive isotopes (RIs) in the energy region of 10–50 MeV/u, and was completed in March 2017 as part of the upgrade of the HRB [3]. A schematic layout of the BigRIPS, OEDO, and SHARAQ spectrometer is illustrated in Fig. 1. We performed the reaction cross-section

aiming at understanding neutron capture processes under the conditions of explosive phenomena in compact astronomical objects and in the Big Bang. However, the installation of the OEDO system arose from a situation in that high-resolution spectroscopy cannot be performed without magnet rearrangements.

In 2021, we performed a minor update of the OEDO-SHARAQ system as shown in the inset of Fig. 1 to obtain better transmission of slowed-down RI beams as well as a recovery of scientific opportunities of high-resolution spectroscopy in the same magnet arrangement. The inset in Fig. 1 illustrates how the OEDO beamline was rearranged in June, 2021. Finally, the OEDO-SHARAQ system successfully attained quite unique dual performances and multifaceted operations of them, enabling researches on these essential topics in nuclear physics. In this report, we present the record in FY2022, showcasing high and stable performances in each operation mode, as well as the ability to swiftly switch the modes.

The OEDO-SHARAQ has provided a total of four experimental opportunities in this fiscal year, covering both low-energy reaction studies and high-resolution spectroscopic studies. Table 1 summarizes the experiments performed and their conditions. The record comprises three LE-A S1 setup and one HE-DM S2 setup. The LE-A S1 setup indicates the setting for inverse-kinematics reaction measurements by low-energy achromatic RI beams at S0 where the reaction products are analyzed by S1 setup of SHARAQ spectrometer, while the HE-DM S2 setup is the setting for normal-kinematics high-energy high-resolution spectroscopy where the dispersion matching in BigRIPS-OEDO-SHARAQ are satisfied and S2 detector setup was used. The details of the experimental conditions and these setups will be elaborated on in each article within this annual report. Additionally it is noteworthy that the experimental setting was swiftly changed from the LE-A S1 mode to HE-DM S2 mode within four days .

All the experiments conducted in the LE-A S1 mode were inverse-kinematics (d,p) reaction measurements at around 20 MeV/u by using the TiNA particle-detector array for transfer reaction [4, 5] at S0. The ion optical design for the new magnet arrangement was detailed in Ref. [6]. We emphasize that this arrangement brought a significant improvement in the transmission of RI beams from F3 to the

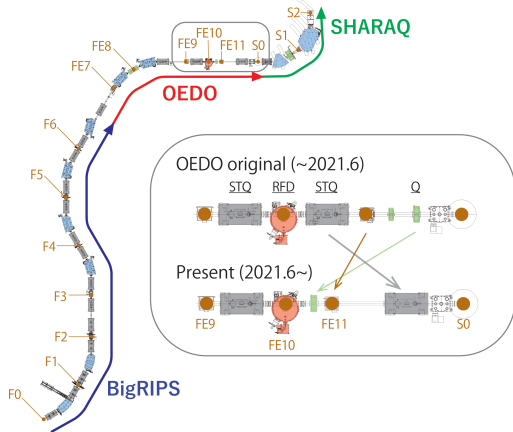


Figure 1: Schematic layout of BigRIPS separator, OEDO beamline, and SHARAQ spectrometer. The closed circles on the beamlines indicate the names of the focal planes. The inset shows how the OEDO beamline was rearranged in June, 2021.

measurements of long-lived fission products (LLFPs) with proton and deuteron nuclei at approximately 25 MeV/u. The data obtained are very fundamental and crucial for safe disposal of nuclear fuel waste. The OEDO-SHARAQ is also used to facilitate spectroscopic investigations of the nuclear structure in particular nuclei far from the β stability line by using single-nucleon transfer reactions. Moreover, we are developing similar reaction measurements to pursue astrophysical studies by using surrogate reactions and are

Table 1: Experiments using OEDO-SHARAQ in FY2022

Exp. ID	Date	RI beam	Mode
SHARAQ18	10-16 April	^{130}Sn	LE-A S1 Setup
SHARAQ19	16-21 May	^{56}Ni	LE-A S1 Setup
SHARAQ13	26 May - 3 June	^{46}Fe	HE-DM S2 Setup
SHARAQ12	5-11 Dec.	^{50}Ca	LE-A S1 Setup

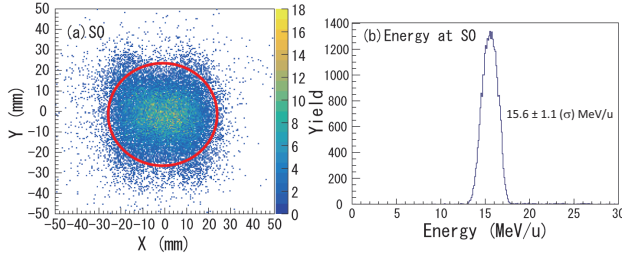


Figure 2: The characteristics of ^{56}Ni beam in the FY2022 series of OEDO-SHARAQ experiments. (a) Beam spot profile at the S0 secondary target. (b) Energy distributions of the RI beam at the S0 secondary target.

secondary target at S0. Table 2 summarizes the measured transmission of the RI beams before and after the rearrangement. The first two experiments were done in FY2022, and

Table 2: Transmissions of RI beams in OEDO S1 mode.

Beam	Energy (MeV/u)	Transmission in F3-S0	Magnet arrangement
^{130}Sn	22.9	~ 85%	Present
^{56}Ni	19.5	~ 85%	Present
^{79}Se	35.0	~ 18%	Original [3]

the last experiment was performed using the original magnet arrangement back in FY2017. The introduction of the new ion optics resulted in a significantly improvement in the beam transmission, approximately by a factor of 4.7. These measurements were successfully completed and the obtained data analyses are in progress.

During autumn, another experiment involving inverse-kinematics measurement of $^{50}\text{Ca}(d,p)$ reaction was performed. However, this experiment had to be suspended due to an accelerator malfunction, leaving some part of the accommodation incomplete. We plan to resume the physics measurement as soon as possible and obtain the complete set of experimental data.

The beam conditions at S0 measured in the ^{56}Ni experiment is shown in Fig. 2. Figure 2(a) shows the beam profile at S0, where a solid red circle indicates 50 mm^ϕ , which is the size of the secondary target. The beam was focused well on the target because the ion optics were tuned as designed. The energy distribution of $15.6 \pm 1.1\text{ MeV/u}$ was achieved, as shown in Fig. 2(b). The compression of the energy spread has significantly improved from the previous performance in 2017.

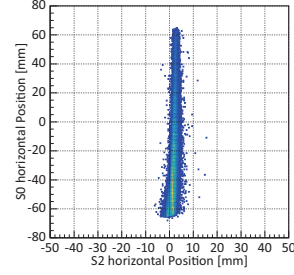


Figure 3: Correlation between S0 horizontal position and S2 horizontal position of ^{39}Ca beam in SHARAQ13 experiment.

A high-resolution performance of OEDO-SHARAQ was essential for an experiment aiming to measure the atomic masses of proton drip-line nuclei around Fe isotopes. The experiment is positioned as the next program of TOF-B ρ mass measurement around ^{54}Ca region [7, 8] and the recovered performance of DM ion optics [9] was maximally utilized. Figure 3 shows the correlation between hit positions of a momentum-dispersive S0 focus and the final focus S2. These hit positions had no correlation and therefore the lateral dispersion matching condition of OEDO-SHARAQ was fully obtained for the experiment. This measurement was successfully conducted, and the obtained data analysis is currently in progress.

This report described the OEDO-SHARAQ possessed dual performances in high-energy high-resolution spectroscopy and low-energy nuclear reaction measurements induced by RI beams. This duality resulted from the update of the beamline of the system in 2021. OEDO-SHARAQ intensively promotes programs that use both modes of operation and at the same time encourages innovative ideas for future experiments.

References

- [1] T. Uesaka *et al.*, Prog. Theor. Exp. Phys. **2012**, 03C007 (2012).
- [2] T. Kawabata *et al.*, Nucl. Instrum. Meth. Phys. Res., Sect. B **266**, 4201 (2008).
- [3] S. Michimasa *et al.*, Prog. Theor. Exp. Phys. **2019**, 043D01 (2019).
- [4] P. Schrock, *et al.*, RIKEN Accel. Prog. Rep. 51 (2018) 20.
- [5] B. Mauss, *et al.*, RIKEN Accel. Prog. Rep. 55 (2022) 93.
- [6] T. Chillery *et al.*, elsewhere in the CNS annual report 2022, (2023).
- [7] S. Michimasa *et al.*, Phys. Rev. Lett. **121**, 022506 (2018).
- [8] S. Michimasa *et al.*, Phys. Rev. Lett. **125**, 122501 (2020).
- [9] S. Michimasa *et al.*, CNS annual report 2021, CNS-REP-101, 31 (2022).

Study of νp -process nucleosynthesis at OEDO

D. Suzuki^a, B. Mauss^b, N. Imai, S. Michimasa, D. Beaumel^{c,a}, K.Y. Chae^d, S. Cherubini^e, T. Chillery, M. Dozono^{f,a}, M. Egeta^{g,a}, F. Endo^{g,a}, N. Fukuda^a, T. Haginouchi^{g,a}, S. Hanai, S. Hayakawa, Y. Hijikata^{f,a}, J.W. Hwang^h, S. Ishio^{g,a}, N. Iwasa^{g,a}, S. Kawase^{i,a}, K. Kawata, R. Kojima, S. Kubono^a, M. La Cognata^e, J. Li, N. Nishimura^a, K. Okawa, M. Oishi^{i,a}, H.J. Ong^{j,k,a}, S. Ota^k, S. Palmerini^{l,m}, R. Pizzone^e, T. Saito, H. Sakurai^a, S. Shimoura^a, Y. Shimizu^a, T. Sumikama^a, H. Suzuki^a, H. Takeda^a, H. Tanaka^{n,a}, M. Tanaka^a, X. Tang^j, T. Teranishi^{n,a}, Y. Togano^a, A. Tunimo^e, Y. Wang^o, K. Yako, K. Yahiro^{f,a}, H. Yamaguchi, R. Yokoyama, K. Yoshida^a, R. Yoshida^{f,a}, and M. Yoshimoto^a

Center for Nuclear Study, Graduate School of Science, University of Tokyo

^a *RIKEN Nishina Center*

^b *CEA-DAM*

^c *IJClab, IN2P3, CNRS*

^d *Department of Physics, Sungkyunkwan University*

^e *Istituto Nazionale di Fisica Nucleare (INFN) Laboratori Nazionali del Sud*

^f *Department of Physics, Kyoto University*

^g *Department of Physics, Tohoku University*

^h *Center for Exotic Nuclear Studies (CENS), Institute for Basic Science*

ⁱ *Interdisciplinary Graduate School of Engineering Sciences (IGES), Kyushu University*

^j *Institute of Modern Physics (IMP), Chinese Academy of Sciences*

^k *Research Center for Nuclear Physics (RCNP), Osaka University*

^l *Istituto Nazionale di Fisica Nucleare (INFN) Sezione di Perugia*

^m *Department of Physics, University of Perugia*

ⁿ *Department of Physics, Kyushu University*

^o *Tsinghua University*

Neutron-deficient stable isotopes, referred to as p -nuclei, are known to be produced by p process nucleosynthesis. However, certain lighter p -nuclei, e.g. Mo and Ru, are significantly underproduced in the present astrophysical scenario. The νp process [1] ascribes their origin to core-collapse supernovae, wherein the availability of neutrons aids the flow to bypass the waiting point ^{56}Ni on the synthesis path. The neutron capture cross section of ^{56}Ni , however, remains experimentally unknown because both the neutron and ^{56}Ni are short-lived. To evaluate the cross sections, we applied the surrogate method [2] to the (d,p) reaction by using an energy-degraded ^{56}Ni beam at OEDO.

The experiment was performed at the OEDO beam line of RIBF. The secondary beam was produced by the projectile fragmentation reaction of a ^{78}Kr beam at 345 MeV/nucleon and purified by the BigRIPS fragment separator. The total beam intensity at F3 was measured to be about 500 kpps (particles per second) with a purity of about 30% for ^{56}Ni . The impurities included ^{55}Co (50%) and ^{54}Fe (10%), both isotones of ^{56}Ni with $N = 28$. The energy of ^{56}Ni transmitted from BigRIPS to OEDO was about 113 MeV/nucleon. The beam energy was degraded at FE9 by an angle-tunable wedge-shaped degrader (3 mm in central thickness) together with a flat degrader (0.3 mm in thickness) [3], both made of aluminum. The angle of the former was set to 4 mrad to obtain a desired beam energy. The beam energy of ^{56}Ni was estimated to be 15.1(10) MeV/nucleon based

on the time of flight measurement from FE9 to FE12. The RF deflector at FE10 was operated at 100 kV to reduce the spot size of ^{56}Ni . The phase shift of RF was optimized to increase the transmission through the target frame aperture of 50 mm in diameter (Fig. 1). The transmission from F3 to FE12 was about 75% with a total rate of 370 kpps at FE12. CD_2 targets of 285 and 644 $\mu\text{g}/\text{cm}^2$, provided by INFN, were set at S0 about 1 m downstream of FE12. The incident position and angle of the secondary beam were deduced by a pair of SR-PPACs [4] in the vacuum chamber of FE12. The recoiling protons were detected by the silicon and CsI detectors array TiNA [5]. Missing mass spectra are deduced from the scattering angle and total kinetic energy measured by TiNA. The scattered particles were transmitted to a QQD spectrometer at zero degrees for the particle identification, which facilitated the determination of the decay channels. The spectrometer was equipped with a pair of SR-PPACs followed by an ionization chamber (IC) with CF_4 gas at 100 Torr. The transmission through the spectrometer was roughly 50%.

The analysis work has mainly been focused on the SR-PPACs and the IC so far. The charge calibration of the SR-PPAC was made by using the secondary beam data of ^{56}Ni obtained with the prescaled beam trigger during the physics run. Note that no pulser calibrations data are available with the present detectors. In the analysis, the uncalibrated charge distributions were first made as a function of

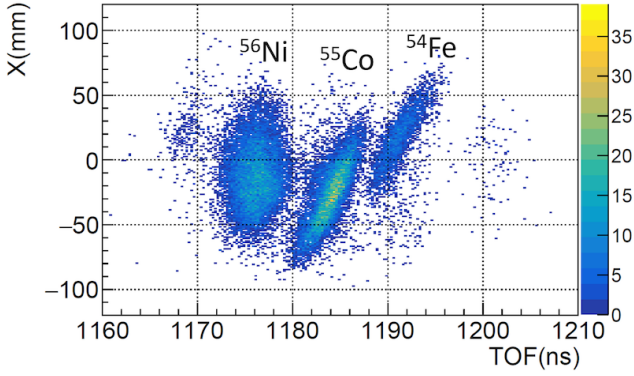


Figure 1: Horizontal position at S0 vs. TOF from F3 to FE9 of the secondary beam with the optimal RF settings.

readout strips. Here we only took the three largest charges into account and eliminated the smaller charges so that the resulting charge spectra show a distinct peak in each strip. The gain parameters were determined to adjust the peak heights to be almost constant among the strips belonging to a given readout plane.

During this calibration step, we found that the gains are not uniform especially in the vertical direction, which results in significant charge fluctuations. The cause of this issue is likely inherent in the detector construction itself, where the foils of the electrodes may not be secured sufficiently flat. To correct for the non-uniformity, the horizontal strips were subdivided into segments by every five vertical strips and the gain parameters were obtained for each segment. An example of the charge distribution after making all the corrections is shown in Fig. 2.

With the gain parameters thus obtained, the position was deduced by the so-called Q_0 - Q_1 method based on the ratio ($R(Q_1/Q_0)$) of the first (Q_0) and the second (Q_1) largest charges found in adjacent pairs of strips. The $R(Q_1/Q_0)$ ratio is translated to the position by using a table of conversion coefficients defined for all combinations of adjacent strip pairs. These coefficients were fine-tuned for each strip pair by using the beam data to make the resulting position distribution as smooth and seamless as possible inside and at the extreme ends of a strip. Otherwise, the spectra show a roughness with spike structures. The two-dimensional position distribution in Fig. 3 is thus obtained for ^{56}Ni beam particle events recorded by the prescaled beam trigger. The widths of the position distributions in the horizontal and vertical directions are evaluated to be 11 mm and 14 mm r.m.s., respectively, by Gaussian fittings.

The analysis of the IC is presently underway. The charge calibration was made by using pulser data acquired prior to the beamtime. The gain parameters were obtained by fitting a set of peaks in ADC spectra obtained for the respective strips. The pedestal data were not included in the fittings since the non-linearity turned out to be not negligible below about 500 ADC channels. The conversion coefficients to translate the calibrated ADC channels to the absolute energies were obtained by using the data of the ^{56}Ni beam with the high energy setting (about 110 MeV/nucleon). The av-

erage energy loss is estimated to be about 3.7 MeV/strip. Once the charge calibration is complete, we will start working on the analysis of the Bragg curves.

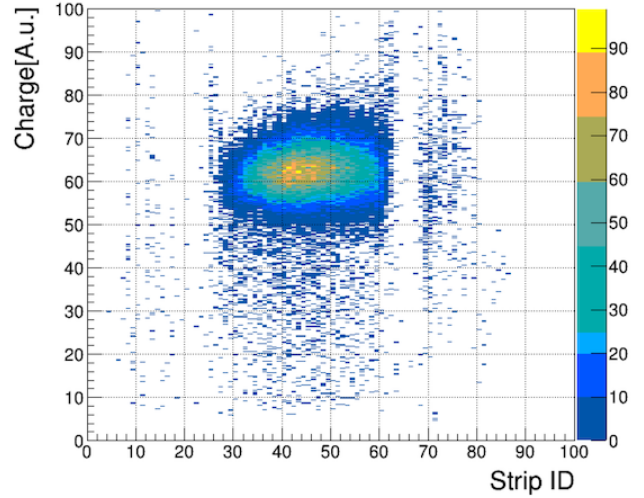


Figure 2: Charge distribution of the ^{56}Ni beam in the horizontal readout plane of the upstream SR-PPAC at FE9.

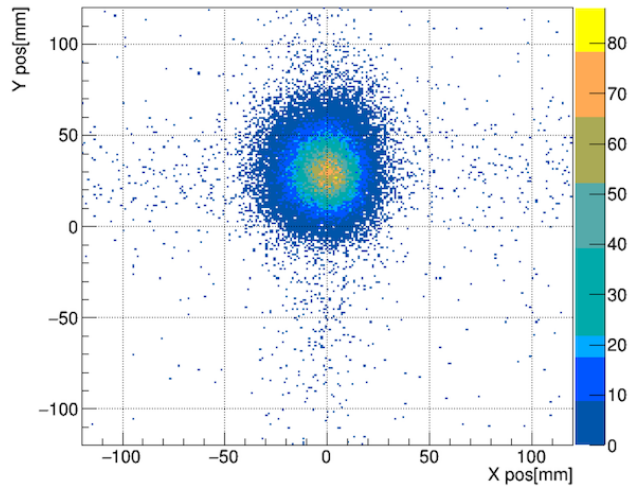


Figure 3: Position distribution of the ^{56}Ni beam at the target obtained from the analysis of the SR-PPACs.

References

- [1] C. Fröhlich *et al.*, Phys. Rev. Lett. **96** (2006) 142502.
- [2] N. Imai *et al.*, submitted to Phys. Lett. B.
- [3] J.W. Hwang *et al.*, RIKEN Accel. Prog. Rep. **53** (2020) 16.
- [4] S. Hanai *et al.*, Nucl. Instr. and Meth. B **541** (2023) 194.
- [5] B. Mauss *et al.*, RIKEN Accel. Prog. Rep. **54** (2021) 114.

Half-life measurement of 107-keV isomeric state in ^{45}Cr

M. Amitani^{a,b}, Y. Nakamura^{a,b}, C. Fukushima^{a,b}, T. Tomiyama^{a,b}, S. Hanai^c, K. Kawata^c, S. Michimasa^c, D. Nishimura^{a,b,c}, K. Okawa^c, T.Y. Saito^c, R. Yokoyama^c, D.S. Ahn^d, H. Baba^b, T. Chillery^c, M. Dozono^{b,e}, F. Endo^{b,f}, M. Fukuda^{b,g}, N. Fukuda^b, M. Fukutome^{b,g}, T. Haginouchi^{b,f}, S. Hayakawa^c, Y. Hijikata^{b,e}, J. W. Hwang^b, E. Ideguchi^{b,h}, N. Imai^c, S. Ishio^{b,f}, N. Iwasa^{b,f}, K. Kameya^{b,f}, R. Kojima^c, K. Kusaka^b, J. Li^c, H. Nishibataⁱ, S. Ota^h, D. Suzuki^b, H. Suzuki^b, Y. Shimizu^b, S. Shimoura^{b,c,h}, T. Sumikama^b, H. Takahashi^{a,b}, H. Takeda^b, H. Tanaka^{b,i}, M. Tanaka^{b,j}, T. Teranishi^{b,i}, T. Uesaka^b, R. Urayama^{b,f}, K. Yako^c, Y. Yanagisawa^b, K. Yoshida^b, and M. Yoshimoto^b

^aDepartment of Natural Sciences, Tokyo City University

^bRIKEN Nishina Center

^cCenter for Nuclear Study, Graduate School of Science, the University of Tokyo

^dCenter for Exotic Nuclear Studies, Institute for Basic Science

^eDepartment of Physics, Kyoto University

^fDepartment of Physics, Tohoku University

^gDepartment of Physics, Osaka University

^hResearch Center for Nuclear Physics, Osaka University

ⁱDepartment of Physics, Kyushu University

^jFaculty of Arts and Science, Kyushu University

The atomic nuclei near the self-conjugate line at $Z = 21$ are known to systematically have spin-gap isomers formed by low-lying $d_{3/2}$ and $f_{7/2}$ orbitals. In $^{42-47}\text{Sc}$ ($Z = 21$) isotopes, isomers with the $d_{3/2}$ -hole configuration have already been reported, while some of isomers with the mirror configuration at $N = 21$ remain unreported.

In this report, we present a preliminary result regarding the half-life of the isomeric state in ^{45}Cr ($Z = 24$, $N = 21$), which was determined for the first time. The isomeric state was discovered to be located at an excitation energy of 107 keV in the previous study [1]. This state was tentatively assigned as the mirror state in ^{45}Sc at 12.4 keV with a spin-parity of $3/2^+$ and a half-life of 318 ms. However, the half-life of the isomeric state in ^{45}Cr had not been determined yet. Only the lower limit of the lifetime of the 107-keV state was reported ($>80 \mu\text{s}$) and it was estimated to be on the order of more than $100 \mu\text{s}$. Recently, the γ -ray spectroscopy for mirror nuclei with isospin $T = 3/2$, and with $A = 45$ and 47 was performed via one- and two-nucleon knockout reactions [2]. However, the 107-keV γ rays were not observed directly due to the long lifetime of the isomeric state. The present study on ^{45}Cr was performed by combining with the TOF- $B\rho$ mass measurements in the vicinity of ^{47}Fe (SHARAQ13) in May-June 2022, which will be explained by Ref. [3].

The experimental setup was similar to the previous experiment [4, 5]. We carried out the delayed γ -ray spectroscopy [6] of unstable nuclei including ^{45}Cr . A secondary beam consisting of various proton-rich isotopes in the pf -shell region was produced by fragmentation of a ^{78}Kr primary beam accelerated at 345 MeV/nucleon impinging on a ^9Be target with a thickness of 2.2 g/cm². After the TOF measurements of the secondary beam particles, these isotopes were implanted into an active stopper consisting of

two plastic scintillators located downstream of the final focal plane (S2) of OEDO-SHARAQ. For the delayed γ -ray spectroscopy, two HPGe detectors were placed in the proximity of the active stopper, perpendicular to the beamline. The γ -ray energy and hit timing of two HPGe detectors were recorded by a self-triggering DAQ system equipped with digital signal processor which shared timestamp information with the DAQ for mass measurements. This system enables us to match the heavy-ion events and γ -ray events without limitation of the time window.

Figure 1 shows the particle identification plot around ^{45}Cr

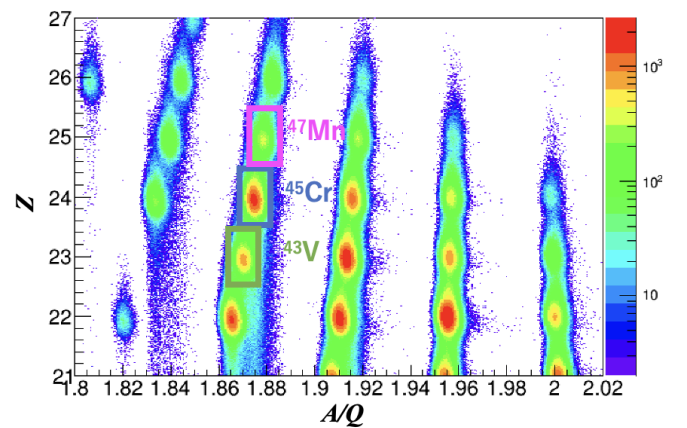


Figure 1: Particle identification plot in the SHARAQ13 experiment. The x axis represents the charge-to-mass ratio (A/Q), while the y axis corresponds to the atomic number (Z). The boxes surrounding the isotopes of ^{43}V , ^{45}Cr and ^{47}Mn are used as the gate of the isotope selection for the γ rays.

obtained in this experiment. The particle identification was

clear for incident RI beams. The ^{45}Cr nuclei implanted in the active stopper amounted to approximately 5×10^5 particles in the 25 hours currently analyzed, which is part of the beam time of about 100 hours. The energy spectra of γ rays followed by the implantation of ^{43}V , ^{45}Cr and ^{47}Mn are shown as Fig. 2, where the time window after the implantation of the RI beams was opened from $1 \mu\text{s}$ to 2 ms. A 107-keV γ -ray peak has been clearly observed in only ^{45}Cr , which is consistent with the previous report [1]. The time

uncertainties are ongoing. After establishing the half-life value, the reduced transition strength $B(M2)$ for the 107-keV transition from the first excited state with $J^\pi = 3/2^+$ to the ground state with $J^\pi = 7/2^-$ can be deduced. We plan to discuss the features of the isospin symmetry in pf shell nuclei including ^{45}Sc - ^{45}Cr pair in comparison with theoretical calculations.

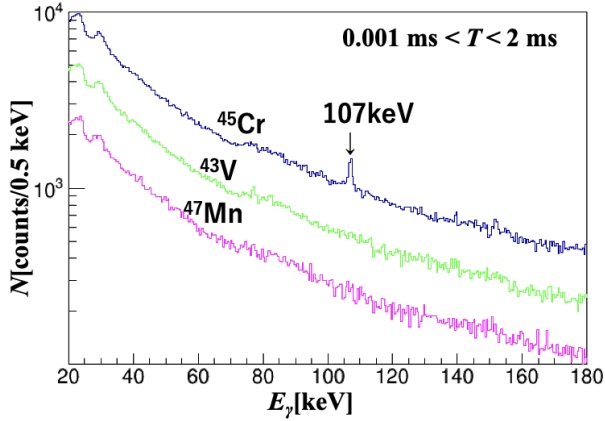


Figure 2: Comparison of gamma-ray energy spectra of three nuclides in the proximity of ^{45}Cr .

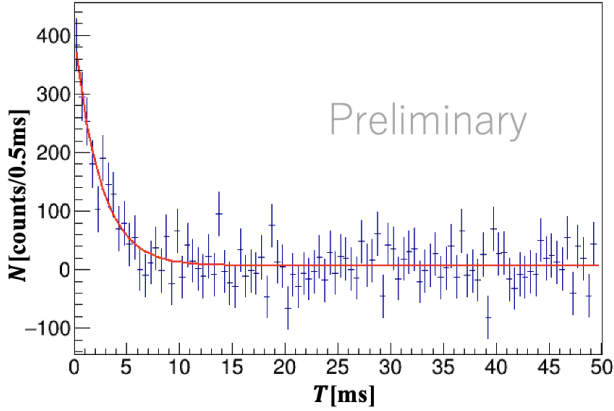


Figure 3: Decay curve in the time spectrum of the 107-keV γ rays from ^{45}Cr . The backgrounds have been already subtracted by using the neighboring region of the 107-keV peak in the energy spectrum.

spectrum of the 107-keV γ rays in ^{45}Cr is shown in Fig. 3. The backgrounds have been already subtracted by using the neighboring region of the 107-keV peak in the energy spectrum. The fitting function was used exponential function for measuring the half-life of ^{45}Cr . The time spectrum was fit to an exponential function plus a constant background as $f(t) = N_0 \exp(-\ln 2 \times t/T_{1/2}) + C$, where three free parameters of N_0 , $T_{1/2}$, and C are used. In the current analysis, we revealed that the half-life of the isomeric state in ^{45}Cr was preliminary determined to be 2 ms. Detailed analysis to determine the precision of the half-life including systematic

References

- [1] R. Hoischen *et al.*, J. Phys. G: Nucl. Part. Phys. **38**, (2011) 035104.
- [2] S. Uthayakumaar *et al.*, Phys. Rev. C **106** (2022) 024327.
- [3] S. Hanai *et al.*, in this report.
- [4] S. Michimasa *et al.*, Phys. Rev. Lett. **121**, (2018) 022506.
- [5] S. Michimasa *et al.*, Phys. Rev. Lett. **125**, (2020) 122501.
- [6] Y. Nakamura *et al.*, in this report.

Direct mass measurement of proton-rich Fe isotopes

S. Hanai^a, S. Michimasa^a, N. Imai^a, R. Yokoyama^a, D.S. Ahn^b, M. Amitani^{c,d}, H. Baba^d, T. Chillery^a, M. Dozono^{e,d}, F. Endo^{f,d}, M. Fukuda^{g,d}, N. Fukuda^d, C. Fukushima^{c,d}, M. Fukutome^{g,d}, T. Haginouchi^{f,d}, S. Hayakawa^a, Y. Hijikata^{e,d}, J.W. Hwang^b, E. Ideguchi^{h,d}, S. Ishio^{f,d}, N. Iwasa^{f,d}, K. Kameya^{f,d}, K. Kawata^a, R. Kojima^a, K. Kusaka^d, J. Li^a, Y. Nakamura^{c,d}, H. Nishibata^{i,d}, D. Nishimura^{c,a,d}, K. Okawa^a, S. Ota^{h,a}, D. Suzuki^c, H. Suzuki^c, T. Saito^a, Y. Shimizu^d, S. Shimoura^{a,d,h}, T. Sumikama^d, H. Takahashi^{c,d}, H. Takeda^d, H. Tanaka^{i,d}, M. Tanaka^d, T. Teranishi^{i,d}, T. Tomiyama^{c,d}, T. Uesaka^d, R. Urayama^{f,d}, K. Yako^a, Y. Yanagisawa^d, K. Yoshida^d, and M. Yoshimoto^d

^a Center for Nuclear Study, Graduate School of Science, The University of Tokyo

^b Center for Exotic Nuclear Studies, Institute for Basic Science

^c Department of Natural Sciences, Tokyo City University

^d RIKEN Nishina Center

^e Department of Physics, Kyoto University

^f Department of Physics, Tohoku University

^g Department of Physics, Osaka University

^h Research Center for Nuclear Physics, Osaka University

ⁱ Department of Physics, Kyushu University

The two-proton radioactivity ($2p$ decay), where two protons are simultaneously emitted during nuclear decay, was theoretically predicted over 60 years ago [1]. In the early 2000s, $2p$ decay was discovered in very proton-rich nuclei such as ^{45}Fe and ^{48}Ni [2, 3]. The energy level structure and one- and two-proton separation energies (S_p , S_{2p}) are essential for evaluating the two-proton emission probability of the $2p$ emitter tunneling through the Coulomb and centrifugal potentials. Since the level structure and mass difference among one- and two-proton-deficient nuclei are directly related to S_p and S_{2p} , the systematic measurement of the masses of nuclei around the $2p$ emitter leads to a complete understanding of $2p$ decay.

We performed direct mass measurements of proton-rich Fe isotopes including ^{45}Fe using the TOF- $B\rho$ technique [4] at the OEDO-SHARAQ beamline in RI beam factory, RIKEN. Figure 1 shows the configuration of the beamline for the experiment. Proton-rich isotopes were produced by the fragmentation of the ^{78}Kr primary beam at 345 MeV/nucleon in a ^9Be target with a thickness of 2.2 g/cm². The fragments were separated by the BigRIPS and transported to the OEDO beam line followed by the SHARAQ spectrometer. OEDO and SHARAQ were operated as a single spectrometer in the dispersion matching mode [5], which achieved a momentum resolution of 1/15,000. In the TOF- $B\rho$ method, the mass value is determined by the charge q , the time of flight (TOF) t , magnetic rigidity $B\rho$, and flight path length L using the following equation:

$$\frac{m}{q} = \frac{B\rho}{c} \sqrt{\left(\frac{ct}{L}\right)^2 - 1} \quad (1)$$

where c is the speed of light. TOF was measured by diamond detectors installed at the focal planes F3 and S2. Two

multiwire drift chamber (MWDC) tracking detectors were also installed at both F3 and S2 to calibrate the flight-path length. To measure the $B\rho$ value, a strip-readout parallel-plate avalanche counter (SR-PPAC), newly developed for measuring high-rate heavy-ion beams [6], was used at the intermediate focal plane S0. A silicon strip detector (SSD) was mounted at S2 to identify the atomic numbers of beam ions. Two layers of plastic scintillators surrounded by gamma-ray detectors were installed after S2. This system was used not only to stop the beam and measure the parti-

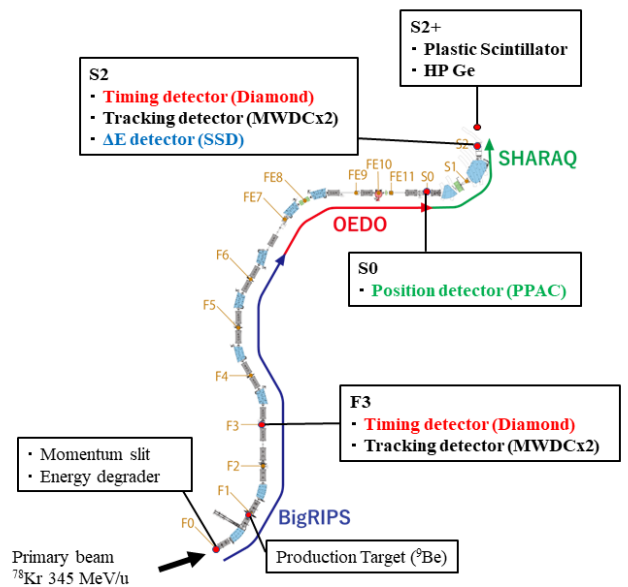


Figure 1: Schematic of the beamline and detector configuration used for mass measurement.

cles emitted from stopped ions, but also to identify isomers, which could shift the peak in the measured mass spectra.

Figure 2 shows the preliminary particle identification plot. Proton-rich Ti, Cr, and Fe isotopes were detected in the vicinity of the proton drip line. More than 30 reference masses widely distributed in proton and neutron numbers were also measured at the same time. The distribution of each nucleus along the x -axis, i.e. mass value, comes from the broadening of TOF due to trajectory differences. Therefore the mass spectrum can be corrected by trajectory information. Precise calibration analysis is now in progress.

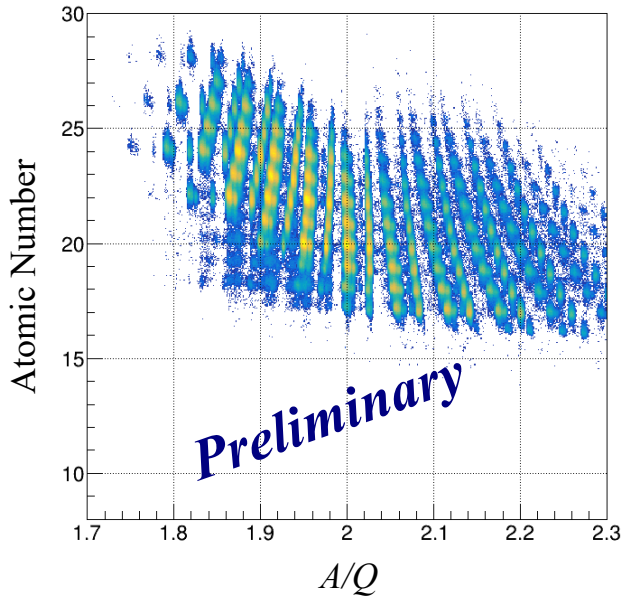


Figure 2: Particle identification plot.

References

- [1] V. I. Goldanskii *et.al.*, Nucl. Phys. **19**, 484 (1960).
- [2] C. Dossat *et.al.*, Phys. Rev. C. **72**, 054315 (2005).
- [3] K. Miernik *et.al.*, Eur. Phys. J. A **42**, 431-439 (2009).
- [4] S. Michimasa *et al.*, Phys. Rev. Lett. **121**, 022506 (2013).
- [5] S. Hanai, *et al.*, RIKEN Accel. Prog. Rep. **55** (2022).
- [6] S. Hanai, *et al.*, Nucl. Instrum. Methods Phys. Res. B **541** (2023).

Isomeric gamma-ray measurement system at S2+ in SHARAQ13 experiment

Y. Nakamura^{a,b}, M. Amitani^{a,b}, C. Fukushima^{a,b}, T. Tomiyama^{a,b}, S. Hanai^c, K. Kawata^c, S. Michimasa^c, D. Nishimura^{a,b,c}, K. Okawa^c, T.Y. Saito^c, R. Yokoyama^c, D.S. Ahn^d, H. Baba^b, T. Chillery^c, M. Dozono^{b,e}, F. Endo^{b,f}, M. Fukuda^{b,g}, N. Fukuda^b, M. Fukutome^{b,g}, T. Haginouchi^{b,f}, S. Hayakawa^c, Y. Hijikata^{b,e}, J. W. Hwang^b, E. Ideguchi^{b,h}, N. Imai^c, S. Ishio^{b,f}, N. Iwasa^{b,f}, K. Kameya^{b,f}, R. Kojima^c, K. Kusaka^b, J. Li^c, H. Nishibataⁱ, S. Ota^h, D. Suzuki^b, H. Suzuki^b, Y. Shimizu^b, S. Shimoura^{b,c,h}, T. Sumikama^b, H. Takahashi^{a,b}, H. Takeda^b, H. Tanaka^{b,j}, M. Tanaka^b, T. Teranishi^{b,i}, T. Uesaka^b, R. Urayama^{b,f}, K. Yako^c, Y. Yanagisawa^b, K. Yoshida^b, and M. Yoshimoto^b

^aDepartment of Natural Sciences, Tokyo City University

^bRIKEN Nishina Center

^cCenter for Nuclear Study, Graduate School of Science, the University of Tokyo

^dCenter for Exotic Nuclear Studies, Institute for Basic Science

^eDepartment of Physics, Kyoto University

^fDepartment of Physics, Tohoku University

^gDepartment of Physics, Osaka University

^hResearch Center for Nuclear Physics, Osaka University

ⁱDepartment of Physics, Kyushu University

^jFaculty of Arts and Science, Kyushu University

The mass of atomic nuclei is one of the most important physical quantities for understanding nuclear structure. Direct mass measurements for neutron-rich pf -shell nuclei were successfully performed with TOF- $B\rho$ method in SHARAQ spectrometer [1, 2]. For the experiments with secondary beam of heavier radioactive ions including the direct mass measurement, the confirmation of particle identification is critical. In this experiment, the particle identification can be confirmed by detecting delayed γ rays emitted from short-lived isomeric states of some of the fragments, which is called isomer tagging. Since the energies and half-lives of isomeric γ rays have specific values, the isomer tagging provides us with an exact fingerprint for the particle identification [3, 4]. In addition, the isomeric ratios are also crucial for determining the ground-state masses [2].

The mass measurement for proton-rich pf -shell nuclei in the vicinity of ^{47}Fe was carried out at OEDO-SHARAQ [5] in May-June 2022. The experimental setup for isomer tagging was installed at the downstream of the final focal plane of SHARAQ spectrometer (S2+), as shown in Fig. 1. An active stopper with two 10-mm-thick plastic scintillators was located at a 45 degree angle to the beamline. The signals of the stopper were read out by MPPCs attached both side of the scintillators. Two HPGe detectors, ORTEC GMX80P4-95-S (Ge1) and CANBERRA GX5019 (Ge2), were installed in close proximity of the active stopper, perpendicular to the beam direction. Two CeBr₃ scintillators with a diameter of 1 inch and a thickness of 1 inch equipped with a PMT (HAMAMATSU H7145MOD) were also placed along an axis tilted at 45 degree to the beamline. Between S2 and the active stopper, an Al energy degrader with a thickness of 3 mm was set for implanting RI beams in the center of the active stopper. Additionally, a veto scintillator was placed downstream of the active stop-

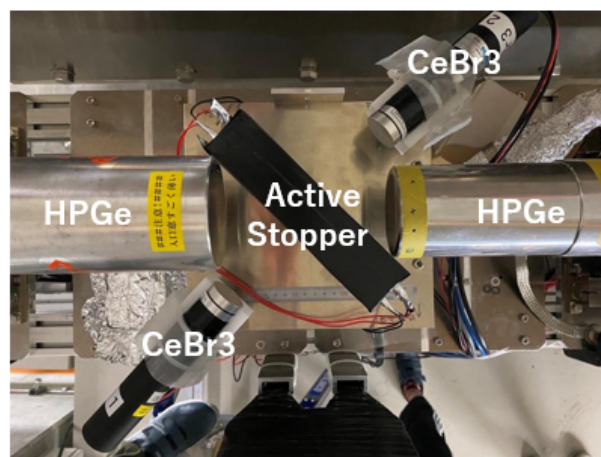


Figure 1: Experimental setup of delayed γ -ray spectroscopy at S2+.

per to identify events where beam particles penetrated the stopper. The energy and hit timing of the HPGe detectors (the CeBr₃ detectors and the active stopper) were recorded by a self-triggering DAQ system equipped with a digital signal processor (DSP) of Techno-AP APV8008 (APV8104-14 and APV8504-14). To optimize the energy resolutions of the DSP, each HPGe detector signal was split in two and recorded in channels with different dynamic energy ranges of 1500 keV and 5500 keV. The typical energy resolution of Ge1 (Ge2) at 1333 keV in FWHM were 2.2 keV (2.0 keV) for the 1500-keV range and 2.7 keV (2.4 keV) for the 5500-keV range, respectively.

To confirm the particle identification of the present experiment, we identified known isomers by using the isomer tagging system. Figure 2 shows the particle identification plot of the secondary beams in this experiment. Known

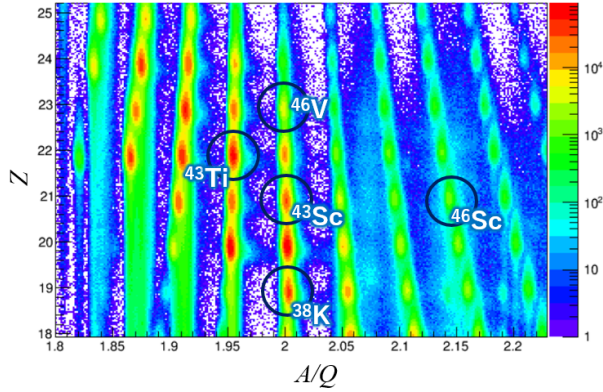


Figure 2: Particle identification plot of the secondary beams. Known isomeric- γ rays from circled isotopes were observed in this experiment.

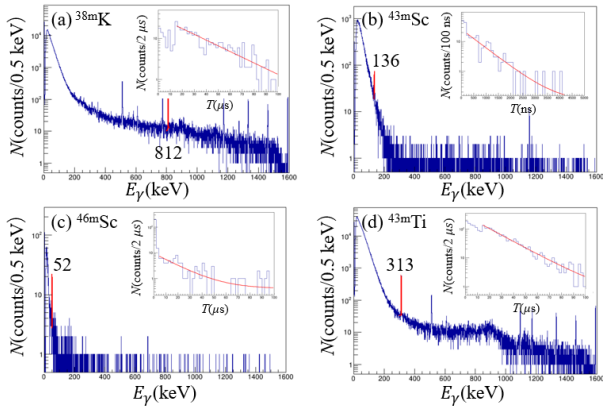


Figure 3: Energy spectra for isomeric γ rays from ^{38m}K , ^{43m}Sc , ^{46m}Sc , and ^{43m}Ti . Decay curves are also shown in these insets.

isomeric- γ rays from circled five isotopes of ^{38m}K , ^{43m}Sc , ^{46m}Sc , ^{43m}Ti and ^{46m}V were observed. The typical delayed γ -ray energy spectra for each of isomers are shown in Fig. 3. Decay curves are also shown in these insets. Table 1 shows the comparison of our preliminary results of γ -ray energies and half-lives of known isomers with reference data [6–9]. Our results are consistent with those from the references. Therefore, we successfully obtained reliable particle identification for widely distributed secondary beam species.

Data analysis with the CeBr_3 detectors and the active stopper are ongoing. It is expected that the active stopper will be used to identify the β -delayed γ rays as well as isomeric γ rays. Then, direct or β -delayed proton emissions may be observed by the stopper. The CeBr_3 detectors will help us to observe the γ - γ coincidence with HPGe detectors. Further analysis for the discovery of new isomeric states are also in progress. We will soon determine all the isomeric ratios of observed isomers for the direct mass measurement.

References

- [1] S. Michimasa *et al.*, Phys. Rev. Lett. **121**, (2018) 022506.

Table 1: Comparison of presents results of γ -ray energies and half-lives of known isomers with reference data [6–9].

Nuclide	$E_\gamma(\text{keV})$		$T_{1/2}$	
	Present	Reference	Present	Reference
^{38m}K	811.9(1)	811.9(2)	22(2) μs	21.95(11) μs
	151.5(1)	151.65(17)	370(40) μs	438(7) μs
^{43m}Sc	135.7(1)	135.6(1)	480(60) ns	}472(4) ns
	1158.1(1)	1157.5(1)	430(80) ns	
	1831.8(2)	1830.1(1)	450(80) ns	
^{46m}Sc	51.9(1)	52.011(1)	12(3) μs	9.4(8) μs
	312.6(1)	312.7(2)	13.4(8) μs	11.9(3) μs
^{43m}Ti	113.8(1)	114.7	510(40) ns	}556(6) ns
	1094.7(1)	1094.0	550(130) ns	
	1858.3(1)	1857.7	550(80) ns	
^{46m}V	801.4(1)	801.5(1)	0.89(8) ms	1.02(7) ms

- [2] S. Michimasa *et al.*, Phys. Rev. Lett. **125**, (2020) 122501.
[3] T. Ohnishi *et al.*, J. Phys. Soc. Jpn. **77**, 083201 (2008).
[4] S. Michimasa *et al.*, Proc. Sci., INPC2016, 106(2017).
[5] S. Hanai *et al.*, in this report.
[6] National Nuclear Data Center, The NuDAT 3.0 database, <https://www.nndc.bnl.gov/nudat3/>.
[7] J. Chen, Nucl. Data Sheets 152 (2018) 1.
[8] B. Singh and J. Chen, Nucl. Data Sheets 126 (2015) 1.
[9] S.-C. Wu, Nucl. Data Sheets 91 (2001) 11.
[10] M. Amitani *et al.*, in this report.

Measurement of double charge exchange (^{12}C , $^{12}\text{Be}(0_2^+)$) reaction aiming for the observation of double Gamow–Teller giant resonance

A. Sakaue for the RIBF-141R1 collaboration

Center for Nuclear Study, Graduate School of Science, University of Tokyo

The double Gamow–Teller (DGT) transition is a nuclear process such that the spin and isospin are changed twice by a $(\sigma\tau)^2$ operator without change of the orbital angular momentum, where σ and τ are the spin and isospin operators, respectively. A giant resonance which occupies most of the DGT transition strength is expected to exist in a high-excitation energy region [1], but it still remains unobserved. Experimental information of the DGTGR is potentially important for determining the nature of neutrinos. The transition strength and the centroid energy of the DGTGR are suggested to be strongly correlated with the nuclear matrix element of a neutrinoless double β decay [2], while theoretically predicted values of the nuclear matrix element have a large uncertainty depending on the chosen model [3].

We are aiming at the observation of the DGTGR using the double charge exchange reaction (^{12}C , $^{12}\text{Be}(0_2^+)$). This reaction is effective for the observation of the DGTGR for the following reasons. First, this reaction is expected to have a large cross section because the transition from $^{12}\text{C}(0_{g.s.}^+)$ to $^{12}\text{Be}(0_2^+)$ through the intermediate state of $^{12}\text{B}(1^+)$ is expected to be strong since these states are all dominated by $0\hbar\omega$ configurations. Second, we can utilize an isomeric decay of $^{12}\text{Be}(0_2^+)$, for the event selection. $^{12}\text{Be}(0_2^+)$ has a lifetime of 331 ± 12 ns and decays into the ground state by emitting an electron-positron pair [4]. Detecting back-to-back photons with an individual energy of 511 keV from the positron serves to tag the events of the double spin-flip mode.

We performed the experiment at the RI Beam Factory (RIBF) using the (^{12}C , $^{12}\text{Be}(0_2^+)$) reaction [5]. A primary beam of ^{12}C with the energy of 250 MeV/u bombarded a ^{48}Ca target of 10 mg/cm² thick with a graphene coating placed at F0 of BigRIPS. The momentum of the ejected ^{12}Be was analyzed by the magnets between F0 and F5, and it was measured as the horizontal position at the dispersive focal plane of F5. We used the DALI2 array for the detection of the delayed- γ rays and successfully identified the isomeric state of $^{12}\text{Be}(0_2^+)$.

Figure 1 shows the differential cross section of the $^{48}\text{Ca}(^{12}\text{C}, ^{12}\text{Be}(0_2^+))$ against the horizontal position at F5, F5X, for each scattering angle at the target. In a preliminary calibration, 1 mm in this distribution corresponds to 0.81 MeV in the excitation energy of ^{48}Ti , and the ground state of ^{48}Ti is 27.7 mm in the position at F5. The background events of the $^{12}\text{C}(^{12}\text{C}, ^{12}\text{Be})^{12}\text{O}_{g.s.}$ reaction coming from the graphene sheet attached to the ^{48}Ca target will be around -17 mm.

We obtained the angular distributions for the integrated cross section focusing four regions of F5X at 10-mm intervals, namely, from -20 to -10 mm (denoted $(-20, -10)$

hereafter), $(-10, 0)$, $(0, 10)$, and $(10, 20)$ as shown in histograms in Fig. 2. The corresponding excitation energy regions of ^{48}Ti in MeV are $(30.6, 38.7)$, $(22.5, 30.6)$, $(14.4, 22.5)$, and $(6.3, 14.4)$.

In order to extract the DGT transition component from the experimental data, we compared the angular distribution with those calculated by ECIS [6] in which the coupled channel calculation is performed. We consider the initial state of $^{48}\text{Ca}(0^+)+^{12}\text{C}(0^+)$, the intermediate state of $^{48}\text{Sc}(1^+)+^{12}\text{B}(1^+)$, and the final state of $^{48}\text{Ti}(0^+)+^{12}\text{Be}(0^+)$ as each channel. We assumed two types of the transfer of the orbital angular momentum ΔL in the calculation. First type is such that in both of the transition from the initial state to the intermediate state and from the intermediate state to the final state, $\Delta L=0$ ($[\Delta L=0] \times 2$), which corresponds to the DGT transition. The other type is $\Delta L=2$ for the transition from the initial state to the intermediate state, and $\Delta L=0$ for from the intermediate state to the final state ($[\Delta L=2] + [\Delta L=0]$). The calculated angular distribution has a peak at 0° for $[\Delta L=0] \times 2$ while 0.7° for $[\Delta L=2] + [\Delta L=0]$.

We decomposed the experimental angular distribution into these components of ΔL . The proportions for each ΔL is determined by the least square method. In Fig. 2, the experimental data, the fitted results of $[\Delta L=0] \times 2$, $[\Delta L=2] + [\Delta L=0]$, and added result of each component are shown by black histograms, black dotted lines, blue dashed lines, and magenta solid lines, respectively. For the region of F5X= $(-10, 0)$ and $(0, 10)$, there seems to be the DGT component by several tens of percent within the experimental cross section. For F5X= $(-20, -10)$, there seems to be the contamination coming from ^{12}C of the graphene. However, the strength coming from ^{48}Ca might remain significantly according to the result of the background measurement. It is still under discussion for this region.

We are now dedicated to the finalization of the results and further discussions.

References

- [1] N. Auerbach, L. Zamick, and D. Zheng, *Ann. Phys.* **192**, 77 (1989).
- [2] N. Shimizu, J. Menéndez, and K. Yako, *Phys. Rev. Lett.* **120**, 142502 (2018).
- [3] J. Engel and J. Menéndez, *Rep. Prog. Phys.* **80**, 046301 (2017).
- [4] S. Shimoura *et al.*, *Phys. Lett. B* **654**, 87 (2007).
- [5] A. Sakaue for the RIBF-141R1 collaboration, *CNS Rep.* **101**, 11 (2023).
- [6] J. Raynal, *Phys. Rev. C* **23**, 2571 (1981).

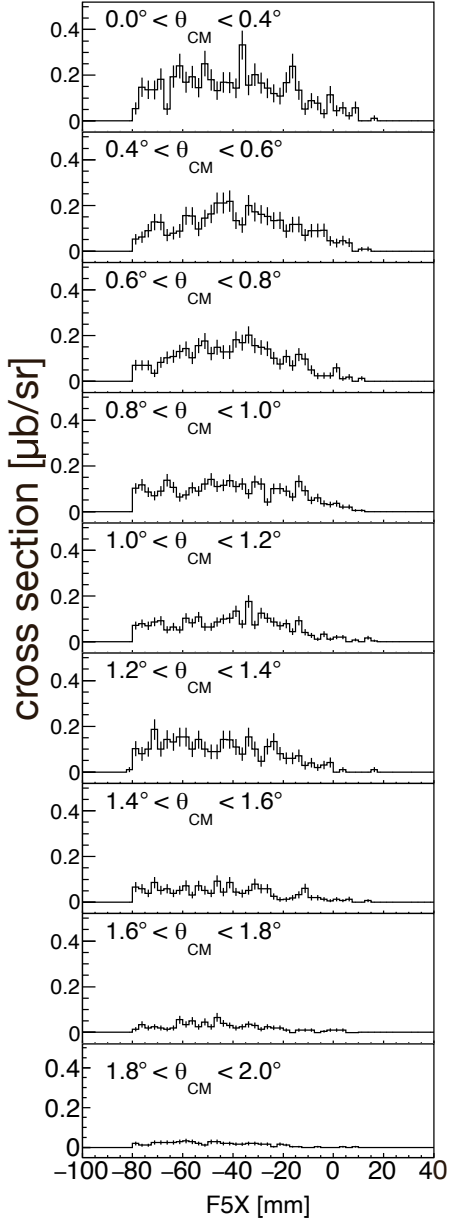


Figure 1: Position distribution at F5 for each scattering angle, θ_{CM} , from 0.0 to 0.4° for the most forward angle, and at 0.2° intervals for the following angle.

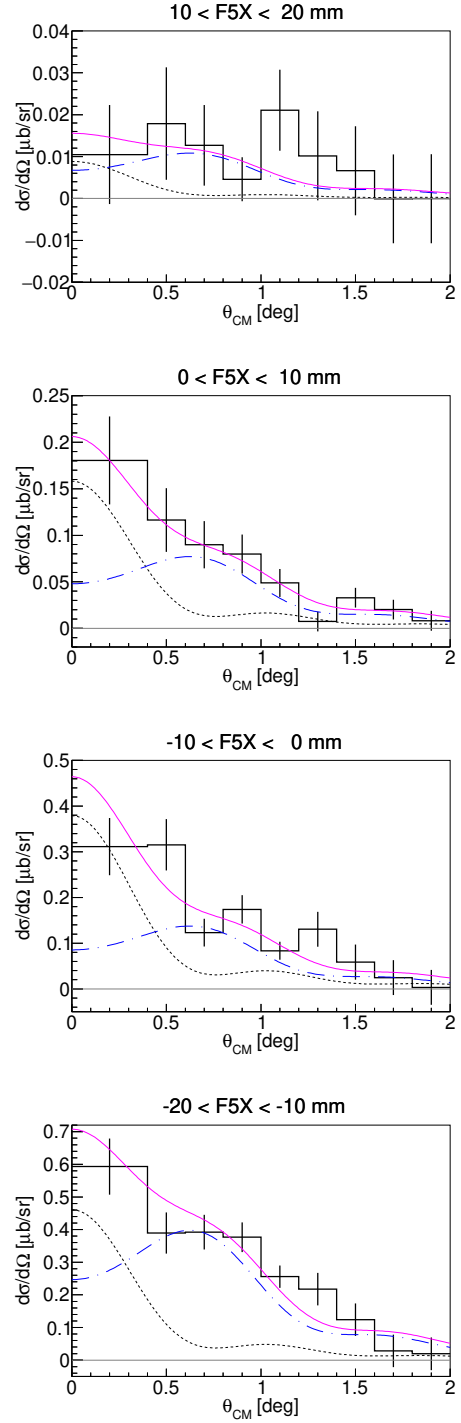


Figure 2: Angular distribution of the cross section integrated within the each region of the position of F5X=(10, 20), (0, 10), (-10, 0), and (-20, -10) in mm (from top to bottom). The decomposed results are also shown.

Measurement of fusion-evaporation cross sections in $^{136}\text{Xe}+^{64}\text{Zn}$ system using inverse kinematics

J. T. Li, N. Imai, R. Yokoyama, T. Chillery, S. Michimasa, S. Hanai, T. Saito, R. Kojima, H. Yamaguchi, S. Shimoura, D. Nishimura^a, S. Sugawara^a, M. Dozono^b, K. Hagino^b, D. Suzuki^c, Y. Watanabe^d, Y. Aritomo^e, S. Sakaguchi^f, S. Ota^g, M. Shiraishi^h, E. Takadaⁱ,

Center for Nuclear Study, Graduate School of Science, University of Tokyo, ^aTokyo City University, ^bKyoto University, ^cRIKEN Nishina Center, ^dKEK, ^eKindai University, ^fKyushu University, ^gResearch Center for Nuclear Physics, Osaka University, ^hRikkyo University, ⁱQST-HIMAC

Owing to the developing technologies of Radioactive Isotope Beams (RIB) around the world, fusion-evaporation reaction using neutron rich RIB provides an approach in the search for the Island of Stability, which is one of the most attractive problems in experimental nuclear physics. Doubly-magic ^{132}Sn ($Z = 50, N = 82$) beam was proposed in reaction $^{132}\text{Sn} + ^{160}\text{Gd}$ [1] to reach the edge of the Island of Stability. Since ^{132}Sn is located on the fission peak of primary beam nuclei ^{238}U , the intensity of ^{132}Sn beam is larger than that of neutron rich Ca beam by four orders of magnitude at RIBF, RIKEN. However, the reducing mass asymmetry of the entrance channel will affect the probability of forming the Compound Nuclei (CN). Hence, pioneering studies of more symmetric systems are mandatory.

To design the experiments to study Very/Super Heavy region and towards the Island of Stability, we need a reaction model that can precisely give the cross section. However, the dynamics of fusion reactions has not been established yet. In particular, a quantitative understanding of the so-called fusion hindrance effect is far from being achieved due to the lack of experimental studies.

Several experiments have been designed to quantitatively evaluate the fusion hindrance effect in near-symmetric system. As the first step, the setup and methodologies were commissioned in an experiment at HIMAC to study the fusion-evaporation reaction $^{136}\text{Xe} + ^{\text{nat}}\text{Zn}$.

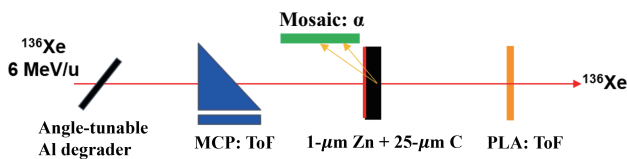


Figure 1: Overview of the experimental setup.

Figure 1 shows schematically the experimental setup. 6-MeV/u- $^{136}\text{Xe}^{42+}$ beam was delivered by the LINAC. Since it was difficult to change the beam energy in the accelerator, an angle-tunable aluminum degrader was used to tune the beam energy, which was then determined by the ToF measurement using a Micro Channel Plate (start) and a Plastic Scintillator (stop). Three beam energies ($E_{\text{Lab}} = 598, 621$ and 651 MeV) were tuned and applied in the physics measurement. A natural zinc target with a thickness of $1 \mu\text{m}$ was backed with a $25\text{-}\mu\text{m}$ -thick graphene sheet. The thickness of the target and the back material were chosen so that after the reaction, the beam would pass through

while Evaporation Residues (ERs) would be stopped in the graphene sheet and went through α decay. A newly-developed mosaic-type detector array [2] consisting of 128 Silicon photodiodes (Mosaic) and two large-size pad type Si PIN Photodiode (Pad) was placed upstream of the target to measure the α decay of ERs. Owing to the inverse kinematics, Si detectors were totally free from the elastic scattering events. A Coaxial Ge detector was used to measure the β -delayed γ rays from relatively long-lived ($T_{1/2} > 10$ min) daughter and grand-daughter nuclei of ERs.

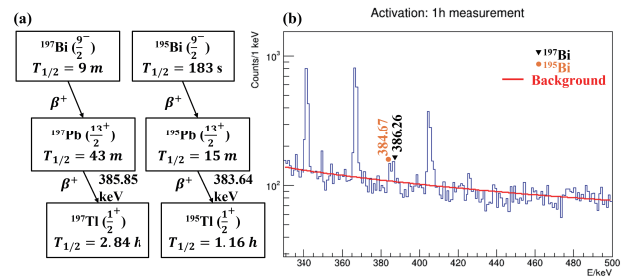


Figure 2: (a) Partial decay scheme of ^{195}Bi and ^{197}Bi ; (b) Off-line γ energy spectrum of one-hour measurement starting from 30 minutes after beam stopped. The red curve denotes the estimated background.

The beam size at the upstream of the degrader is 1 cm in diameter, while due to the multiple scattering of the beam in the degrader and the large distance between the degrader and the target, the beam spot was enlarged more than twice on target, thus part of the beam ($\sim 10\%$) hit the target holder, the material of which is natural copper. Partial ERs: ^{195}Bi and ^{197}Bi produced in the fusion reaction between ^{136}Xe and $^{63,65}\text{Cu}$ were identified in the activation measurement, as shown in Fig. 2. Unfortunately, no β -delayed γ rays associated with ERs produced in $^{136}\text{Xe} + ^{\text{nat}}\text{Zn}$ were observed since the beam interacted with the Al degrader with a huge cross section ($\sim 1\text{b}$) and unstable products were stopped in the target, causing the huge background in the activation measurement.

To measure the α decay of ERs, the pulsed beam with 3 spills on and 3 spills off (1.65 s/spill) was applied, as shown in Fig. 3, where the x axis is Δt , defined as the time difference between the timestamp of each event and the start of each pulse. It can be seen that even in the beam-off period, there are some small peaks which may be caused by the beam leakage. Figure 4(a) shows the experimental α energy spectrum measured by the Pad detector and Figure 4(b) shows the an-

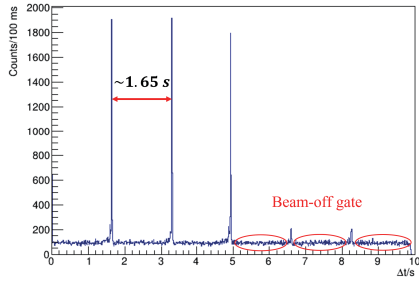


Figure 3: Beam pulsing mode.

gular dependence of α particles measured by the Mosaic detector, where y axis is the energy and x axis is the distance from hit position on detector to the target plane along the beam axis, as shown in the inset. Due to the low statistics, no clear angular dependence was observed. Since we

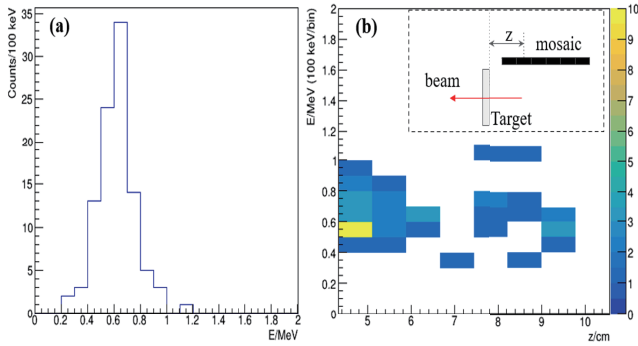


Figure 4: Experimental α energy spectra measured by the (a) Pad; (b) Mosaic detector at $E_{Lab} = 598$ MeV.

used quite thick back material to stop ERs, energy loss of α particles is rather large, therefore the Monte-Carlo simulation was performed to reproduce the experimental spectra. Figure 5 shows one optimum fitting using 6.5-MeV α particles emitted by the ER ^{196}Po , where k_r is a reduced factor to multiply the range of ERs calculated by ATIMA code.

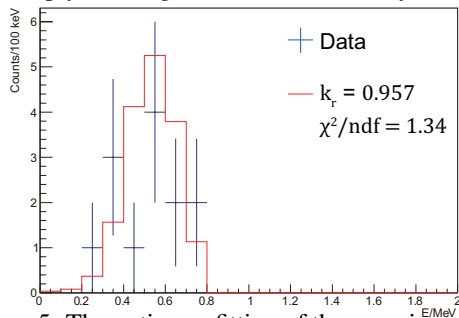


Figure 5: The optimum fitting of the experimental spectrum measured by the Pad detector at $E_{Lab} = 598.4$ MeV.

Figures 6(a) and (b) present the measured excitation function of $^{136}\text{Xe} + ^{63}\text{Cu}$ and $^{136}\text{Xe} + ^{64}\text{Zn}$, respectively. For the system $^{136}\text{Xe} + ^{63}\text{Cu}$, cross section values are averaged values in the effective thickness of the Cu target holder, which was defined as beam energy ranging from incident energy to the Bass fusion barrier. For the system $^{136}\text{Xe} + ^{64}\text{Zn}$, cross section values are averaged values in the target thickness. In the statistical model software PACE4, the input fission barrier height (B_f) of the CN was tuned to reproduce the experimental cross sections. It can

be seen that for $^{136}\text{Xe} + ^{63}\text{Cu}$, B_f calculated by Möller [3] reproduced the experimental results while in the system $^{136}\text{Xe} + ^{64}\text{Zn}$, the experimental cross sections agreed with the B_f calculated by the Liquid Drop Model (LDM).

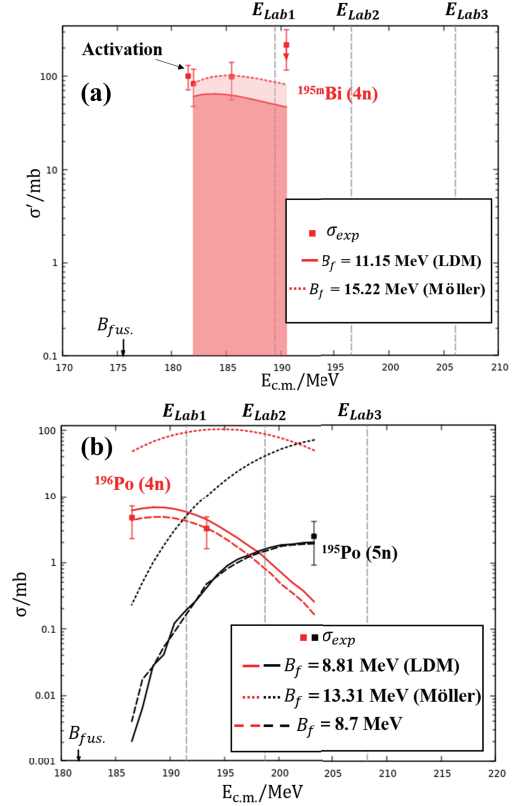


Figure 6: Extracted excitation functions in (a) $^{136}\text{Xe} + ^{63}\text{Cu} \rightarrow ^{199}\text{Bi}^*$ and (b) $^{136}\text{Xe} + ^{64}\text{Zn} \rightarrow ^{200}\text{Po}^*$.

In conclusion, a fusion reaction using low-energy ^{136}Xe beam was performed at HIMAC. Partial ERs produced in the reactions between ^{136}Xe beam and ^{nat}Cu , ^{nat}Zn targets were identified by the in-beam α measurement and the off-line activation measurement, independently. Cross sections deduced from the both measurements above are consistent at $E_{Lab} = 598.4$ MeV, and the excitation functions deduced based on the in-beam α measurement were reproduced by tuning the input fission barrier height of CN in PACE4. Our results suggest that the fusion-evaporation reactions of the systems $^{136}\text{Xe} + ^{nat}\text{Cu}$, ^{nat}Zn were not hindered significantly, and PACE4 gave a fair prediction of the reaction cross sections of the systems above.

References

- [1] T. Nomura and Y. Abe. Journal of the Physical Society of Japan. **50**, 9(2005).
- [2] J. Li et al, CNS Annual Report 2021, 39 (2023).
- [3] P. Möller et al. Phys. Rev. C, **91**,024310(2015).

In-beam γ -ray spectroscopy of ^{32}Mg

N. Kitamura, K. Wimmer^{a,b,c,d}, T. Miyagi^e, A. Poves^f, N. Shimizu, J. A. Tostevin^h,
V. M. Bader^{d,g}, C. Bancroft^c, D. Barofsky^c, T. Baugher^{d,g}, D. Bazin^d, J. S. Berryman^d,
V. Bildsteinⁱ, A. Gade^{d,g}, N. Imai, T. Kröll^j, C. Langer^d, J. Lloyd^c, E. Lunderberg^{d,g}, F. Nowacki^k,
G. Perdikakis^{c,d}, F. Recchia^d, T. Redpath^c, S. Saenz^c, D. Smalley^d, S. R. Stroberg^{d,g}, Y. Utsuno^l,
D. Weisshaar^d, and A. Westerberg^c

Center for Nuclear Study, University of Tokyo

^aInstituto de Estructura de la Materia, CSIC

^bDepartment of Physics, University of Tokyo

^cDepartment of Physics, Central Michigan University

^dNational Superconducting Cyclotron Laboratory, Michigan State University

^eInstituto de Estructura de la Materia, CSIC

^fDepartamento de Física Teórica and IFT UAM-CSIC

^gDepartment of Physics and Astronomy, Michigan State University

^hDepartment of Physics, University of Surrey

ⁱDepartment of Physics, University of Guelph

^jInstitut für Kernphysik, Technische Universität Darmstadt

^kInstitut Pluridisciplinaire Hubert Curien

^lAdvanced Science Research Center, Japan Atomic Energy Agency

The disappearance of the canonical magic numbers, such as 8, 20, 28, has been observed in neutron-rich unstable nuclei [1]. In the area known as the “island of inversion” [3], ground states of neutron-rich *sd*-shell nuclei are predominantly characterized by intruder configurations that involve *fp* orbitals across the $N = 20$ shell gap, leading to the breakdown of the neutron magic number $N = 20$. This phenomenon can be attributed to the evolving shell structure as one moves away from stability [2], and the island of inversion continues to be an important testing ground for understanding the nuclear interactions and correlations driving these significant changes in shell structure.

The nucleus ^{32}Mg , located at the heart of the island of inversion, is a pivotal isotope in this region. While its ground state is strongly deformed, the remnants of the $N = 20$ shell closure are thought to manifest in excited 0^+ states, associated with a spherical shape [4, 5]. The competition of these distinct shapes, and consequently the emergence of the island of inversion, is considered to strongly depend on the delicate balance between the $2p2h$ intruder and $0p0h$ normal configurations. However, recent theoretical studies suggest that the inclusion of stronger mixing, particularly $4p4h$ configurations, may be essential in describing the $N = 20$ island of inversion [6, 7].

Discriminating between various nuclear models requires comparison with high-quality experimental data. To this end, detailed in-beam γ -ray spectroscopy of ^{32}Mg was performed. Two different reaction probes, the one-neutron (two-proton) knockout reactions on ^{33}Mg (^{34}Si), each sensitive to intruder (normal) configurations, were used to populate states in ^{32}Mg . The first results were reported in Reference [8]. The subsequent publication, Reference [9], provides more comprehensive information about this study.

The experiment was performed at the National Superconducting Cyclotron Laboratory at Michigan State University. Secondary beams of ^{33}Mg and ^{34}Si were produced by fragmenting a ^{48}Ca beam at 140 MeV/nucleon on a ^9Be primary target. The beams of ^{33}Mg and ^{34}Si were then directed onto a ^9Be secondary target with a thickness of 375 mg/cm² to induce nucleon knockout reactions. The outgoing ions of ^{32}Mg were identified and momentum-analyzed by the S800 spectrograph. The secondary reaction target was surrounded by an array of γ -ray detectors, Gamma-Ray Energy Tracking In-beam Nuclear Array, GRETINA [10]. By utilizing its γ -ray interaction position sensitivity, the Doppler correction of γ rays emitted from the fast outgoing nucleus was performed on an event-by-event basis. We note that the experimental setup is identical to a previous study described in Reference [11], but with different rigidity settings of the beamline and spectrograph.

The strong selectivity of the one-neutron and two-proton knockout reactions, as well as the high statistics collected in the present measurement, enabled us to significantly update the level scheme (see Figure 1). Parallel momentum distributions associated with each state were extracted from the experimental data. Through comparisons with eikonal-based reaction model calculations, spins and parities were assigned to each level.

The use of one-neutron knockout has provided evidence supporting a $3/2^-$ spin-parity assignment for the ground state of ^{33}Mg , which points to its $3p2h$ nature. Consequently, one-neutron knockout is expected to preferentially populate $3p3h$ negative-parity states in ^{32}Mg . Such states were indeed identified, with the lowest-energy negative-parity state established at 2858 keV. This observation highlights the evolving shell structure as one approaches the

Direct measurement of the $^{14}\text{O}(\alpha,p)^{17}\text{F}$ reaction with the TexaAT_v2 detector

S. Ahn^a, C. Park^{a,b}, D. Kim^a, K.I. Hahn^a, M. Avila^c, S. Bae^a, M. Barbui^d, D.W. Bardayan^e, J. Bishop^d, S.M. Cha^a, K.Y. Chae^f, A. Chen^g, T. Chillery^h, S. Doⁱ, N.N. Duy^j, G.M. Gu^f, S. Hayakawa^h, B. Hongⁱ, N. Imai^h, N. Iwasa^j, A. Kimⁱ, C.H. Kim^f, M.J. Kim^f, S.H. Kim^f, Y. Kim^a, N. Kitamura^h, Y. Koshchiy^d, S. Kubono^k, M.L. Cognata^l, H. Lee^m, B. Moon^a, T. Nakamura^m, K. Okawa^h, C.E. Parker^d, A. Psaltisⁿ, G.V. Rogachev^{d,o}, M. Roosa^{d,o}, M. Sasano^h, M. Sferrazza^p, H. Yamaguchi^h and Q. Zhang^h

^aCenter for Exotic Nuclear Studies, Institute for Basic Science, Daejeon, Republic of Korea

^bDepartment of Physics, Ewha Womans University, Seoul, Republic of Korea

^cArgonne National Laboratory, Argonne, IL, USA

^dCyclotron Institute, Texas A&M University, College Station, TX, USA

^eDepartment of Physics & Astronomy, University of Notre Dame, Notre Dame, IN, USA

^fDepartment of Physics, Sungkyunkwan University, Suwon, Republic of Korea

^gDepartment of Physics and Astronomy, McMaster University, Hamilton, Ontario, Canada

^hCenter for Nuclear Studies, University of Tokyo, Tokyo, Japan

ⁱDepartment of Physics, Korea University, Seoul, Republic of Korea

^jDepartment of Physics, Tohoku University, Sendai, Miyagi, Japan

^kRIKEN Nishina Center, Wako, Saitama, Japan

^lINFN, Laboratori Nazionali del Sud, Catania, Italy

^mDepartment of Physics, Tokyo Institute of Technology, Tokyo, Japan

ⁿTriangle Universities Nuclear Laboratory, Duke University, Durham, NC, USA

^oDepartment of Physics & Astronomy, Texas A&M University, College Station, TX, USA

^pDépartement de Physique, Université Libre de Bruxelles, Bruxelles, Belgium

1. Introduction

Type I X-ray bursts are well known explosive stellar events in the Universe and they occurred on the surface of accreting neutron stars from a binary companion [1]. While the bursts are powered by many nuclear reactions including the triple-alpha reaction, the p- and the rp-process [2], large uncertainties of their reaction rates cause difficulties when predicting light curves of X-ray bursts to compare with observations. Therefore, it is important to understand these nuclear reactions involved in crustal processes in order to interpret properties of neutron stars such as accreted composition, source distances, and composition of the burst ashes [3].

The large uncertainties of the reaction rates are due to the nucleosynthesis flow driven toward the proton-drip line by the αp -process and the rapid proton capture process (rp-process). Recent sensitivity studies [4, 5] have shown that there are important astrophysical (α, p) reaction rates affecting a large variation of energy generation and final ash in X-ray burst models. Among the list of key reactions from the Multi-zone X-ray Burst model, the $^{14}\text{O}(\alpha, p)^{17}\text{F}$ reaction was found to produce significant changes (7%) in calculated luminosity, and a direct measurement of its total cross section has been performed with a relatively large uncertainty [6].

The reaction was also emphasized as a key determination of the alternate break-out path from the hot CNO cycle to the rp-process at sufficiently high temperatures ($T_9 > 0.5$) and high densities because the α capture on ^{14}O and ^{15}O

competes favorably with β decay [7].

The spin and parity of a resonance state at $E_x = 6.15$ MeV plays an important role but recently the spin-parity assignment was questioned in Ref. [8]. In order to constrain the astrophysical reaction rate, the total cross section measurement along the large range of E_{cm} is necessary.

The $^{14}\text{O}(\alpha, p)^{17}\text{F}$ cross sections are calculated using AZURE R-Matrix code [9] and TALYS-1.95 [10], and plotted on top of previously measured total cross sections [6, 11, 12] as shown in Fig. 1. Due to the different frameworks between the AZURE and the TALYS-1.95, the results show a discrepancy of two orders of magnitude by maximum and this implies the importance of the direct measurement. Furthermore, two cross section measurements from Ref. [11, 12] show large disagreements with the data from Ref. [6] at high energy range ($2 \text{ MeV} \leq E_{cm} \leq 2.8 \text{ MeV}$) whereas the two of them covering the low energy range ($1 \text{ MeV} \leq E_{cm} \leq 1.5 \text{ MeV}$) are somewhat in agreement to each other, encouraging another study to confirm the reliability of measurements.

To address the uncertainties of the $^{14}\text{O}(\alpha, p)^{17}\text{F}$ cross section, a direct cross section measurement was performed at CNS RI beam separator (CRIB), RIKEN. In this manuscript, we report its experimental setup and the status of data analysis.

2. Experimental Setup

The schematic diagram of experimental setup is shown in Fig. 2. In order to produce the ^{14}O beam for the exper-

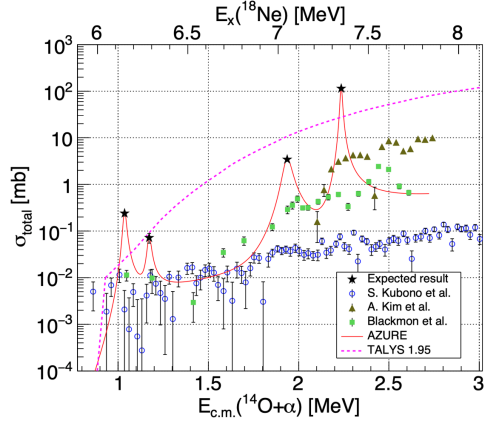


Figure 1: Calculated total cross sections of $^{14}\text{O}(\alpha,p)$ reaction and previous measured data. The measured cross sections between $E_{cm} = 0.5$ MeV and 1.3 MeV show deviations from the calculated ones and have relatively large uncertainty. The error bars on the expected cross sections from this proposed experiment are based on the statistical uncertainty.

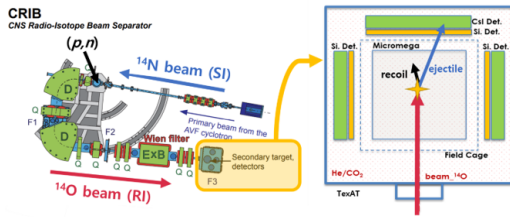


Figure 2: A schematic diagram of the CRIB beam-line and experimental setup for the $^{14}\text{O}(\alpha,p)^{17}\text{F}$ reaction. The energy of ^{14}N primary beam was chosen to maximize the ^{14}O production from the $^1\text{H}(^{14}\text{N}, ^{14}\text{O})n$ reaction.

iment, a ^{14}N beam with the energy of 8.40 MeV/u and H_2 gas cell target were used. Also, Texas Active Target Time Projection Chamber (TexAT) was used as a reaction target and a charged particle detector [13] as shown in Fig. 3. The detector was developed at Texas A&M University, and upgraded to Texas Active Target v2 (TexAT_v2) at the Center for Exotic Nuclear Studies (CENS), Institute for Basic Science (IBS) to optimize the detection efficiency for the (α,p) cross section measurement [14]. The energy and position resolution of detected charged particles from the reaction are enhanced thanks to the three-dimensional tracking of the particles. Along with the segmented silicon and the CsI(Tl) detectors around the field cage, TexAT enables measuring more precise cross sections as a function of center-of-mass energy. In order to manage about 2500 channels from various detectors, the GET electronics is used with the GANIL data acquisition system. Two Parallel plate avalanche counters (PPAC) were installed at the upstream of the TexAT_v2 chamber to measure the beam identification. Also, a thin plastic scintillator ($2 \mu\text{m}$) with SiPM readout sensor (BM) was installed along the beam axis right behind the window of the TexAT_v2 chamber to monitor beam intensity and



Figure 3: A front view of TexAT_v2. The field cage is located at the middle of the detector and surrounded by Si and CsI(Tl) detectors.

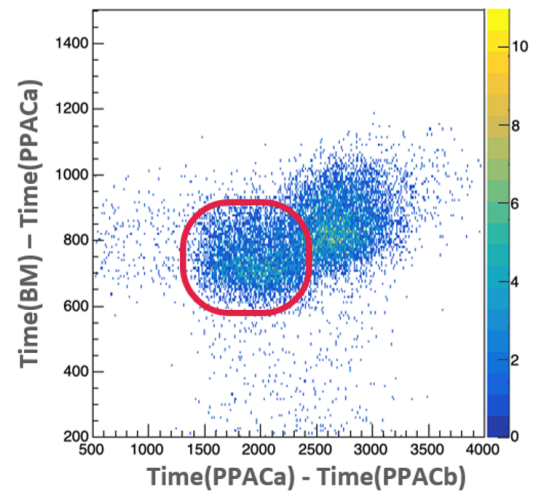


Figure 4: A beam particle identification plot using the timing information from PPAC a, PPAC b and BM. The red circle represents events of ^{14}O beam particles.

to correlate beam particles entered in the chamber. The ^{14}O beam energy after the window was 3.36 MeV/u, corresponding to $E_{cm} = 10.45$ MeV and TexAT_v2 measured proton tracks from the reaction. A silicon detector array and a CsI(Tl) detector array around the active area provide the total energy deposition of light particles and particle identification if a particle escapes the active TPC volume.

3. Preliminary Results of Data Analysis

Once all the data transfer and data conversion from the raw format to ROOT format were completed, the beam particle identification and good event identification such as proton or α -particle hits in the Si detectors were performed. The energy calibration of all Si detectors and forward CsI(Tl) detectors was also performed with a calibrated ^{241}Am source.

The beam identification plot using the time of flight between PPAC a and PPAC b as well as the time difference between PPAC a and BM is shown in Fig. 4. Also, the particle identification plot of light particles detected by Si detectors is used to find proton or α -particle events as shown in Fig. 5.

Using the gated proton or α -particle events, the particle

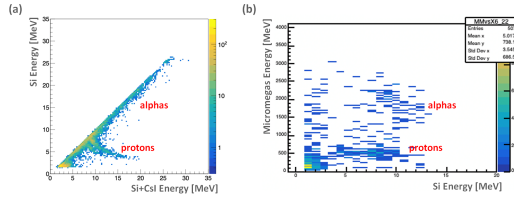


Figure 5: (a) A particle identification plot using Forward Si energy and sum of Forward Si and Forward CsI(Tl) energy. (b) A particle identification plot using averaged energy from Micromegas and X6 Si energy.

track could be plotted and its reaction vertex could be found matched with the beam track as a next step. Further analysis such as the efficiency of the detector and excitation functions is necessary to improve the existing $^{14}\text{O}(\alpha,p)^{17}\text{F}$ cross section data.

In conclusion, due to the importance of low uncertainty in $^{14}\text{O}(\alpha,p)^{17}\text{F}$ cross section related to the Type I X-ray bursts, the direct cross section measurement of the cross section has been studied at the CRIB, RIKEN, and data analysis is in progress.

References

- [1] W. H. G. Lewin *et al.*, Space Sci. Rev. **62**, 223 (1993).
- [2] H. Schatz and K. E. Rehm, Nucl. Phys. A **777**, 601 (2006).
- [3] D. K. Galloway, Astrophys. J. **601**, 466 (2004).
- [4] A. Parikh *et al.*, Astrophys. J. Suppl. Ser. **178**, 110 (2008).
- [5] R.H. Cyburt *et al.*, Astrophys. J. **830** (2) (2016) 55.
- [6] S. Kubono *et al.*, Eur. Phys. J. A **27**, s01, 327-332 (2006).
- [7] R. K. Wallace and S. E. Woosley, Astro. J. Suppl. Ser. **45**, 389 (1981).
- [8] J. J. He *et al.*, arXiv:1001.2053v1.
- [9] R. E. Azuma *et al.*, Phys. Rev. C **81**, 045805 (2010).
- [10] Talys 1.95, https://tendl.web.psi.ch/tendl_2019/talys.html.
- [11] A. Kim *et al.*, Phys. Rev. C **92**, 035801 (2015).
- [12] J. C. Blackmon *et al.*, Nucl. Phys. A **718**, 127c (2003).
- [13] E. Koshchiy *et al.*, Nucl. Inst. and Meth. A **957**, 163398 (2020).
- [14] C. Park *et al.*, Nucl. Inst. and Meth. B **541**, 221 (2023).

Direct measurement of the $^{26}\text{Si}(\alpha, p)^{29}\text{P}$ reaction at CRIB for the nucleosynthesis in the X-ray bursts

K. Okawa^a, M. J. Kim^b, K. Y. Chae^b, S. Hayakawa^a, S. Adachi^c, S. M. Cha^d, T. Chillery^a, N. N. Duy^b, T. Furuno^c, G. M. Gu^b, S. Hanai^a, N. Imai^a, D. Kahl^e, T. Kawabata^c, C. H. Kim^b, D. Kim^d, S. H. Kim^b, S. Kubono^f, M. S. Kwag^b, J. Li^a, N. R. Ma^a, S. Michimasa^a, K. Sakanashi^c, H. Shimizu^a, O. Sirbu^e, N. K. Uyen^b, H. Yamaguchi^a, R. Yokoyama^a, and Q. Zhang^a

^aCenter for Nuclear Study, Graduate School of Science, University of Tokyo

^bDepartment of Physics, Sungkyunkwan University

^cDepartment of Physics, Osaka University

^dCenter of Exotic Nuclear Studies, Institute for Basic Science (IBS)

^eExtreme Light Infrastructure Nuclear Physics (ELI-NP)

^fRIKEN Nishina Center

1. Introduction

Type I X-ray bursts (XRBs) are thermonuclear explosions that have been observed many times since the Astronomical Netherlands Satellite (ANS) observed the first XRBs [1]. Cyburt *et al.* [2] investigated the sensitivity of the nuclear reactions to the light curve of XRBs, which is the time variation of the X-ray flux. The study suggested that the $^{26}\text{Si}(\alpha, p)^{29}\text{P}$ reaction has one of the largest effects on the light curve. In order to evaluate the reaction rate experimentally, Almaraz-Calderon *et al.* [3] studied the energy level structure of ^{30}S using $^{28}\text{Si}(^3\text{He}, n)^{30}\text{S}$ and $^{32}\text{S}(p, t)^{30}\text{S}$ transfer reactions. However, the energy levels they measured were up to 12.04 MeV and the data were insufficient data above the α -threshold (9.343 MeV), corresponding to the important energy region for estimating the $^{26}\text{Si}(\alpha, p)^{29}\text{P}$ reaction rate. Therefore, we performed a direct measurement of the $^{26}\text{Si}(\alpha, p)^{29}\text{P}$ reaction to get information of the cross section at high energy region (excited energy < 16.8 MeV).

2. Experimental setup

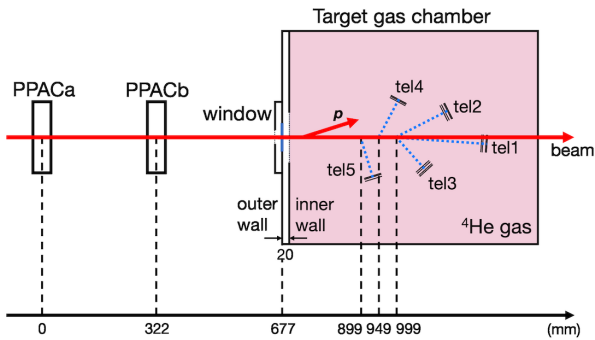


Figure 1: Experimental setup at the target chamber.

The experiment was performed at the Center for Nuclear Study Radioisotope Beam Separator (CRIB) [4]. CRIB produced a ^{26}Si beam with a typical intensity of 3.2×10^4 pps and a purity of 29%, which bombarded the ^4He gas target at about 250 Torr. As shown in Figure 1, beam tracking information was measured by two delay-line Parallel

Plate Avalanche Counters (di-PPACs) [5], and reaction particles were measured by five ΔE -E telescopes each of which consist of three or four Silicon detectors. A Mylar foil ($\text{C}_{10}\text{H}_8\text{O}_4$) was used for the window to seal the ^4He gas target. We used the thick target method [6] to measure a wide range of the reaction energy, and with this experimental setup, the $^{26}\text{Si}(\alpha, p)^{29}\text{P}$ reaction was measured up to the center-of-mass energy of about 7.5 MeV ($T \sim 9$ GK).

3. Analysis

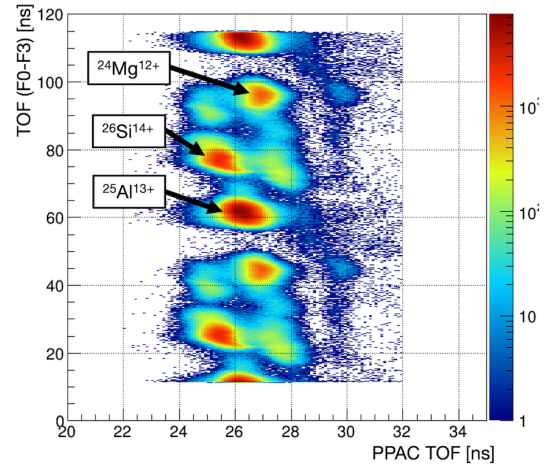


Figure 2: Beam identification at the target position. The positions of ^{26}Si , ^{25}Al and ^{24}Mg are shown in the figure as typical beam ions.

CRIB could not completely separate the ^{26}Si ion, and other beam ions also entered in the target chamber. Therefore, it was necessary to identify the beam particles. Figure 2 shows the beam identification using the time difference from the primary target to the PPACb (y-axis) versus the time difference between PPACa and PPACb (x-axis). Simulations were performed for various beam particles and compared with this results, and ^{26}Si ions were identified.

Then, we selected proton events with the ^{26}Si beam gate using ΔE -E identification to select the $^{26}\text{Si}(\alpha, p)^{29}\text{P}$ reaction. We also performed background measurements with

Ar gas at 54.9 Torr to evaluate background proton events, and the same process was applied to these data. Figure 3 shows an example of the comparison of the proton energy spectra between the ^4He gas target and the Ar gas target measurement. The number of events in the background measurement was scaled to the ^4He gas target measurement and this is an example for Telescope 5.

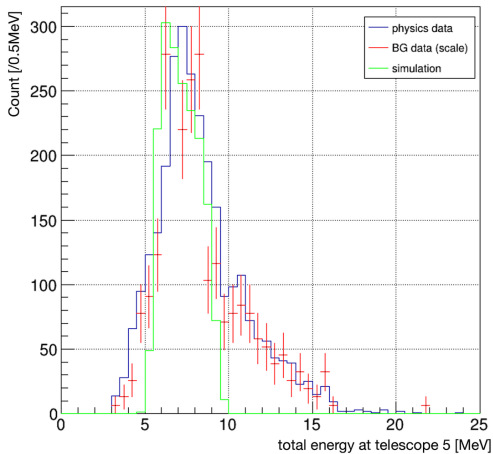


Figure 3: Comparison of the proton energy spectrum between the physics data and the background data. The simulation result of the elastic scattering at the target window is also shown.

The result shows that the structure of energy spectrum appeared in the same position, and with the simulation of the elastic scattering at the target window, we found that the proton events in the low energy region (<10 MeV) mainly originated from elastic scattering at the Mylar window (Figure 3). However, background proton events also appeared in the high energy region, therefore background subtraction was necessary to evaluate the correct yield of the $^{26}\text{Si}(\alpha, p)^{29}\text{P}$ reaction.

The same process was performed for all the telescopes and the reaction cross section was calculated using the yields with the background subtraction. Figure 4 shows the results, together with the cross section of the statistical model, the NON-SMOKER cross section [7]. We assumed a uniform angular distribution and a transition to the ground state. The reaction cross section was considered to be larger in the high energy region, and the ratio of the background events became larger. The events that the reaction occurred near the window had a center-of-mass energy of 7.5 MeV, therefore we considered 6.0 MeV to 7.5 MeV to be a reasonable region for evaluating this data. The energy dependence of the cross section was assumed to be the same as for the NON-SMOKER cross section and fitting was performed using the selected data points. Due to the low statistics, significant yield could not be obtained, therefore an upper limit (99%) was also calculated for conservative evaluation, and the result was 0.134 times the value of the NON-SMOKER cross section (Figure 4).

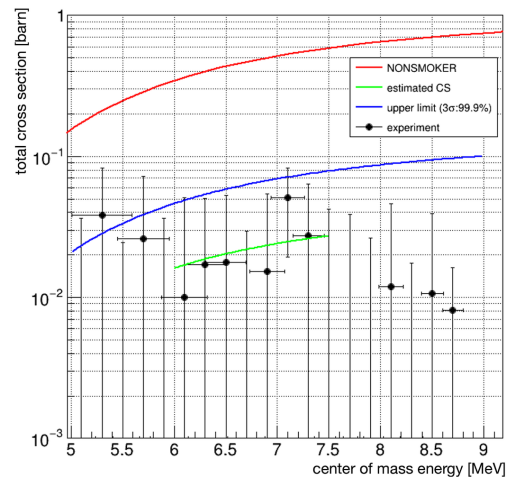


Figure 4: Calculated cross section with NON-SMOKER cross section. The middle line represents the upper limit of the measured cross section, assuming the energy dependence is the same as NON-SMOKER cross section.

4. Summary and outlook

The present study focused on the direct measurement of the $^{26}\text{Si}(\alpha, p)^{29}\text{P}$ reaction. We obtained proton events with up to 7.5 MeV center-of-mass reaction energy, corresponding to a Gamow peak energy of $T = 9$ GK. However, due to the low statistics and the large number of background events, it was difficult to extract significant proton events, so an upper limit on the reaction cross section was calculated. The result was an order of magnitude smaller than the value from the statistical model currently used in models of XRBs, and we point out that this result can constrain the light curve models of XRBs.

For a more accurate evaluation, it is considered necessary to change the window foil causing the background to a hydrogen-free material and perform the measurement again. Also, a comparison with the ongoing analysis of $^{26}\text{Si}(\alpha, \alpha)^{26}\text{Si}$ resonance scattering [8] will provide more complementary results.

References

- [1] J. Grindlay *et al.*, *Astrophys. J.* **205**, L127 (1976)
- [2] R. H. Cyburt *et al.*, *Astrophys. J.* **830**, 55 (2016)
- [3] S. Almaraz-Calderon *et al.*, *Phys. Rev. C* **86**, 065805 (2012)
- [4] Y. Yanagisawa *et al.*, *Nucl. Inst. and Meth. A*, **539**, 74 (2005)
- [5] H. Kumagai *et al.*, *Nucl. Inst. and Meth. A* **470**, 562 (2001)
- [6] K. Artemov *et al.*, *Sov. J. Nucl. Phys.* **52**, 408 (1990)
- [7] T. Rauscher, NON-SMOKER database, <https://nucastro.org/nonsmoker.html>
- [8] M. J. Kim *et al.*, *CNS Annual Report*, (2021)

Investigation of the ${}^6\text{He}$ beam for the ${}^6\text{He}+p$ reaction at CRIB

Q. Zhang^{a,b}, M. Sferrazza^c, H. Yamaguchi^a,
S. Hayakawa^a, K. Okawa^a, S. Cherubini^d, M. La Cognata^d, G. Pizzone^d, T. Chillery^a, S. Hanai^a,
N. Imai^a, S. Masuoka^a, K. Yako^a

^aCenter for Nuclear Study, Graduate School of Science, University of Tokyo

^bSchool of Nuclear Science and Technology, Lanzhou University

^cDepartment of Physics, Université Libre de Bruxelles

^dINFN - Laboratori Nazionali del Sud

We are interested in studying nuclear reaction mechanisms using halo nuclei [1]. We started a research program to study the elastic scattering, transfer reactions, and breakup effect using the lightest halo nucleus, ${}^6\text{He}$. Halo nuclei have a low separation energy on the last nucleon(s): ${}^6\text{He}$ is considered to have a three-body structure $\alpha+n+n$ with a radius of 2.4-2.5 fm [2]. The goal of our experiments is to study the elastic scattering, the two-neutron and one-neutron transfer reactions using ${}^6\text{He}$ beam with light targets. The study of transfer reactions – (p, d) and (p, t) – and breakup effects is anticipated to provide insight into the halo structure and reaction mechanisms [3–5]. For that purpose, we have developed a ${}^6\text{He}$ beam at CRIB.

The machine study (MS) with a ${}^6\text{He}$ beam was performed in Oct. 2022 at the CNS Radio-isotope Beam Separator (CRIB) to improve the beam intensity and purity [6]. The ${}^7\text{Li}^{3+}$ beam at 8.3 MeV with the intensity of 4.4 e μ A was extracted through the AVF cyclotron to bombard the cryogenic gas cell filled with deuteron gas. The ${}^6\text{He}$ particles were produced via the ${}^7\text{Li}(d, {}^3\text{He}){}^6\text{He}$ reaction in inverse kinematics. The ${}^6\text{He}$ beam energy at the F3 Chamber was 7.86 MeV/u, and the intensity reached to 6×10^5 cps with purity of 90% in the optimal experimental conditions. We used two multi-wire drift chamber (MWDC) [7] to track the beam particles event by event as shown in Fig. 1. The tracking efficiency of both MWDCs was better than 96% when the supplied voltages to MWDCa and MWDCb were -900V and -790 V, respectively. The data acquisition (DAQ) trigger made by the MWDCb cathode together with the silicon detectors was compared with the trigger made by the plastic scintillator and silicon detectors [8].

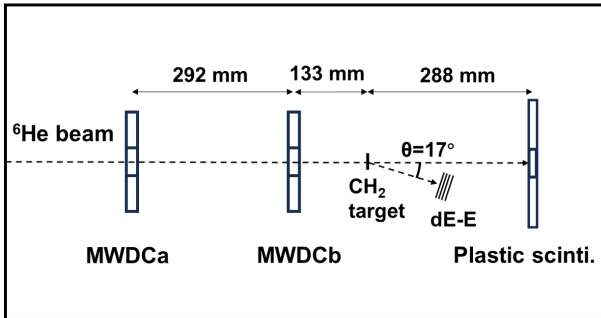


Figure 1: Schematic diagram of the detector setup in the F3 chamber.

In addition to optimizing the beam conditions, we also

performed a short physics run in the MS. The optimal ${}^6\text{He}$ beam hit a polyethylene (CH_2) target with the thickness of 50 μm . A silicon telescope composed of four layers was installed at a detection angle of 17 degrees to detect the scattered particles. The active size of each layer was $50 \times 50 \text{ mm}^2$ with a spacing of 10 mm. The distance between target center and telescope center was 138 mm. A double-side silicon detector (DSSD, 300 μm thick, 16×16 strips) was used as the first layer to measure the hit position (X and Y) and energy loss (ΔE) of the produced particles. The silicon detectors of the remaining three layers were 1500 μm thick and measured the residual energies of the particles. The particles were identified as proton (p), deuteron (d), triton (t), alpha (α), and ${}^6\text{He}$ particles using the ΔE - E method, as shown in Fig. 2.

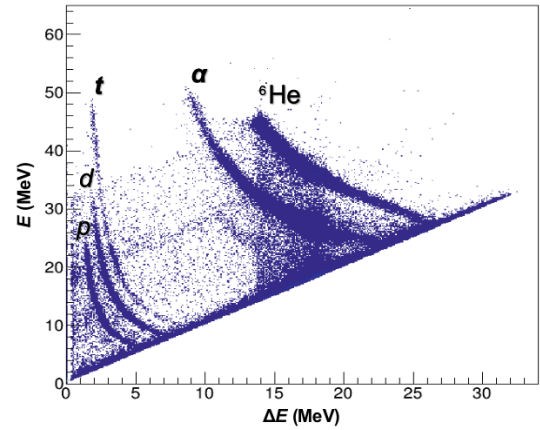


Figure 2: E - ΔE plot of the elastic and transfer reaction.

Fig. 3 shows a correlation between total kinetic energy (E) and the scattering angle in the laboratory frame, as data were collected in only 52 minutes using an intense ${}^6\text{He}$ beam of 1.5×10^5 cps. Kinematical curves of the ${}^6\text{He}(p, p_0/p_1){}^6\text{He}$, ${}^6\text{He}(p, t){}^4\text{He}$, and ${}^3\text{H}(p, p_0){}^3\text{H}$ reactions were depicted in the figure, the p_1 corresponds to the proton from the inelastic scattering to the first excited state of ${}^6\text{He}$ (1.797 MeV, 2^+). It is obvious that the p_0 from the elastic scattering (solid curve in Fig. 3(a)) and t from the transfer reaction (solid curve in Fig. 3(b)) can be clearly separated from other events. Because of the breakup effect of the ${}^6\text{He}+p$ reaction and the subsequent decay of ${}^5\text{He}$ produced by the ${}^6\text{He}(p, d){}^5\text{He}$ reaction, and the $\alpha + d + n$ 3-body exit channel, α and d from the ${}^6\text{He}(p, t){}^4\text{He}$ and

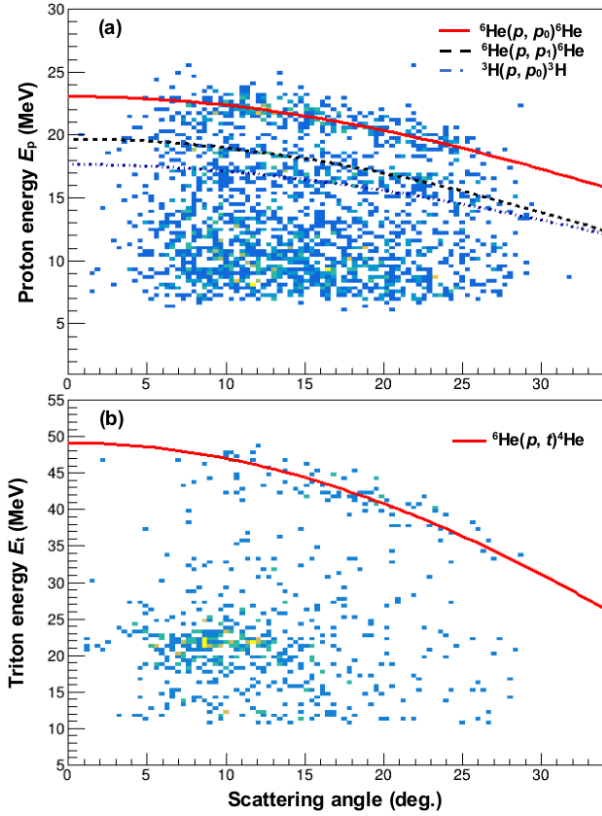


Figure 3: Correlation between kinematic energy (E) and scattering angle in the laboratory frame. Fig. 3(a) and Fig. 3(b) are obtained with selections of produced protons and tritons, respectively. The dashed and dash-dotted kinematic curves of the ${}^6\text{He}(p, p_1){}^6\text{He}$ and ${}^3\text{H}(p, p_0){}^3\text{H}$ reactions are also plotted, respectively. The p_1 corresponds to the first excited state of ${}^6\text{He}$ (1.797 MeV, 2^+).

${}^6\text{He}(p, d){}^5\text{He}$ reactions are not identified yet in the present status. The data analysis of MS will help optimizing the detector setup for the upcoming main experiment in May, 2023.

In summary, the MS was successfully done, where the beam intensity and purity of ${}^6\text{He}-p$ were improved to be 6×10^5 cps and 91% respectively. Additionally, the performance of the 4-layer silicon telescope was examined with the ${}^6\text{He}-p$ reaction for the coming physics experiment. Based on the present analysis, we confirmed the ${}^6\text{He}(p, p_0)\text{He}$ and ${}^6\text{He}(p, t){}^4\text{He}$ reactions were identified with the present setup.

References

- [1] I. Tanihata, H. Savajols, and R. Kanungo, Prog. Part. Nucl. Phys. **68** (2013) 215.
- [2] S. V. Stepantsov *et al.*, Phys. Lett. B **542** (2002) 35.
- [3] P. Descouvemont, C. Daniel, D. Baye, Phys. Rev. C **67** (2003) 044309.
- [4] L. Giot *et al.*, Phys. Rev. C **71** (2005) 064311.
- [5] R. Wolski *et al.*, Phys. Lett. B **467**, 8 (1999) 8.
- [6] H. Yamaguchi *et al.*, RIKEN Accel Prog. Rep. **55** (2022) 94.

- [7] H. Miya *et al.*, Nucl. Instr. and Meth. in Phys. Res. B, **317** (2013) 701.
- [8] S. Hayakawa *et al.*, CNS Annual report (2022, in this volume).

**Experimental Nuclear Physics: PHENIX
Experiment at BNL-RHIC and ALICE
Experiment at CERN-LHC**

Multiplicity dependence of direct photon production in pp collisions at $\sqrt{s} = 13$ TeV

H. Murakami and T. Gunji

Center for Nuclear Study, Graduate School of Science, University of Tokyo

1. Introduction

Thermal direct photon is one of the key signatures of creation of strongly-interacting hot Quark Gluon Plasma (QGP) in ultra-relativistic heavy-ion collisions. In recent years, collective phenomena in high-multiplicity proton-proton and proton-ion collisions [1, 2] have been found and attracted great interest of the heavy-ion community as they exhibit surprising similarities observed in heavy-ion collisions. If these phenomena indicate formation of QGP or creation of a thermalised system, it should give rise to thermal radiation of (virtual) direct photons as well. However, such measurement has not been conducted yet so far. Furthermore, experimentally direct photon measurement is a big challenge, as it is swallowed by a huge background, i.e. photons from hadron decays such as π^0 and η meson. Therefore, the study of direct photon production in small systems is very important, and hence we perform direct photon measurement in minimum-bias (MB) and high-multiplicity (HM) pp collisions, with internal conversion technique [3]. The choice of this technique is based on the necessity to get better signal to background ratio. In this report, the first measurement of direct photon as a function of p_T and charge particle multiplicity $dN_{ch}/d\eta$ are presented.

2. Analysis

The fraction of virtual photon r is defined as the ratio direct over inclusive photon, which is the same as for real as well as virtual photon at massless limit is given by $r = \gamma_{dir}/\gamma_{incl} = \gamma_{dir}^*/\gamma_{incl}^* \Big|_{m=0}$. It is extracted by a fit to the measured dielectron invariant mass spectra as reported in Ref. [4]. The results were preliminary but since then, the π^0 and η meson were finalized. According to this update, systematic uncertainties of r was also re-evaluated and reduced for both MB and HM events. Based on r , the direct photon excess ratio R_γ , which is defined as the ratio between inclusive photon and decay photon spectra $R_\gamma = \gamma_{incl}/\gamma_{decay} = 1/(1-r)$ is calculated. By definition, $R_\gamma > 1$ indicates existence of direct photon signal.

In this analysis, measured R_γ is 1 - 2 % and show significant excess of 3.2σ and 1.9σ of direct photons in the low-momentum range of $1 < p_T < 6$ GeV/c in MB and HM event classes, respectively. This is for the first time to measure direct photon in pp collisions at 13 TeV down to very low $p_T \sim 1$ GeV/c, where theoretical uncertainty of pQCD is large.

The direct photon yield is calculated as $\gamma_{dir} = \gamma_{decay} \times r/(1-r)$. To this purpose, the decay photon spectra called decay photon cocktail, are obtained by employing fast Monte Carlo simulation of light-flavor hadrons decaying into photon. For each of these sources, the input parame-

terizations of the corresponding p_T spectra are identical to those used in the dielectron cocktail simulated for the dielectron spectral analysis.

3. Results

Figure. 1 shows obtained direct photon cross section (left) and invariant yield (right) as a function transverse momentum. Data compared with theoretical calculations: the next-to-leading order (NLO) pQCD calculations by Vogelsang [5], the model of Shen which consists of pQCD (prompt photon) plus thermal photon contribution [6], and prompt photon contribution using Pythia 8 event generator [7]. The pQCD photons are produced via quark-gluon Compton scattering, quark-antiquark annihilation. In addition, higher order processes, like fragmentation or bremsstrahlung, are considered. Note that at LHC energy, fragmentation photon dominates pQCD photon. Shen's thermal contribution considers viscous hydrodynamic evolution which is necessary to discuss creation of QGP in small systems. In Pythia 8 calculation, we selected top 0.1% multiplicity class for the inelastic events.

The result in MB event class is found to be consistent with both pQCD-based calculation and prompt plus thermal contribution, while Pythia 8 underestimates data below 3 GeV/c. The result in high-multiplicity event class is also compared with calculations by Shen and Pythia 8. Since pQCD photon production at high-multiplicity events can not be calculated in the context of the ordinary NLO calculation [8], one from Vogelsang is not shown. For the prompt contribution by Shen, it is assumed that invariant yield is same as MB events. It was found that the HM result is consistent with Shen's calculation, while prompt only contribution and Pythia 8 calculation underestimate data below 3 GeV/c.

Finally, Fig.2 presents the integrated direct photon yield as a function of charged-particle multiplicity at mid-rapidity measured in pp collisions. For this Figure, direct photon yields in MB and HM event classes presented in Fig. 1 are integrated over the $1 < p_T < 3$ GeV/c range. The results show the clear multiplicity dependence, which is not expected a priori. Also, it is found that the result in MB event class is compatible with both prompt photon calculation and hydrodynamical model. Furthermore, the HM result favors photon from prompt plus thermal photons which is hint for QGP in small systems.

4. Discussions

In this report, we presented direct photon measurement in MB and HM pp collisions at $\sqrt{s} = 13$ TeV. With increased statistics and significantly reduced systematic uncertainties of hadronic cocktail compared to previous publication [9],

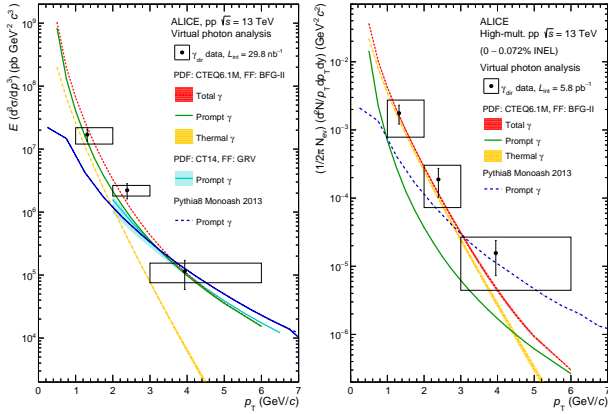


Figure 1: Direct photon spectra vs p_T at MB (left) and HM (right) events compared with theoretical calculations. Statistical and systematic uncertainties of the data are displayed as vertical bars and boxes, respectively. The result in MB pp collisions is compared to theoretical calculations from [5–7], while HM one is compared with [6] and [7].

- [5] L. E. Gordon and W. Vogelsang, Phys. Rev. D (1993) 48.
- [6] C. Shen *et al*, Phys. Rev. C 95 (2017) 1.
- [7] T. Sjostrand *et al*, Comput. Phys. Commun. (2015) 191.
- [8] Private communication with W. Vogelsang.
- [9] ALICE collaboration, Phys. Lett. B 788 (2019) 505.
- [10] ALICE collaboration, Phys. Rev. Lett. 127 (2021) 042302.

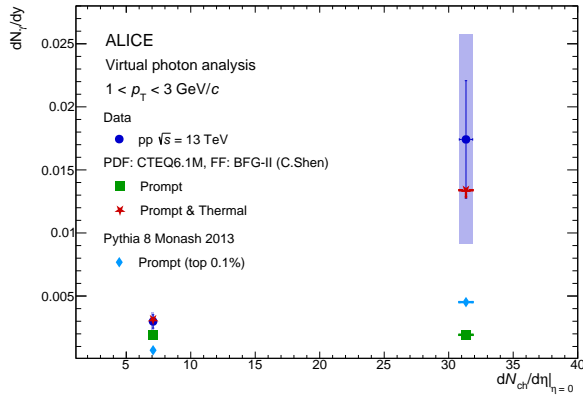


Figure 2: Direct photon yield at mid-rapidity as a function of charged-particle multiplicity $dN_{ch}/d\eta$.

we see for the first time in pp collisions a significant yield of direct photons at low transverse momentum in both event classes. In addition, direct photon yield at mid-rapidity as a function of charged-particle multiplicity $dN_{ch}/d\eta$ is studied. The results show clear multiplicity dependence, and furthermore, it was found that the results favors prompt plus thermal contribution instead of one from prompt only. The statistics which will be collected in the ongoing and future Run 3 and Run 4 periods of LHC operation will allow one to study the direct photon yield with higher statistical precision and in a more differential way.

References

- [1] CMS collaboration, J. High Energy Phys. 09 (2010) 091.
- [2] CMS collaboration, Phys. Lett. B 718 (2013) 795.
- [3] PHENIX collaboration, Phys. Rev. C 81 (2010) 034911.
- [4] H. Murakami and T. Gunji, CNS Annual Report 2022.

Measurement of long-range two-particle correlation and pseudorapidity dependence of v_2 with ALICE

Y. Sekiguchi for the ALICE Collaboration

Center for Nuclear Study, Graduate School of Science, the University of Tokyo

1. Introduction

The measurements of long-range two-particle correlation are a useful tool to study the properties of Quark Gluon Plasma (QGP). Striking correlations over a long range in $\Delta\eta$ on the near side ($\Delta\phi \sim 0$), the so-called ‘‘ridge’’, have been observed in heavy ion collisions at RHIC and the LHC [1, 2]. They are well understood as derived from the collective expansion of the initial collision geometry and its fluctuations in heavy-ion collisions. The ‘‘ridge’’ structure was also observed in small collision systems such as pp and p–Pb collisions [3]. Extending these measurements over a wider range in pseudorapidity and final-state particle multiplicity is important to understand better the origin of these long-range correlations in small-collision systems. We present results on long-range two-particle correlations with pseudorapidity gap $|\Delta\eta| \sim 8$ and the second-order azimuthal anisotropy as a function of pseudorapidity in and p–Pb at $\sqrt{s_{NN}}=5.02$ TeV. These measurements utilize the Forward Multiplicity Detector (FMD) to extract $v_2(\eta)$ over the unprecedented range of about 8 units of pseudorapidity ($-3.1 < \eta < 4.8$). The results are compared with a hydrodynamical calculation.

2. Experimental setup

The main sub-detectors in this analysis are the Time Projection Chamber (TPC) and the Forward Multiplicity Detector (FMD). The TPC is used for charged particle tracking. It covers a pseudorapidity of $|\eta| < 0.8$, where a 2π coverage in azimuthal angle is ensured. The FMD is located at $-3.4 < \eta < -1.7$ (FMD3) and $1.7 < \eta < 5.1$ (FMD1,2) with 2π acceptance in azimuthal angle. The FMD counts the charged-particle multiplicities with a granularity of $\Delta\phi = 1/20\pi$ and $\Delta\eta = 0.05$. For event trigger and centrality determination, the V0 detectors, which are located at $-3.7 < \eta < -1.7$ (V0C) and $2.8 < \eta < 5.1$ (V0A), are used. Minimum-bias events are triggered by using a coincidence signal between V0A and V0C. The positive pseudorapidity is in the Pb-going direction.

3. Analysis

The two-particle correlations between trigger and associated particles are measured as a function of the pseudorapidity difference $\Delta\eta$ and the azimuthal angle difference $\Delta\phi$ for a given event. The associated yield to a trigger particle as a function of $\Delta\eta$ and $\Delta\phi$ between two charged particles is defined as

$$\frac{1}{N_{\text{trig}}} \frac{d^2 N_{\text{asso}}}{d\Delta\eta d\Delta\phi} = \frac{S(\Delta\eta, \Delta\phi)}{B(\Delta\eta, \Delta\phi)}, \quad (1)$$

where N_{trig} is the total number of triggered particles in the

event class, the signal distribution $S(\Delta\eta, \Delta\phi) = \frac{1}{N_{\text{trig}}} \frac{d^2 N_{\text{same}}}{d\Delta\eta d\Delta\phi}$ is the associated yield per trigger particle in the same event, and the background function $B(\Delta\eta, \Delta\phi) = \alpha \frac{d^2 N_{\text{mixed}}}{d\Delta\eta d\Delta\phi}$ is the pair yield between trigger in one event and associated particles from other events with the same multiplicity and primary-vertex position along the beam direction. The α factor is chosen so that $B(\Delta\eta, \Delta\phi)$ is unity at the maximum bin. By dividing $S(\Delta\eta, \Delta\phi)$ by $B(\Delta\eta, \Delta\phi)$, pair acceptance and pair efficiency are corrected. Figure 1 shows the associated yield per unidentified hadron trigger particles for TPC-FMD1,2 (left), TPC-FMD3 (center), and FMD1,2–FMD3 correlations (right) in the 0–5% (top) and 60–100% (bottom) p–Pb collisions. For all three combinations, a long-range correlation on the near side ($-\pi/2 < \Delta\phi < \pi/2$), the so-called ‘‘ridge’’, is observed in the 0–5% event class, while no significant ‘‘ridge’’ is observed in 60–100%.

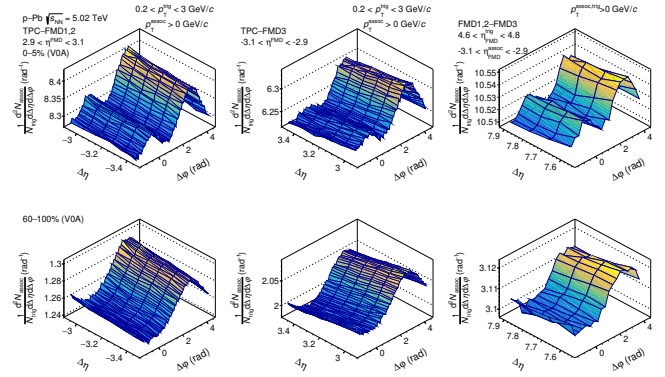


Figure 1: Correlation functions between TPC-FMD1,2 (left), TPC-FMD3 (center), and FMD1,2–FMD3 (right) in 0–5% (top) and 60–100% (bottom) p–Pb collisions.

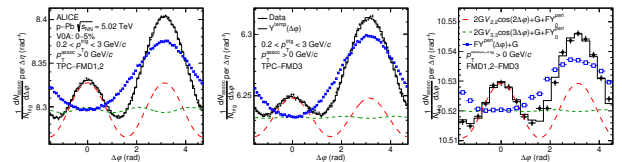


Figure 2: Projection of the correlation function of TPC-FMD1,2 (left), TPC-FMD3 (central), and FMD1,2–FMD3 (right) correlations in 0–5% p–Pb collisions with the template fit.

The template fitting procedure [4] is employed to estimate and subtract the non-flow contamination due to recoil jets and resonance decay. The correlation function $Y(\Delta\phi)$ is assumed to be a superposition of a non-flow contribution, which is estimated by scaling the correlation function from

peripheral events, and the flow contribution. The template fit function is defined as

$$Y(\Delta\phi) = FY_{\text{peri}}(\Delta\phi) + G\left\{1 + 2 \sum_{n=2}^3 V_{n,n} \cos(n\Delta\phi)\right\} \quad (2)$$

where $Y(\Delta\phi)$ and $Y_{\text{peri}}(\Delta\phi)$ are the correlation functions in central and peripheral events, respectively. $F, G, V_{n,n}$ are free parameters. Assuming that the relative modulation of the two-particle correlation function is solely due to the modulation of the single-particle distribution, the modulation of the two-particle correlation measured in two different pseudorapidity ranges for particles A and B can be factorized as: $V_{2,2}(\eta_A, \eta_B) = v_2(\eta_A)v_2(\eta_B)$. If this factorization holds, for example, the second azimuthal anisotropy at the TPC acceptance is obtained by three relative modulations of TPC-FMD1,2, TPC-FMD3, and FMD1,2-FMD3 as

$$v_2(\eta^{\text{TPC}}) = \sqrt{\frac{V_{2,2}(\eta^{\text{TPC}}, \eta^{\text{FMD1,2}})V_{2,2}(\eta^{\text{TPC}}, \eta^{\text{FMD3}})}{V_{2,2}(\eta^{\text{FMD1,2}}, \eta^{\text{FMD3}})}}. \quad (3)$$

Figure 3 shows the p_T -integrated v_2 as a function of η for

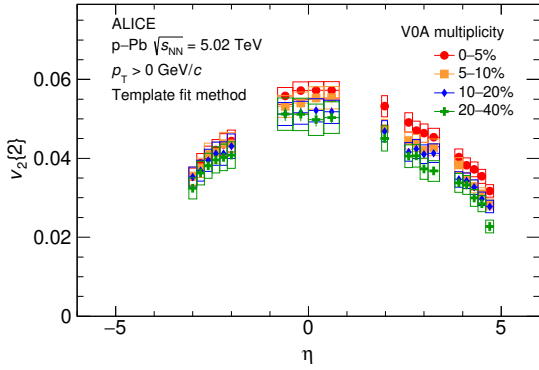


Figure 3: p_T -integrated v_2 as a function of η in various centrality classes.

the 0–5%, 5–10%, 10–20%, and 20–40% centrality class. Non-zero v_2 is observed at $-3.1 < \eta < 4.8$ in up to 0–40% p–Pb collisions. Figure 4 shows v_2 as a function of charged-

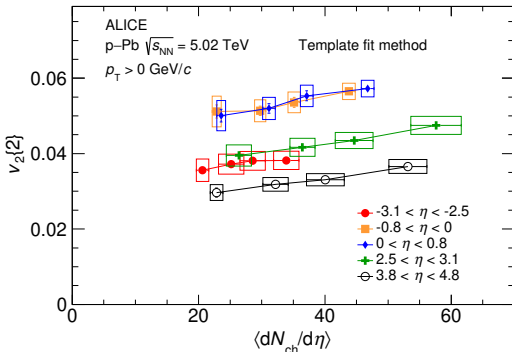


Figure 4: v_2 as a function of charged-particle pseudorapidity density for five different pseudorapidity regions.

particle multiplicity density for five different pseudorapidity regions and for different centrality classes: 0–5%, 5–10%, 10–20%, and 20–40%. It is found that the pseudorapidity

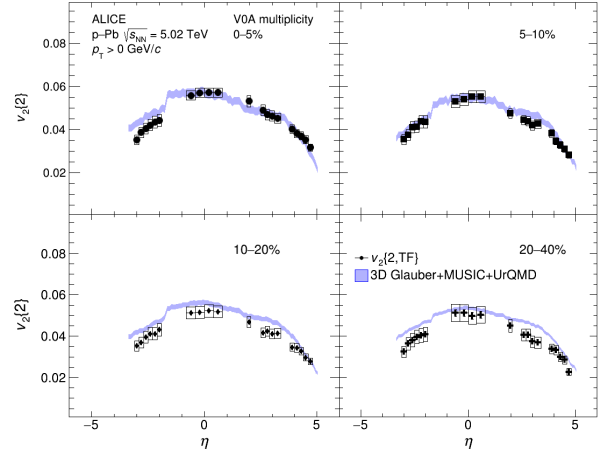


Figure 5: $v_2(\eta)$ compared to the hydro calculation in p–Pb collisions

dependence of v_2 is not just simply driven by the local multiplicity, v_2 independently depends on both η and $dN_{ch}/d\eta$. Figure 5 shows $v_2(\eta)$ compared to the 3+1 hydrodynamical model [5] which employs 3D Glauber initial conditions, viscous hydrodynamics based on MUSIC, and the UrQMD model to simulate the dynamics in the hadronic phase in four different centrality classes. The hydrodynamical model qualitatively describes data for all centrality classes over the entire pseudorapidity region. It suggests that strong final-state interactions are possibly the origin of a significant v_2 over a wide pseudorapidity range even in small collisions.

4. Summary

The long-range two-particle correlations are measured using TPC and FMD in p–Pb collisions. The long-range correlations are observed up to $\Delta\eta \sim 8$. Non-zero v_2 is observed over a wide pseudorapidity range, which is extracted using the three-sub event method. The pseudorapidity dependence as well as its asymmetric shape of v_2 could be well explained by charged-particle multiplicity distributions. The hydrodynamical model describes the data over the entire rapidity region in up to 0–40%. It suggests that the collectivity exists over a wide rapidity region in small collision system.

References

- [1] PHOBOS Collaboration, Phys. Rev. Lett. 104 062301 (2010).
- [2] ALICE Collaboration, Phys. Lett. B 708 249–264 (2012).
- [3] CMS Collaboration, JHEP 09 091 (2010).
- [4] ATLAS Collaboration, Phys. Rev. Lett. 116, 172301 (2016).
- [5] W. Zhao et al. arXiv:2203.06094 (2022)

Production of direct photons via internal conversions in Pb–Pb collisions at $\sqrt{s_{\text{NN}}} = 5.02$ TeV with ALICE at the LHC

D. Sekihata and T. Gunji

Center for Nuclear Study, Graduate School of Science, University of Tokyo

1. Introduction

The goal of performing high-energy heavy-ion collisions is to understand the properties of the quark-gluon plasma (QGP), which is a phase of matter composed of deconfined quarks and gluons under extreme conditions at high temperature and high energy density [1, 2]. Photons and dileptons are one of the tools to investigate the space-time evolution of the high-energy heavy-ion collisions. These electromagnetic probes are produced by various sources during the entire evolution and traverse the medium without strong interaction. Thus, they carry undistorted information at the time of their production [3].

Thermal Photons emitted from partonic and hadronic phases, and prompt photons produced by the initial hard scattering are called direct photons. Thermal photons carry information on the thermodynamics of the system and prompt photons are suitable for testing perturbative QCD (pQCD) calculations. Since experimental photon yields are dominated by background due to photons from hadronic decays, the decay photons are simulated and subtracted. The simulated decay photons, so called “hadronic cocktail”, are based on their measured yields with realistic detector resolution. For the non-measured hadrons, their transverse momentum (p_{T}) spectra are scaled from the measured pions called m_{T} -scaling technique.

The measurement of real direct photons at low p_{T} is challenging due to the large background from π^0 decays which amounts $\sim 85\%$ of total backgrounds, followed by $\eta \sim 12\%$, $\omega \sim 2\%$ and $\eta' \sim 1\%$. An alternative approach to measure the direct photons is to measure direct virtual photons via dielectron channels [4]. One of the advantages of dielectrons compared to real photons is that the dominant background of π^0 decays is significantly reduced by measuring virtual direct photons in the dielectron invariant mass (m_{ee}) region above the π^0 mass of $135 \text{ MeV}/c^2$. The fraction of direct virtual photons over inclusive virtual photons in the kinematic range of quasi-real photons ($p_{\text{T},ee} \gg m_{ee}$) is expected to be equivalent to that of real photons in the mass-less limit $m_{ee} \rightarrow 0$ [5]. Therefore, the measurement of direct virtual photons decaying into dielectrons is independent and complementary to that of direct real photons.

2. Analysis

In November and December of 2018, ALICE took data in Pb–Pb collisions at $\sqrt{s_{\text{NN}}} = 5.02$ TeV with enhanced triggers for central semi-central collisions. The number of events for physics analyses is 65 M in the 0–10% and 55 M in the 30–50% centrality classes respectively. In this analysis, charged particles with $p_{\text{T}} > 0.2 \text{ GeV}/c$ and pseudo-rapidity $|\eta| < 0.8$ are selected. The tracking detectors at the central barrel of ALICE are Inner Tracking System (ITS)

consisting of 6 silicon layers and Time Projection Chamber (TPC). For the electron identification, the specific ionizing energy loss in unit length dE/dx measured in ITS, TPC and the time of flight with the TOF detector are used.

In the pair analysis, there are huge combinatorial backgrounds in unlike-sign pairs (ULS: e^+e^-). The combinatorial background is estimated by the like-sign technique (LS: e^+e^+ or e^-e^-). Signal S is defined as

$$S = N_{+-} - 2R\sqrt{N_{++}N_{--}},$$

where R is a correction factor for different detection efficiencies between electrons and positrons obtained from the event mixing technique by

$$R = \frac{N_{+-}^{\text{mix}}}{2\sqrt{N_{++}^{\text{mix}}N_{--}^{\text{mix}}}}$$

The reconstruction efficiency for dielectron pairs is evaluated in the Monte-Carlo simulation together with detector response.

3. Results and discussions

The efficiency-corrected dielectron invariant mass (m_{ee}) spectrum is shown in Figure 1.

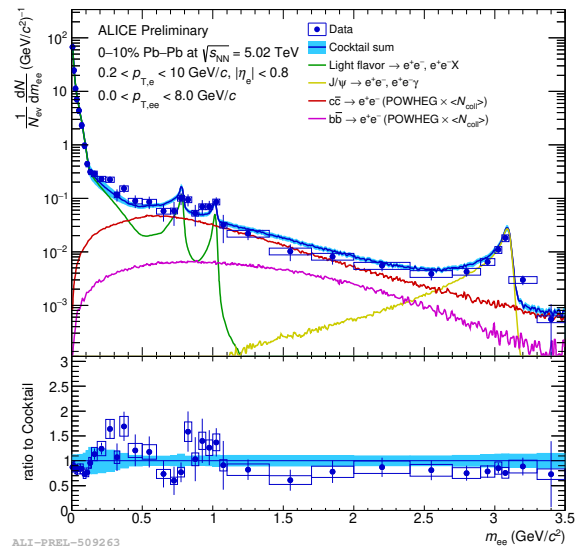


Figure 1: The m_{ee} spectrum in 0–10% central Pb–Pb collisions at $\sqrt{s_{\text{NN}}} = 5.02$ TeV. The vertical bar shows statistical error, while the box shows the systematic error.

Then, the direct virtual photon signal is extracted from the m_{ee} spectrum with the template fit consisting of 3 components. The fitting function is defined as

$$\frac{dN}{dm_{ee}} = rf_{\text{dir}} + (1-r)f_{\text{LF}} + f_{\text{HF}},$$

where f_{LF} is the light-flavor cocktail, f_{HF} is the heavy-flavor cocktail and f_{dir} is the direct photon template given by Kroll-Wada formula [5] which describes the relation between real photon production and dielectron production. The r is the only free parameter and is interpreted as direct photon fraction ($\gamma^{direct}/\gamma^{inc}$). In order to avoid the $\pi^0 \rightarrow e^+e^-\gamma$ (Dalitz) decays, the fitting is performed in the mass range of $0.12 < m_{ee} < 0.34 \text{ GeV}/c^2$. Both f_{dir} and f_{LF} are separately normalized to the data at $m_{ee} < 30 \text{ MeV}/c^2$, because a process dependent factor of the π^0 Dalitz decay is close to unity in this mass region. Thus, the functional forms of f_{dir} and f_{LF} are identical. f_{HF} is in absolute yield. An example of the template fit is shown by Figure 2.

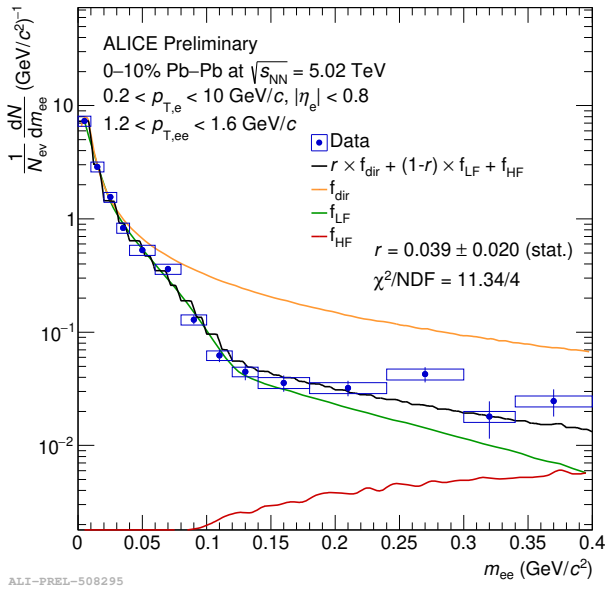


Figure 2: The template fit for direct photon extraction in 0–10% central Pb–Pb collisions at $\sqrt{s_{NN}} = 5.02 \text{ TeV}$ for $1.2 < p_T < 1.6 \text{ GeV}/c$.

Finally, the direct photon yields are constructed by $\gamma^{dir} = r\gamma^{inc}$. The inclusive photon γ^{inc} is measured with photon conversion method at the same energy in the same centrality class. Figure 3 shows the p_T spectrum of the direct photon in 0–10% central Pb–Pb collisions at $\sqrt{s_{NN}} = 5.02 \text{ TeV}$ compared with theoretical models. The dominant systematic uncertainty is due to the fit range variation and the light-flavor cocktail. The new ALICE data points are slightly higher than the pQCD calculation (i.e. photons from hard scatterings at the initial stage). On the other hand, the state-of-the-art model [6] including photons from pre-equilibrium, thermal radiations and hard photons tends to overpredict the direct photon yields at low p_T .

4. Summary

The measurement of dielectron production is performed in 0–10% central Pb–Pb collisions at $\sqrt{s_{NN}} = 5.02 \text{ TeV}$ recorded in 2018. The virtual photon signal is extracted from the mass range of $0.12 < m_{ee} < 0.34 \text{ GeV}/c^2$. The direct photon yields are higher than the pQCD calculation, which can be interpreted as thermal contributions. On the other hand, the state-of-the-art model including photons

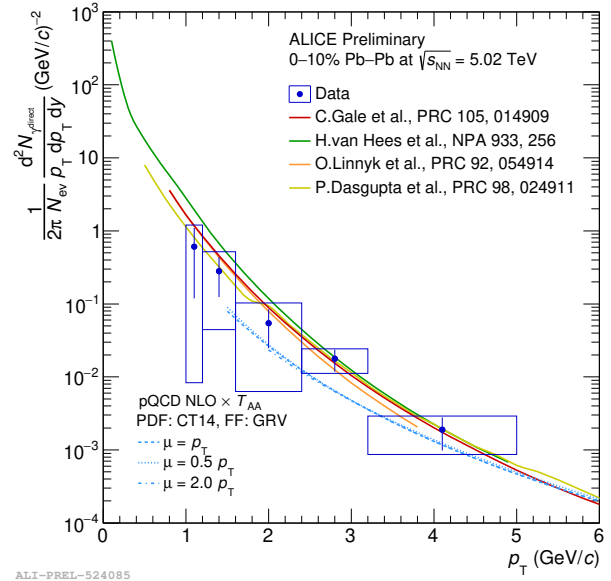


Figure 3: The direct photon spectrum in 0–10% central Pb–Pb collisions at $\sqrt{s_{NN}} = 5.02 \text{ TeV}$ compared with theoretical models.

from pre-equilibrium, thermal radiations and hard photons tends to overpredict the direct photon yields at low p_T .

References

- [1] A. Bazavov et al., Phys. Rev. D 85, 054503 (2012)
- [2] S. Borsányi et al., Phys. Lett. B 730 99-104 (2014)
- [3] J. E. Alam et al., Phys. Rep. 273, 243 (1996)
- [4] A. Adare et al. (PHENIX Collaboration), Phys. Rev. C 81, 034911 (2010)
- [5] Norman M. Kroll and Walter Wada, Phys. Rev. 98, 1355 (1955)
- [6] C.Gale et al., Phys. Rev. C 105, 014909 (2022)

Space-charge distortion correction for the ALICE-TPC using machine learning methods

H. Baba, D. Sekihata and T. Gunji

Center for Nuclear Study, Graduate School of Science, University of Tokyo

1. Introduction

A Large Ion Collider Experiment (ALICE) [1] is an experiment at the Large Hadron Collider (LHC) dedicated to the study of high-energy heavy-ion physics. It aims to uncover the physical properties of strongly interacting matter known as the quark-gluon plasma (QGP) at the highest energy density that could be reached with currently existing accelerators. All matter in our universe is thought to have been in the QGP state at $10^{-6} \sim 10^{-5}$ seconds after the Big Bang.

The Time Projection Chamber (TPC) in ALICE [2] is a gaseous tracking detector designed to detect charged particles with mid-rapidity. There, the trajectories of charged particles are reconstructed and particle identification is carried out. The momentum of charged particles is measured by the curvature of the trajectories in the solenoid magnet at 0.5 T, and particle identification is performed by combining this information with each particle's energy loss in the gas. A 400 V/cm electric field with very high homogeneity is achieved inside the drift volume of TPC by the fine-segmented field cage on the inner and outer wall and a high voltage of -100 kV applied to the central electrode.

The readout chamber at the end cap ($z = \pm 250$ cm) is divided into 18 sectors in azimuthal angle ϕ . Installed in each sector are the inner and outer readout chambers, respectively called IROC and OROC. The active areas for the readout chambers are between 85 and 132 cm for the IROC, and 135 and 247 cm for the OROC in radial direction. Multi-Wire Proportional Chambers (MWPC) with gating grids were used as the signal amplification technology during LHC Runs 1 (2009-2013) and 2 (2015-2018).

In Runs 3 (started in 2022) and 4 (planned in 2030), LHC experiments will take data in Pb-Pb collisions at a maximum of $\sqrt{s_{NN}} = 5.5$ TeV and a collision rate of 50 kHz. In order to accumulate the unprecedented amount of statistics, upgrade of the TPC [3] has been carried out during the LHC Long Shutdown 2 (LS2).

One significant issue in the TPC that needs to be overcome is the space-charge effect. Positive ions produced in the electron multiplication process at the readout chambers are known to flow back into the TPC field cage, becoming a major source of distortion to the homogeneity of the electric field (space-charge effect). During Runs 1 and 2 the gating grid prevented these positive ions from entering the TPC field cage, but this architecture could only handle collision rates of up to 3 kHz, which is significantly below the expected 50 kHz collision rate during the LHC Run 3. As part of the TPC upgrade, the MWPC and gating grid in the readout chambers were removed and were replaced with stacks of four Gas Electron Multiplier (GEM) foils in order to address this problem.

The four GEM foils are relatively effective on their own in keeping the space-charge effect to a tolerable level, but a mechanism to correct the distortions created by the space-charge is still necessary. As the gain of the GEMs will be operated at ~ 2000 and the proportion of backflowing positive ions (Ion Backflow, IBF) is designed to be 1%, 20 ions per one single primary electron are expected to go back to the drift volume. With the positive ion drift time of 160 ms and the collision rate of 50 kHz, space-charge from 8,000 collision events are expected to pile up inside the TPC field cage, resulting in a distortion of $\mathcal{O}(10$ cm) (see figures 1 and 2). The strategies used to correct this distortion are discussed in the following sections.

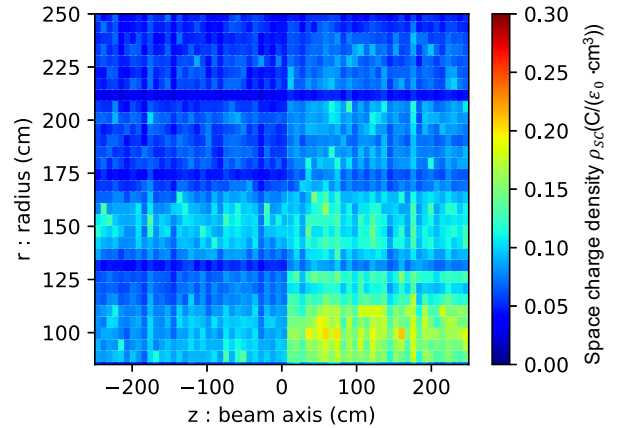


Figure 1: The simulated space-charge density ρ_{sc} at 50 kHz of Pb-Pb collisions in r-z plane. The striped pattern in z originating from the fluctuation of the charged-particle multiplicity corresponds to timing structure of collisions.

2. Calibration strategy

The space-charge distortion calibration will be performed in two steps: online synchronous calibration and offline asynchronous calibration.

The online synchronous calibration will be performed with the goal of reducing the distortion to an amount that would allow for the cluster to track association ($\mathcal{O}(\text{mm})$). To accomplish this the TPC clusters are corrected by a 3D correction map obtained by tracklets from the Inner Tracking System (ITS), Transition Radiation Detector (TRD) and Time-Of-Flight detector (TOF) as a reference for the true track position. The map is updated to the current average charged particles density in the time interval of $\mathcal{O}(\text{min})$ scaled by the digital currents from the readout chambers integrated over the drifting time of ions.

The offline asynchronous calibration will be performed with the goal of reducing the space-charge distortion to the

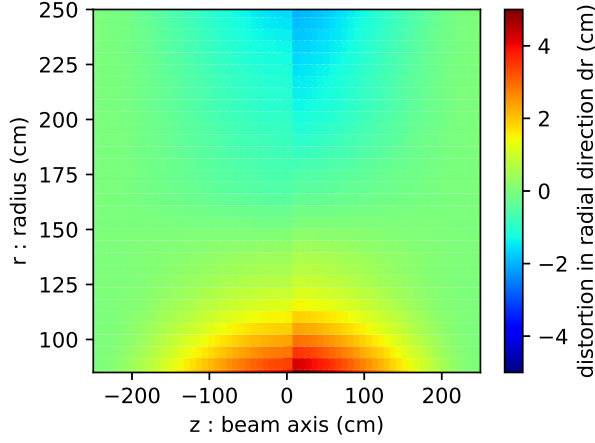


Figure 2: The expected electron track distortion in radial direction dr at 50 kHz of Pb-Pb collisions in r-z plane obtained by solving the Poisson and Langevin equations. It can be seen that the electrons are diverted towards larger radii at inner points and vice versa. The discontinuity at $z = 0$ arises from the muon chamber absorbers installed in the negative z direction.

intrinsic resolution of the TPC ($\mathcal{O}(200 \mu\text{m})$). The short-time distortion fluctuations must be addressed in order to accomplish this level of precision. This would require that the distortion correction be applied every ~ 5 ms, which makes it impossible to collect the amount of statistics necessary for generating corrections with enough precision using traditional methods such as the ITS-TRD-TOF extrapolation method. Therefore, an alternative approach which would allow a relatively fast, efficient distortion prediction is desired.

3. Machine learning approach

As one possibly effective solution to the tasks discussed above, the authors have been studying ways to implement a machine learning approach. The machine learning scheme currently under discussion is as follows: First, input data from the TPC is integrated over ~ 1 ms and stored as the Integrated Digital Current (IDC) in the Conditions and Calibration Database (CCDB). Then the IDCs are integrated over r and ϕ (1D IDC), and the 1D IDC, together with its Fourier coefficients with respect to time are fed to the machine learning as input data to predict the amount of distortion at each TPC space point (1D \rightarrow 3D correction).

So far, three machine learning models, namely the boosted decision tree (XGBoost [4]), Random Forest [5] and dense neural network, have been implemented. The distortion fluctuations for 400 maps were predicted, and the mean / standard deviation of the difference between the model predictions and the expected distortion fluctuation (calculated using Monte-Carlo simulation) were observed (see, for example, figure 3). Several parameters in each of the models were scanned, and a comparison of the overall predictive performance was made. All three models proved to be efficient enough in terms of calculation speed, and some models (one example being the XGBoost model in figure 3) succeeded in lowering the residual space-point dis-

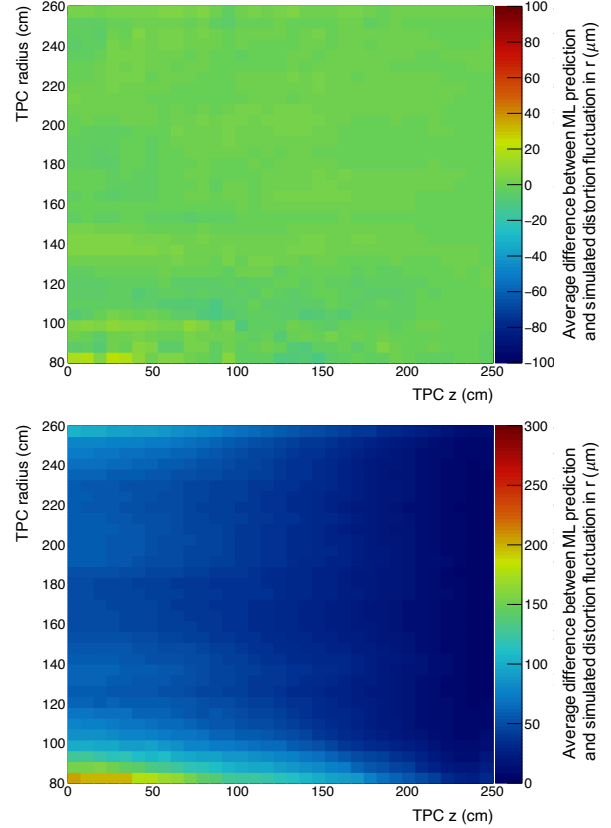


Figure 3: Difference between the distortion fluctuation in the radial direction dr (at $\phi = 0$) predicted by the XGBoost and by Monte-Carlo simulation at 50 kHz Pb-Pb collisions. The XGBoost model was trained with 200,000 maps and 10 points per map. Mean and standard deviation over 400 maps.

tortion below the TPC intrinsic spatial resolution of $200 \mu\text{m}$ at a very wide range inside the TPC volume.

4. Summary and outlook

Machine learning techniques seems to be a promising solution to the ALICE-TPC space-charge distortion calibration. Further studies on model parameters, calculation resource management, additional corrections, etc., will be carried out to achieve the optimal performance.

References

- [1] B. Abelev et al. (The ALICE Collaboration), Int. J. Mod. Phys. A 29 (2014) 1430044
- [2] The ALICE Collaboration, CERN-LHCC-2000-001
- [3] The ALICE Collaboration, CERN-LHCC-2013-020
- [4] Tianqi Chen and Carlos Guestrin. XGBoost: A Scalable Tree Boosting System. 3 2016.
- [5] Leo Breiman. Random Forests. Machine Learning, 45(1): 5-32, 2001.

Accelerator and Instrumentation

Development and commissioning of a mosaic type array formed by Si photodiodes

J. T. Li, N. Imai, R. Kojima, R. Yokoyama, T. Chillery, S. Michimasa, S. Hanai, T. Saito and M. Shiraishi^a

Center for Nuclear Study, Graduate School of Science, University of Tokyo
^aRikkyo University

Heavy-ion fusion-evaporation reactions have been exploited in expanding the chart of nuclides and exploring high excited states in heavy nuclear region [1]. To identify Evaporation Residues (ERs) produced in fusion reactions, the measurement of characteristic α -decay energies has been proven to be effective [2]. Various types of Si detectors are often applied in the measurement owing to good energy resolutions and fast response time. However, there are some long-standing limitations such as the high cost and radiation damage. If the position sensitivity is required experimentally, (Double-sided) Silicon Strip Detector (SSD or DSSD) are used in general while the costs are rather high compared to other detectors like solid scintillators. In addition, the deterioration of the detector performance due to radiation damage has been reported [3] and limits the application of Si detectors in certain nuclear physics experiments such as the synthesis of Very Heavy and Super Heavy Nuclei (VHN, SHN) in which high-intensity beams are necessary to increase the statistics.

To achieve a low-cost (easily replaceable) charged-particle detection with the position sensitivity, we have developed a mosaic-type detection unit by aligning multiple Si photodiodes (Hamamatsu S13955-01) side by side on a Printed Circuit Board (PCB) [4], as shown in Fig. 1.

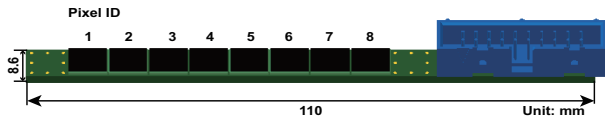


Figure 1: A single row of PCB with 8 pixels mounted on top.

More characteristics of the photodiode have been further investigated. In the previous tests where Mesytec STM16 was used as the shaping amplifier, the resolution of a single photodiode was larger than 100 keV in σ for 5.5-MeV α particles. It was then found that the deteriorated resolution was caused by the short shaping time of STM16 (maximum 2 τ s). Resolutions of the photodiode were measured with different shaping times of the amplifier, as shown in Fig. 2. Since the rising time of the preamplifier output is rather slow ($\sim 8 \tau$ s), good resolutions were achieved with longer shaping time (6, 10 τ s).

The intrinsic position uncertainty of a single photodiode was investigated by placing a collimator between the photodiode and α source (^{241}Am and ^{244}Cm). Several measurements were performed with five different positions of α source, as shown in Fig. 3(a). The inset (7.05 mm is the size of photosensitive area) denotes the geometry for each

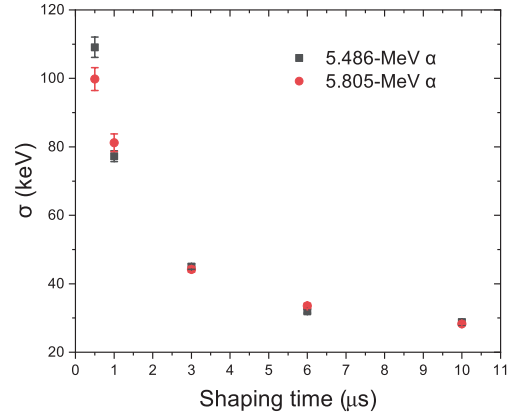


Figure 2: Energy resolutions of the photodiode with different shaping times.

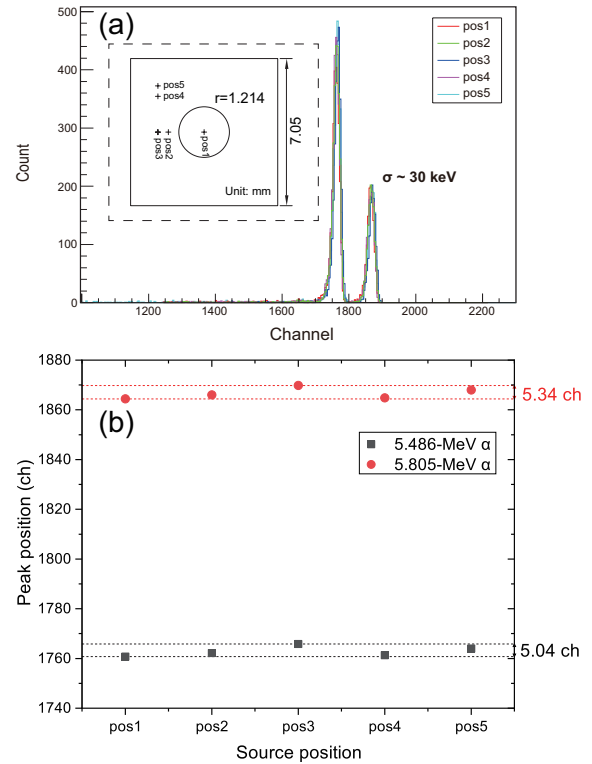


Figure 3: (a) α -energy spectra measured at different source positions; (b) Quantitative evaluation of the intrinsic position uncertainty.

source position, the effective area of the photodiode, which is determined by the size of the collimator and the distance between the photodiode and α source, is 1.214 mm in radius. It can be seen in Fig. 3(b) that for both α particles, maximum shifts of peak centres are about 5 ch correspond-

ing to ~ 15 keV, which is acceptable since 15 keV is less than the intrinsic resolution of 30 keV as shown in Fig. 3(a).

Cross-talk is an important characteristics that affects the performance of an array and was studied using one row of PCB with 8 photodiodes mounted as shown in Fig. 1, the α source (^{241}Am and ^{244}Cm) was placed right in front of the photodiodes. The ratio of cross-talk events was estimated by measuring α spectra for all pixels (ID=1-7) while the trigger was only generated by the central pixel (ID=4). It was found that the ratio between maximum cross-talk events among neighboring pixels and events in the central pixel was affected by the threshold of the trigger output as shown in Fig. 4(a), higher threshold hinders the cross-talk events sufficiently. Figure 4(b) presents the 2-dimensional spectrum for 7 pixels with the trigger threshold of 141 mV, roughly corresponding to an energy threshold of 4.8 MeV. Here the ratio of maximum cross-talk events was 0.08%.

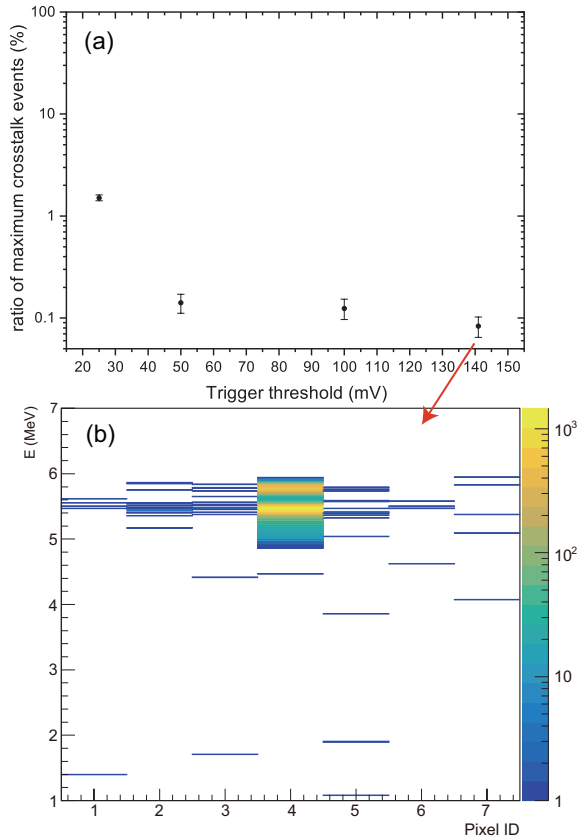


Figure 4: (a) Ratios of maximum cross-talk events with different trigger threshold, the error bars are simply systematic errors; (b) Measured spectrum with the trigger threshold of 141 mV, the y axis is the energy and the x axis is the pixel ID.

By aligning multiple PCBs in Fig. 1, a box-type array called Mosaic was constructed, as shown schematically in Fig. 5. The array was composed of two sides of 8×8 matrix of Si photodiodes. The dead space of the array, originating from the finite size of PCBs and the intrinsic dead space of the photodiode, is of 26% in total.

In July 2022, the setup was commissioned in an experiment performed at HIMAC, during which α decays of partial ERs including Po and Bi isotopes produced in the fusion

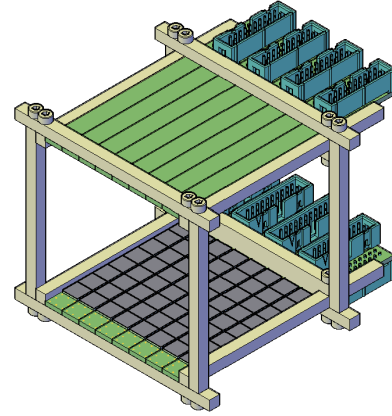


Figure 5: The constructed box-type detector array: Mosaic.

reactions $^{136}\text{Xe} + \text{nat}\text{Zn}$ were measured. Figure 6 shows the angular dependence of the α emission, where the x axis is the distance between the hit position and the target along the beam axis (z direction), the bin size corresponds to the actual size of a photodiode.

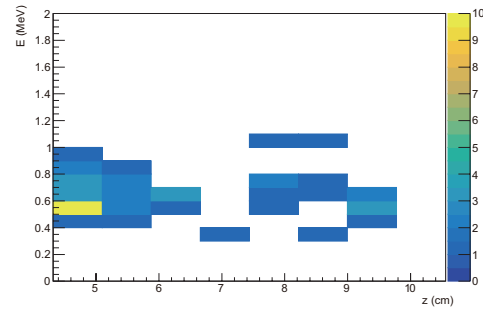


Figure 6: The angular dependence of α particles measured by the Mosaic array.

In conclusion, characteristics of Hamamatsu S13955-01 were studied thoroughly, a box-type Mosaic array was formed using 16 readout PCBs and 128 Si photodiodes in total. During the commissioning experiment, Both prompt and delayed α particles produced in fusion reactions were successfully measured and the array were operated with the beam intensity up to 4×10^8 ppp. The most important feature of the array is the high modularity, which allows one to modify the geometric configuration according to specific experimental requirements. Therefore, the application of Si photodiode Hamamatsu S13955-01 merits further investigation and it shall be a preferred choice to employ such Si photodiodes for budget-limited projects.

References

- [1] W. Nazarewicz, Nature Physics, **14**, 537-541(2018).
- [2] Yu Ts Oganessian and V K Utyonkov, Reports on Progress in Physics, **78**, 036301(2015).
- [3] Gunnar Lindström, Nucl. Instrum. Meth. A, **512**, 30-43(2003).
- [4] J. Li *et. al*, CNS Annual Report 2021, 39(2023).

Recent activities with an active target CAT-M

S. Ota^{a,b}, M. Dozono^c, F. Endo^d, S. Hanai^b, S. Hayakawa^b, N. Imai^b, K. Kawata^b, R. Kojima^b, J. Li^b, S. Michimasa^b, A. Sakaue^b, R. Yokoyama^b, Y. Hijikata^{c,e}, T. Isobe^e, D. Suzuki^e, T. Uesaka^e, S. Fracassetti^f, M. Latif^f, R. Raabe^f, N. Zhang^g, T. Harada^h, J. Zenihiro^c, E. Takadaⁱ,

^aResearch Center for Nuclear Physics, Osaka University

^bCenter for Nuclear Study, Graduate School of Science, University of Tokyo

^cDepartment of Physics, Kyoto University

^dDepartment of Physics, Tohoku University

^eRIKEN Nishina Center

^fDepartment of Physics and Astronomy, KU Leuven

^gInstitute for Modern Physics, Chinese Academy of Science

^hDepartment of Physics, Toho University

ⁱNational Institute for Quantum and Radiological Science and Technology

Incompressibility of macroscopic nucleonic system or so-called nuclear matter is a basic property of the matter relating to the equation of state of nucleonic system. Its isospin dependency becomes very important when the property of matter in neutron stars is discussed but its current precision and/or accuracy is not enough to determine the equation of state. The isospin dependent term K_τ is deduced from the systematic trend of the measured nuclear incompressibility by considering the effect of the surface term and mass-dependent terms. So far the systematic measurements of isoscalar giant monopole resonances (ISGMRs) were performed along the isotopic chains of such as tin and cadmium isotopes using alpha or deuteron inelastic scattering. However, the isobar chain or isologos (a coined word meaning the series of nuclei having the same asymmetric parameter or isospin) chain is very important for the accurate determination of isospin independent and dependent terms of nuclear-matter incompressibility with evaluating the isospin dependent and independent surface term in nuclear incompressibility. Since the mass is constant in the isobar chain and the asymmetric parameter is constant in the isologos chain, then one can evaluate each term in the expansion of the nuclear incompressibility based on the liquid drop model [1] using the several systematic measurements along the isobar and isologos chains. In such nuclide chains, the measurements for not only the stable nuclei but also the unstable nuclei are required. A technique using an gaseous active target system based on a time-projection chamber is one solution. For this purpose (and other general use), an active target system called CAT-M [2] has been developed aiming at the measurement with heavy high-intensity beams and with a large active volume. The operation of the CAT-M with high-intensity beams, for instance, of 500-keV Xe isotopes, was successful but the signal-to-noise ratio of the trigger and the measured hits was poor since the huge amount of background signals was produced by the delta electrons escaped from the beam path into the recoil region. In this report, the recent development for the improvement of the signal-to-noise ratio and the relating measurement is overviewed.

The delta electrons has the various kinetic energy de-

pending on its scattering angle. The maximum kinetic energy is approximated to be $2m_e c^2 \beta^2 \gamma^2$ [3], using the electron mass m_e , light speed c , the ratio of the beam velocity to the light speed β and Lorentz factor γ . For the ISGMR measurement, an incident energy around 100 MeV is suitable from the view points of the simple reaction mechanism and the reaction cross section. Then the maximum magnetic rigidity of the delta electrons is 1.8×10^{-3} Tm. When the magnetic field with a strength of 0.3 T, the curvature of trajectory is 6 mm. A typical way to form a magnetic field for a box-type TPC is to use a large-gap dipole magnet. When whole the active area is in the magnetic field, the cost may be high in general and whole the trajectory is bent and the track fitting becomes complicated (of course it's method is generally established). If the narrow magnetic field can be formed in the field cage and along the beam path, the trajectory outside the magnetic field will be straight and the existing track fitting method can be applied. Then we decided to realize a dipole field formed by a set of permanent magnets. Neodymium magnet with a typical surface strength of 0.6 T is chosen for a easier treatment but this type of magnet is weak against hydrogen embrittlement, which is severe in a deuteron-scattering measurement. To avoid this, the magnets are confined in a gas-tight chassis. In addition, to form the strong field in a gap of 30 mm, return yoke made of iron is attached. Typical magnetic field at the center of the dipole magnet is measured to be 0.3 T. In order to keep the uniform electric field with this dipole permanent magnet system, additional strip electrodes PCB plate surrounds the system and an appropriate HV bias is supplied. An offline test with alpha source was performed. The alpha particles are injected from the side of the magnet. The trajectory of alpha particle from the source was successfully measured with a bending angle.

A compact TPC is designed to measure the beam trajectory with a similar drift velocity to the main TPC and to measure recoil trajectory in order to combine the beam profile measured by an external system, such as timing counter of diamond detector and position detectors. The detail of the compact TPC is described in Ref. [4].

Measurement of deuteron inelastic scattering off ^{136}Xe

was performed for a commissioning of the dipole magnet system and a physics measurement in 2021. The CAT-M was operated with ~ 40 -kPa deuterium gas and a primary beam of ^{136}Xe was impinged into the CAT-M. In order to evaluate the improvement of the signal-to-noise ratio with the dipole magnet, the number of hits is compared. The typical number of hits without the magnet system was 630 out of 4048 readout pads, while the one with the magnet system was 1.4. The signal-to-noise ratio becomes 450 times better.

The other measurements of deuteron inelastic scattering with ^{80}Kr and ^{86}Kr were also performed in 2021 and with ^{84}Kr in 2022. For the physics measurement, two strip-readout parallel plate avalanche counter (SR-PPAC) was installed most upstream of the setup to measure the beam profile. The beam-like particles after the active volume of the CAT-M was measured with Xe-gas scintillator and diamond detector. Data analysis is ongoing.

References

- [1] J. Piekarewicz, and M. Centelles, Phys. Rev. C79, 054311 (2009)
- [2] S. Ota *et al.*, CNS Annual Report 2017 (2019) 41
- [3] R.L. Workman *et al.* (Particle Data Group), Prog. Theor. Exp. Phys. 2022, 083C01 (2022)
- [4] F. Endo *et al.*, CNS Annual Report 2021.

New implantation detectors for decay spectroscopy at fragmentation facilities

R. Yokoyama^a, S. Nishimura^b, V.H. Phong^b, S. Kurosawa^c,

^aCenter for Nuclear Study, the University of Tokyo, 2-1 Hirosawa, Wako, Saitama 351-0198, Japan

^bRIKEN, Nishina Center, 2-1 Hirosawa, Wako, Saitama 351-0198, Japan

^cInstitute for Materials Research, Tohoku University, 2-1-1 Katahira, Aoba-ku, Sendai 980-8577, Japan

The study of β decays far from stability is essential for understanding the evolution of nuclear structure and nucleosynthesis processes. β -decay experiments with such exotic nuclei involve intense cocktail beams from fragmentation facilities. The role of an implantation detector in these experiments is to measure the energy and the positions of both heavy ion implantation and β -ray emission to correlate the identified ion with β -decay events. Historically, Silicon strip detectors have been widely used as implantation detectors for β - γ spectroscopy. As the focus of the β -decay study moves further away from the line of stability towards the neutron drip line, the rising Q_β value and falling neutron separation energy result in the growing significance of β -delayed neutron spectroscopy. A new implantation detector, which uses a segmented YSO (Yttrium Orthosilicate) scintillator array for neutron time-of-flight spectroscopy, was developed [1] to meet the requirement of sub-nanosecond time resolution for the β events that mark the start of the neutron time of flight. The new detector was implemented in β -delayed neutron measurement experiments at RIKEN RI Beam Factory. It was confirmed that the YSO detector correlates β and implant events more efficiently owing to its higher effective atomic number, $Z \approx 35$, and density, $\rho \approx 4.5 \text{ g/cm}^3$. The correlation efficiency of the YSO detector was more than 80% with a 3 mm correlation radius [1]. The success of the YSO detector motivated us to develop a new detector using heavier scintillator material.

We focused on $(\text{Gd}, \text{La})_2\text{Si}_2\text{O}_7:\text{Ce}$ (La-GPS) crystal [2–4] as a candidate material for the new implantation detector. It has a much higher effective atomic number ($Z \approx 51$) and density ($\rho \approx 5.2 \text{ cm}^3$). It is expected to enable us to narrow down the correlation radius to $\approx 1.5 \text{ mm}$ to achieve 80% efficiency, which, in principle, reduces the random coincidences to a quarter of YSO. There are two concerns in using La-GPS crystal as an implantation detector. One is radiation from one of the natural La isotopes, ^{138}La . It could increase the background β events. The other is the longer decay component ($T_{1/2} \approx 310 \text{ ns}$) in the light output of La-GPS [2]. Since an implantation detector has to deal with a wide dynamic energy range, the long tail component causes β -detection dead time after heavy-ion implantation.

To address these concerns, we conducted waveform and self-activity measurements on two La-GPS crystal samples. Sample #1 had a lower amount of Ce doping, while sample #2 had a higher amount. Both samples are 5-mm cubes and connected to Hamamatsu H11934 PMT. The waveform data were taken by CAEN V1730, a 14-bit 500 MS/s digitizer, and fitted with a function with two decay components:

$$f(t) = A(1 + \text{erf}(t/\sigma))(r_1 e^{-t/\tau_1} + (1 - r_1) e^{-t/\tau_2}), \quad (1)$$

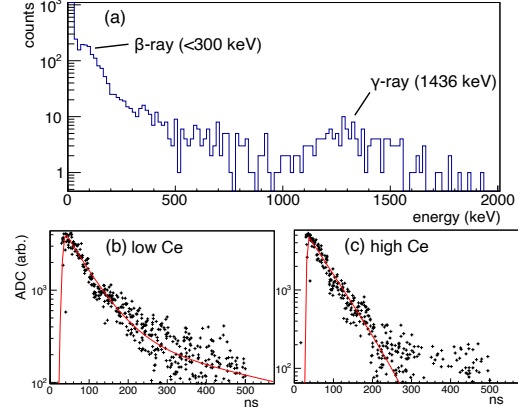


Figure 1: Energy spectrum of La-GPS in room background (a) and example waveforms of sample #1 (b) and #2 (c).

where erf is the error function, σ corresponds to rise time, τ_1 and τ_2 are the lifetimes of two decay components, and r_1 is the ratio of the fast component. τ_1 and τ_2 are fixed to the values in the paper [3], 42ns and 311 ns in $T_{1/2}$, respectively.

Figure 1 (a) is the amplitude (A) spectrum of the background run, roughly calibrated to energy by using ^{137}Cs source data. The γ ray of 1436 keV from ^{138}La decay was observed. The total count of the peak was 118 in an ≈ 90 -minute run. The total radioactivity of the 5-mm cube was estimated to be 5.8 Bq by assuming 0.5% photo peak efficiency from Geant4 simulation and the branching ratio of the γ ray, which is 0.655. The waveforms of samples #1 and #2 in Fig. 1 shows that increasing the Ce doping diminishes the long tail component. The amplitude of the waveform for 1436-keV γ -rays from sample #2 is $\approx 30\%$ less than that of #1 under the same detector conditions. This means the sample #2 meets our minimum light-yield requirement, which is equivalent to that of YSO (≈ 10 photons/keV) or less than a third of the La-GPS sample #1 (≈ 36 photons/keV) [2]. Our current focus is on developing a stable enriched ^{139}La -GPS to minimize the self-activity, thereby reducing the β background.

References

- [1] R. Yokoyama *et al.*, Phys. Rev. C **95** 034313 (2017)
- [2] A. Suzuki *et al.*, Applied Phys. Exp. **5**, 102601 (2012)
- [3] S. Kurosawa *et al.*, NIM A **744**, 30-34 (2014)
- [4] S. Kurosawa *et al.*, IEEE TNS **65**, 2136-2139 (2018)

Cathode-readout self-triggering system on a multi-wire drift chamber

S. Hayakawa^a, K. Okawa^a, Q. Zhang^a, H. Yamaguchi^a, M. Sferrazza^b, S. Cherubini^{c,d},
T. Chillery^a, S. Hanai^a, N. Imai^a, M. La Cognata^c, S. Masuoka^a, R. G. Pizzone^{c,d}, and K. Yako^a

^aCenter for Nuclear Study, Graduate School of Science, University of Tokyo

^bDépartement de Physique, Université Libre de Bruxelles

^cIstituto Nazionale di Fisica Nucleare - Laboratori Nazionali del Sud

^dDepartment of Physics and Astronomy "Ettore Majorana", University of Catania

We have been developing ⁶He beam at Center-for-Nuclear-Study Radioisotope beam separator (CRIB) [1] since 2021. The radioactive beam ⁶He will be used to investigate elastic scattering, transfer reactions and break-up effects using a variety of light targets elucidating, moreover, the properties of the halo structure of the nucleus. As the result of the first ⁶He production test at CRIB in 2021, we successfully obtained ⁶He beams at two different energies of 8.0 and 5.7 MeV/nucleon and with an intensity of the order of 10⁵–10⁶ pps. However, the practical beam intensity was limited to $\sim 2 \times 10^5$ pps due to the low detection efficiency of the Parallel Plate Avalanche Counters (PPACs [2]) for such a light-ion beam. We expected that introducing Low-Pressure Multi-Wire Drift Chamber (LP-MWDC) [3] instead of PPAC would improve the detection efficiency thanks to its higher gas pressure, higher electric field and multi-layer structure, as it has been successfully used even for lower-mass and higher-energy beam such as triton at 200 MeV/nucleon.

MWDCs are usually operated with an external time reference defined by a fast-response detector placed in the beam line such as a plastic scintillator or a diamond detector. A potential problem in low-energy nuclear experiments is, however, that such an extra material may be too thick and degrade the beam energy too much. We thus decided to develop a readout system to pick up the beam-hit timing from the cathode planes of an MWDC to provide the self-triggering function. The conceptual diagram of the readout process is illustrated in Fig. 1. An MWDC has several cathode planes (for the present case, 5 cathode planes sandwiching the X, X', Y and Y' anode wire layers, respectively) and potential wires between every other anode wire which are commonly biased with a single high-voltage (HV) channel. It is considered that a fast detectable pulse is induced to these cathodes by ionization around an anode wire where a beam particle hits, while ions are much slower and defused up to the cathodes surrounding the anode, thus less significant to observe. Installing a high-pass filter (HPF) section with a cutoff frequency of 160 kHz between the cathodes and the readout enables extraction of the induced pulse. We also put a low-pass filter (LPF) section with a cutoff frequency of 333 Hz between the cathodes and the HV, in order to prevent ringing and to suppress high-frequency noise coming from the HV power supply line. We tested the cathode readout system with an ²⁴¹Am alpha source with a gas pressure of 10 kPa and the cathodes biased at 750 V. Figure 2 (a) shows a typical preamplifier (Kaizuworks 3356

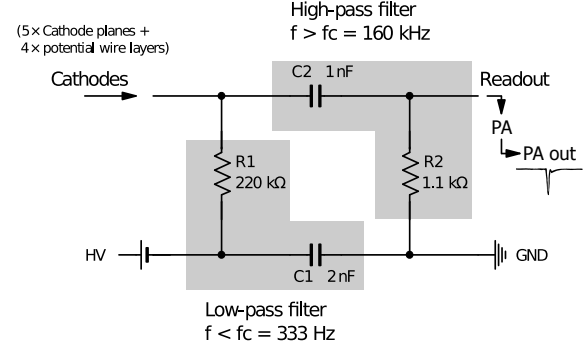


Figure 1: Diagram of the cathode readout of the MWDC.

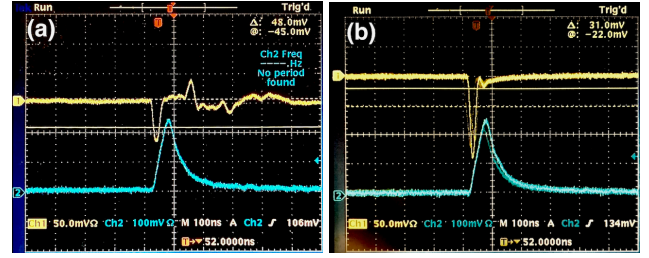


Figure 2: Oscilloscope views of the cathode readout signal (Ch1) without (a) and with (b) the low-pass filter.

5CH AC Pre AMP) output of the cathode signal (Ch1) triggered by one of the anode channels (Ch2) without the LPF, which has a ringing trail caused by reflection in the HV line. One can recognize in Fig. 2 (b) that the ringing is much improved with the LPF, so the pulse width gets also narrower and the height is enhanced, and the baseline is slightly less noisy. This cathode signal is then processed by a timing filter amplifier (ORTEC 474) and a constant fraction discriminator (ORTEC 935) to be used as the data acquisition (DAQ) trigger.

We evaluated the performance of the self-triggering MWDC in the second ⁶He beam production test in October 2022. The primary beam ⁷Li³⁺ was provided at 8.3 MeV/nucleon by the AVF cyclotron, and the secondary beam ⁶He²⁺ was separated by a magnetic rigidity of 1.2272 Tm (8.0 MeV/nucleon). We installed two MWDCs (DCa at upstream side and DCb at downstream side) of XX'-YY' anode configurations with cell sizes of 5 mm and 3 mm for DCa and DCb, respectively. The cathode readout function was provided only at DCb for the test. We also installed a plastic scintillator (PS) at the most downstream position as a time reference for comparison to the cathode readout of the DCb. DCa and DCb were both operated with

Table 1: Position resolution of each anode layer with different trigger conditions.

Trigger	DCa position resolution (mm)				DCb position resolution (mm)			
	X	X'	Y	Y'	X	X'	Y	Y'
Plastic @430 kcps	0.50	0.49	0.49	0.49	0.30	0.30	0.29	0.29
DCb @585 kcps	0.54	0.53	0.50	0.50	0.34	0.35	0.35	0.35

Table 2: Tracking efficiencies of different trigger conditions.

Trigger	DCa eff.	DCb eff.	DCa&b eff.
Plastic @430 kcps	0.926	0.963	0.936
DCb @585 kcps	0.924	0.959	0.900

isobutane gas at 10 kPa, and biased at -890 V and -780 V, respectively for the full intensity beam around 550 kcps.

The observed timing peak of DCb cathode had a full width at half maximum (FWHM) of 3.87 ns with respect to the PS trigger. Since the PS typically has a much faster time resolution, and beam passes through the MWDC structure fast enough (typically within ~ 0.3 ns), this FWHM can be considered as the intrinsic time resolution of the cathode readout. Note that the present MWDC cathode consists of 5 plane layers and 4 potential wire layers, and the pulse timing from each layer may deviates from the actual beam-passing timing depending on the drift time from the beam track to the closest anode wire. Nevertheless, we observed a reasonable time resolution as mentioned above probably because superposing the signals of all the cathode layers may smooth out the random drift-time deviations, forming into a well-shaped single pulse as observed in Fig. 2 (b).

At each anode layer (e.g., DCa X), residual can be defined as the deviation from the best tracked position by all the other layers (e.g., DCa X', DCb X and X'). The position resolution of each anode layer is then defined as the FWHM of the residual distribution. Table 1 lists the position resolution of each anode layer with different trigger conditions. The resolutions with the PS trigger tend to be better probably due to its better time resolution, but we emphasize that those with the DCb trigger are still of practicable level.

The tracking efficiency is defined as the ratio of the number of events within 3σ of the residual distribution to the number of triggers counted either by the PS or the DCb cathode. The tracking efficiencies of DCa, DCb and both DCa and DCb are listed in Table 2. The ones with the DCb trigger achieved a tracking efficiency of 90% for the condition which succeeds both the DCa and DCb tracking. Note that the efficiencies with the PS trigger shown here are corrected by considering the ratio of the DCb counts to the PS counts which is about 90%.

In the test experiment, we also set up a CH_2 target and a position sensitive ΔE - E silicon telescope to evaluate the proton scattering and the two-neutron transfer reaction measurement. The DAQ trigger was a sum of the down scaled

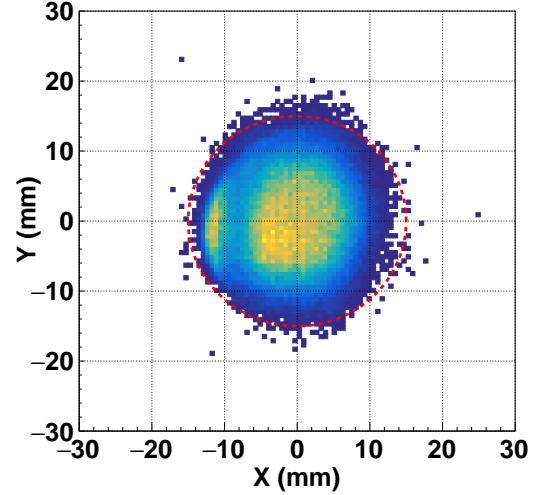


Figure 3: Two dimensional beam profile at the target position extrapolated from the both MWDCs with the coincidence (DCb cathode \otimes Σ Silicon) trigger. The dashed-line circle indicates the target size.

single DCb cathode events (BEAM/N) and the coincidence events (BEAM \otimes Σ Silicon). The secondary beam profile extrapolated on target from the two MWDCs with the coincidence trigger is shown in Fig. 3. Since the events displayed here are only those which passed the target frame, reaching to the telescope through reactions or scatterings, it confirms that the beam tracking by the MWDCs successfully represents the target frame geometry with a reasonable position resolution even with the MWDC self trigger ¹.

In conclusion, the MWDC self triggering system is useful for low-energy light nuclear beams such as ${}^6\text{He}$ even at much higher beam intensity (~ 600 kcps) than the PPAC limit (~ 200 kcps) with reasonable position resolution and tracking efficiency, satisfying the condition required by the approved experiment (NP2021-AVF70) to be performed in 2023. We expect that the performance of the self-triggering MWDC such as position resolution or tracking efficiency can be improved with further optimizations of the readout setup or operation conditions for future experiments.

This test experiment was performed at RI Beam Factory operated by RIKEN Nishina Center and CNS, University of Tokyo. This work was supported by JSPS KAKENHI (grant Nos. 15K17631, 18K13556, and 19K03883) and by the Fonds de la Recherche Scientifique - FNRS under grants numbers J.0174.22.

References

- [1] Y. Yanagisawa *et al.*, NIM A, **539**, 74 (2005).
- [2] H. Kumagai *et al.*, NIM A, **470**, 562 (2001).
- [3] H. Miya *et al.*, NIM B, **317**, 701 (2013).

¹Due to a DAQ problem, we might have lost information of the correspondence between the trigger type and the data, but the coincidence trigger rate was still dominant over the down-scaled beam-single trigger rate.

Improved ${}^6\text{He}$ beam production at CRIB with MWDC and degraders

H. Yamaguchi, M. Sferrazza^a, S. Hayakawa, K. Okawa, Q. Zhang^b, S. Cherubini^c, M. La Cognata^c, R.G. Pizzone^c, T. Chillery, S. Hanai, N. Imai, S. Masuoka, and K. Yako

Center for Nuclear Study, Graduate School of Science, the University of Tokyo

^aDepartment of Physics, Université Libre de Bruxelles

^bLanzhou University

^cINFN - Laboratori Nazionali del Sud

The first production test of ${}^6\text{He}$ beam at CRIB was performed in 2021 [1], in which ${}^6\text{He}$ beams at two different energies (8.0 and 5.7 MeV/u) were successfully produced with an intensity around 10^5 – 10^6 pps. However, the practical beam intensity was limited to $\sim 2 \times 10^5$ pps due to the low detection efficiency of the PPAC for such a light-ion beam. The ${}^6\text{He}$ beam purity was 73% for the 8 MeV/u beam, where the main contaminant was ${}^3\text{H}^{1+}$, having an almost identical charge-to-mass ratio as ${}^6\text{He}^{2+}$.

The second test was carried out in Oct. 2022 as a two-day Machine Study (MS-EXP22-05), to improve the effective intensity and purity of the ${}^6\text{He}$ beam by introducing wire chambers (MWDC [2]) and degraders. The primary beam was ${}^7\text{Li}^{3+}$ accelerated with the AVF cyclotron to an energy of 8.3 MeV/u, and the RI beam was produced with the ${}^7\text{Li}(d, {}^3\text{He}){}^6\text{He}$ reaction in inverse kinematics. The major differences from the first test were the maximum ${}^7\text{Li}$ beam current of $1.5 \mu\text{A}$ ($= 4.4 e\mu\text{A}$) at the entrance of CRIB and the pressure of the production target (around 410 Torr), both lower than the previous values ($3 \mu\text{A}$ and 730 Torr, respectively).

To purify the ${}^6\text{He}$ beam, we installed degraders with two different thicknesses (10- μm -thick aluminized and 20- μm -thick normal Mylar films) at the F1 (momentum dispersive) focal plane. We confirmed a position offset between ${}^6\text{He}$ and ${}^3\text{H}$ was produced at F2 with each degrader, as shown in Figure 1. Using the 20- μm -thick degrader, the beam purity at F3 measured with a plastic scintillator was 91%, much improved from the previous value, 73%.

The MWDC had already been developed and used at CNS for SHARAQ/OEDO experiments [2], and introduced for the first time at CRIB. In the present test, we employed two MWDCs operated at 10 kPa (76 Torr), having an XX-YY anode configuration and cell sizes of 3 mm and 5 mm for the upstream and downstream ones, respectively. Even with a high-rate secondary beam at 6.0×10^5 pps, the MWDCs maintained a timing-detection efficiency $\epsilon > 90\%$ with high voltages of up to 900 V, and no significant reduction of the efficiency was observed. This is in contrast to the previous test, where we had to limit the primary beam current to $0.3 \mu\text{A}$ in order to keep the stable PPAC operation with an acceptable efficiency ($\epsilon = 70\%$). The basic beam parameters are summarized in Table 1 and compared with those of the optimum case in the previous test. The new ${}^6\text{He}$ rate ($\times 2.6$ improvement) is roughly consistent with the previous value, considering the higher ${}^7\text{Li}$ beam current ($\times 5$) and nearly half F0 pressure ($\times 0.56$). How-

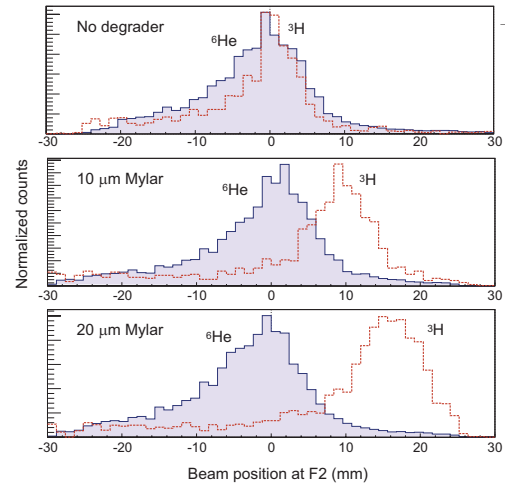


Figure 1: The beam profiles of ${}^6\text{He}$ (solid line) and ${}^3\text{H}$ (dashed line), with different degrader settings. The counts are scaled to show the profiles as similar heights.

Table 1: Summary of the basic beam parameters. ϵ is the efficiency of the beam-monitoring detector.

Test year	${}^7\text{Li}$ (μA)	F0 Pres. (Torr)	ϵ	${}^6\text{He}$ purity	${}^6\text{He}$ rate (kcps)
2021	0.3	730	70%	73%	200
2022	1.5	410	94%	91%	520

ever, the previous rate (200 kcps) was severely limited with the capability of the PPAC, while in the present work we successfully obtained a higher ${}^6\text{He}$ rate (520 kcps) with a better beam purity (91%), even though the F0 pressure was lower. The new condition well satisfies the requirements by the approved experiments [3], to be performed in the near future.

References

- [1] H. Yamaguchi *et al.*, RIKEN Accel Prog. Rep. **55** (2022) 94.
- [2] H. Miya *et al.*, Nucl. Instr. and Meth. in Phys. Res. B, **317** (2013) 701–704.
- [3] M. Sferrazza, H. Yamaguchi *et al.*, proposal for RIBF NP-PAC-21, NP2021-AVF70 (2020, unpublished).

Development of a Radio Frequency Dipole Mass Filter for the Francium Permanent Electric Dipole Moment Search

M. Fukase, H. Nagahama^a, K. Nakamura^a, N. Ozawa¹, M. Sato^{b,c}, T. Nakashita^{b,c}, S. Nagase, D. Uehara², Y. Kotaka^a, K. Kamakura^a, T. Aoki^b, H. Haba^c, A. Takamine^c, H. Ueno^c, and Y. Sakemi^a

Graduate School of Science, University of Tokyo

^a*Center for Nuclear Study, University of Tokyo*

^b*Graduate School of Arts and Sciences, University of Tokyo*

^c*RIKEN (The Institute of Physical and Chemical Research)*

Our research group aims to measure the permanent electric dipole moment (EDM) using the heavy element francium (Fr). EDM is a physical quantity that breaks the time-reversal (T) symmetry. Assuming the CPT theorem, the T symmetry breaking is equivalent to the CP symmetry breaking, so it is said that EDM denotes the CP symmetry breaking. CP symmetry breaking is one of Sakharov's three conditions necessary to explain the matter-dominated universe [1]. Therefore, the search for EDMs is an important means to solve the mystery of the preponderance of matter over antimatter in our universe. In particular, it is known that the effect of the electron EDM is amplified in heavy elements with large atomic numbers and it manifests as the atomic EDMs. It is theoretically suggested that the amplification rate is proportional to the cube of the atomic number [2]. Based on the above, our group aims to measure electron EDM by precision spectroscopy using Fr, which has the largest atomic number among alkali metal atoms that can be easily controlled by laser.

Beam purity is an important factor in such precise measurements of heavy elements using heavy element ion beams. For example, our plan is as follows. Since Fr is rarely available in nature, our plan is to produce it by the nuclear fusion reaction $^{197}\text{Au}(^{18}\text{O}, xn)^{215-x}\text{Fr}$. The produced Fr moves through the gold target by thermal diffusion, is drawn from the gold surface as a Fr ion beam by surface ionization, and is irradiated to the yttrium (Y) foil target by an electrostatic lens system. Also, other alkali metal ions, which are lighter than Fr, are extracted from the gold surface in large quantities as impurities. Since the electrostatic lens system does not have the ability to perform mass separation, these impurities are also irradiated to the Y foil target. The irradiated Y foil target is mechanically transported to the chamber for laser spectroscopy, where it is heated. Fr and impurities irradiated to the Y foil are thermally desorbed as neutral atoms and they are cooled and captured by the laser. However, the presence of impurities causes the loss in reproducibility of Fr desorption from the Y foil and in the efficiency of Fr capture by laser. Thus, we need to increase the purity of the Fr ion beam. Therefore, a radio frequency dipole mass filter (RFDMF) to remove impurities lighter than Fr and a beam diagnostic system to evaluate the performance of the filter were developed.

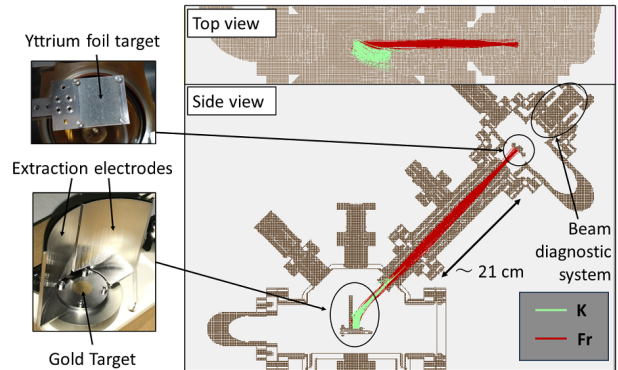


Figure 1: Examples of trajectories of K and Fr ions and an overview of the experimental setup. Trajectory calculation is based on SIMION.

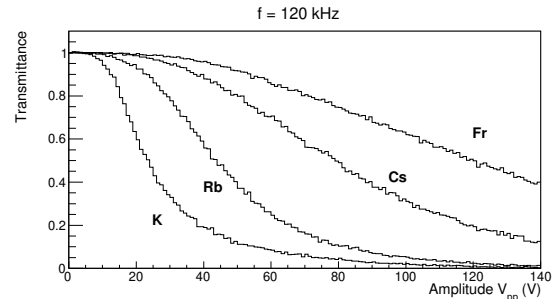


Figure 2: Simulation result. Dependence of the transmittance for each ion on the amplitude of the alternating voltage at the frequency $f = 120$ kHz, due to the operation of the RFDMF.

The RFDMF is a mass filter that removes impurities by shaking the ion beam by adding an oscillating electric field to the electrostatic field created by the electrostatic lens system [3]. Heavy ions such as Fr ions are not easily affected by the oscillating electric field and proceed straight to the Y foil target, while impurity ions, which are lighter than Fr ions, are bent by the oscillating electric field and are removed by colliding with the inner walls of the chamber (Fig. 1). The oscillating electric field is created by applying an alternating voltage $V(t; f, V_{pp}) = V_{pp}/2 \cdot \sin(2\pi ft)$ in the opposite phase to a pair of extraction electrodes associated with a gold target, the beam extraction source. Fig. 2 shows an example of the calculated transmission to the Y foil target for several alkali metal ions using the SIMION [4] sim-

¹Present Address: Department of Physics, Kyoto University

²Present Address: PwC Consulting LLC

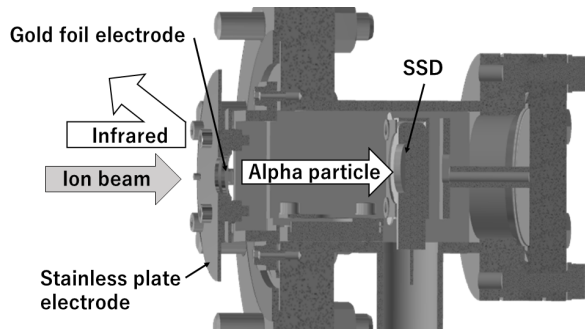


Figure 3: Developed beam diagnostic system. Stray light from the infrared heater is shielded by the gold foil electrode and the stainless plate electrode of Faraday cup, but the alpha particles penetrate the gold foil electrodes

ulation code for ion trajectories. The transmittance was calculated with the beam intensity at the Y foil target as 1 when no alternating voltage was applied. The advantages of this mass filter are that it can be realized by applying an alternating voltage to existing electrodes, making it inexpensive to develop, and that it can function in a beam transport system as short as several tens of centimeters.

The alternating voltage applied to the extraction electrode was generated by amplifying the signal from a function generator using a resonant circuit made with transformers and capacitors.

The beam diagnostic system must be able to simultaneously measure the beam current and the alpha particles from the alpha emitters contained in the beam to measure the beam purity. In addition, a silicon solid state detector (SSD) is used to detect the alpha particles, but it is necessary to prevent stray light from the infrared heater used to heat the gold target from entering the SSD. To meet these requirements, a beam diagnostic system using a gold foil as a Faraday cup electrode was developed (Fig. 3). By placing the SSD on the opposite side of the gold foil from the beam irradiation surface, the alpha particles emitted by the beam particles on the gold foil can penetrate the gold foil and enter the SSD. In addition, stray light from the infrared heater is shielded by Faraday cup electrodes. However, since the Faraday cup has a flat plate structure, the contribution of secondary electron emission due to beam irradiation may be included in the observed beam current. By using this structure, the beam current and the alpha particles from the alpha emitters contained in the beam were measured simultaneously.

In September 2022, an evaluation experiment of the RFD MF was performed with an $^{18}\text{O}^{6+}$ beam accelerated to 6.96 MeV/nucleon using the AVF cyclotron at RIKEN. During the evaluation experiment, the voltage in the electrostatic lens system was fixed and the alternating voltage applied to the extraction electrode was varied every 180 to 190 s, and the change in beam intensity was measured by the beam diagnostic system. The frequency of the alternating voltage was fixed at $f = 120$ kHz and only the amplitude V_{pp} was varied. From the obtained data with the SSD, events in the channels that were thought to correspond to Fr were extracted. Then, the Fr beam intensity was derived

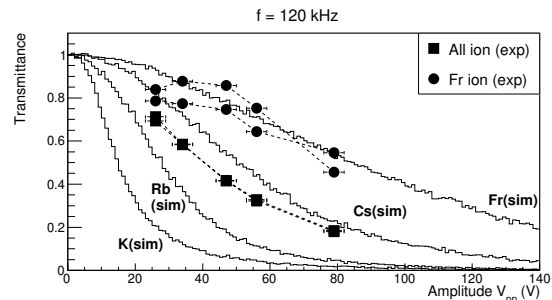


Figure 4: Dependence of the transmittance for each ion on the amplitude of the alternating voltage at the frequency $f = 120$ kHz, due to the operation of the RFD MF. The plot for Fr shows the lowest possible value when errors are taken into account. The dashed line shows time series of data points. The solid line shows results from simulation.

from the time variation of the count rate under the following two simplifications. First, among the Fr isotopes produced in the fusion reaction, the lifetimes of ^{208}Fr and ^{209}Fr , which are short-lived, were set to 79.1 s, and the lifetimes of ^{210}Fr and ^{211}Fr , which are long-lived, were set to 272 s. Second, the abundance ratios of these isotopes in the beam were assumed to be constant at all times. Also, the total beam intensity was obtained from the current measured in the Faraday cup. Transmittance was then obtained by comparing those intensities when the RFD MF was not operating ($V_{pp} = 0$), and when $V_{pp} \neq 0$ (Fig. 4). Fig. 4 shows that the beam purity was improved by at least a factor of 2.9 by the RFD MF at $V_{pp} = 79$ V.

The RFD MF improved the beam purity. This is a milestone in developing RFD MF for short beam transport systems such as our group's. On the other hand, the improvement in beam purity may not be sufficient for EDM measurements, and new methods may need to be developed in the future.

Acknowledgement

This research was supported by Forefront Physics and Mathematics Program to Drive Transformation (FoPM), a World-leading Innovative Graduate Study (WINGS) Program, the University of Tokyo.

References

- [1] A. D. Sakharov, *Sov. Phys. Usp.* **34** (1991) 392.
- [2] D. Budker, D.F. Kimball, and D.P. DeMille. *Atomic Physics: An Exploration Through Problems and Solutions*. Oxford University Press, 2004.
- [3] S. Okamura. A high purity francium beam for studies of fundamental symmetries: development of a mass filter. Master's thesis, Universit'a degli Studi di Ferrara, 2020.
- [4] D. A. Dahl, *Int. J. Mass Spectrom.* **200** (2000) 3.

Optical system for the optical lattice trapping of heavy alkali atoms

N. Ozawa^{†,a}, K. Nakamura^a, S. Nagase^a, T. Nakashita^{b,c}, H. Nagahama^a, and Y. Sakemi^a

^aCenter for Nuclear Study, Graduate School of Science, University of Tokyo

^bGraduate School of Arts and Sciences, University of Tokyo

^cRIKEN (The Institute of Physical and Chemical Research)

[†]Current address: Department of Physics, Kyoto University

The permanent electric dipole moment (EDM) of elementary particles is a source of charge-conjugation and parity (CP) violation if it exists, and although the Standard Model of elementary particle physics (SM) predicts an undetectably small magnitude of it, unknown sources of CP symmetry predicted in BSM models could enhance the effect [1]. It is theoretically predicted that the francium (^{210}Fr) atom enhances the electron EDM by a factor of $\sim 8 \times 10^2$ [2]. Using an optical lattice, the Fr atoms can be confined in the measurement region for ~ 1 s while suppressing interatomic collisions, improving the statistical sensitivity for the measurement. The optical lattice is formed by a standing wave of linearly polarized continuous wave laser beam [3]. The wavelength of the beam must be red-detuned with respect to atomic resonance. For Fr and other alkalis, this can be satisfied by using the wavelength $\lambda = 1064$ nm, which is easily producible by commercial Nd:YAG lasers. The trap potential depth is proportional to the intensity of the light at the atom position, so the standing wave must be focused at the position of the atoms.

We have developed an optical system capable of producing an optical lattice of approximately 0.2 mK depth in the case of Fr. As an initial step, we build a system to directly load stable Rb or Cs atoms from a magneto-optical trap (MOT) into a one-dimensional optical lattice. Fig. 1 shows the setup of the developed system. The laser light is emitted from a Nd:YAG laser (Coherent Mephisto 500NE), and coupled to a single-mode polarization-maintaining fiber (SM/PMF). The beam is divided into three paths, so that light can be used simultaneously for, e.g., other optical trapping experiments, or inspection of alignment quality. The SM/PMF is fed to an ytterbium-doped fiber amplifier (YDFA; Nufern NuAMP), which amplifies the beam power from ~ 0.1 W to over 30 W at maximum. It is typically operated at below 10 W for safety reasons. The amplified light is emitted into air via a fiber-pigtail collimator, and sent through an acousto-optic modulator (AOM) for power stabilization, and a Faraday rotator (FR) for circulation. The beam is then coupled to another SM/PMF using a fused-silica objective lens (Thorlabs, LMH-10X-1064) in order to minimize thermal lensing effect, and sent to the experimental area, where the vacuum chamber is placed. The beam is emitted into air with a fiber collimator (Thorlabs, ZC618APC-C), focused at the center of the vacuum chamber with a pair of achromatic doublet lenses (Thorlabs, AC254-300-C), and finally reflected with a plane mirror (Autex, HYD-10). A vacuum system containing dispensers of Rb and Cs is used to prepare a MOT. In order to check whether the beam axis is properly aligned to the

atoms trapped in the MOT, which could be displaced from the center of the vacuum chamber due to misalignment, a dichroic mirror (Thorlabs, DMLP900) superimposes a probe beam onto the lattice axis. When the probe beam has enough intensity and is properly aligned onto the atoms, it will blast the atoms away from the MOT, which could be directly observed by monitoring the fluorescence. After confirming that the probe beam is aligned, the lattice beam axis is tuned by a pair of mirrors so that it is aligned onto the probe beam axis. Note that this is a rough alignment, and further fine-tuning using spectroscopic methods are necessary to achieve maximal loading.

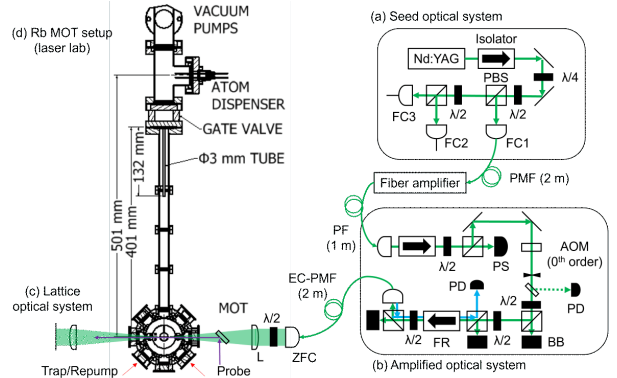


Figure 1: Entire system of the optical lattice setup. The beam is prepared in the systems (a) and (b), and irradiated onto atoms trapped in the chamber at (c). Dispensers of rubidium and cesium are installed in region (d). Abbreviations are PBS: polarization beam splitter, FC: fiber coupler, PS: power sensor, and BB: beam block.

The beam width at the focal point (commonly referred to as the “beam waist”) determines the depth of the potential. For the current setup, it is determined by the focal lengths of the fiber collimator f_{ZFC} and the achromatic doublet lens f_L . Assuming an ideal Gaussian beam, the radius at which the beam intensity drops to $1/e^2$ of the peak is given by

$$w_0 = \frac{(\text{MFD})}{2} \times \frac{f_L}{f_{ZFC}}, \quad (1)$$

where (MFD) is the mode-field diameter of the SM/PMF, which is $6.6 \mu\text{m}$ for our fiber (Thorlabs P3-1064PM-FC) operating at 1064 nm. Since f_L is fixed to 300 mm and f_{ZFC} is adjustable in the range from 6 mm to 18 mm, the beam radius should lie within the range

$$55 \mu\text{m} \leq w_0 \leq 165 \mu\text{m}. \quad (2)$$

Species	$U_{\text{IDOL}}/k_{\text{B}}$ (mK)	$2\pi/\Gamma_{\text{IDOL}}$ (s)
Rb	0.02–0.2	4–30
Cs	0.04–0.4	2–10
Fr	0.02–0.2	4–40

Table 1: Calculated ranges of lattice potential depth U_{IDOL} and photon scattering rate Γ_{IDOL} expected with our choice of optical components. Values of α are calculated using the approximate formula for ground state alkali atoms [4].

The maximum potential depth resulting from this system is given by

$$U_{\text{IDOL}} = \frac{4\alpha P_{\text{in}}}{\pi\epsilon_0 c w_0^2}, \quad (3)$$

where α is the polarizability of the atom, P_{in} is the power of the laser beam, ϵ_0 is the vacuum permittivity, and c is the speed of light. The photon scattering rate Γ_{IDOL} , which limits the trap lifetime, is proportional to U_{IDOL} by a factor independent of P_{in} and w_0 . Assuming a value of $P_{\text{in}} = 2$ W, the ranges of $U_{\text{IDOL}}/k_{\text{B}}$, where k_{B} is the Boltzmann constant, and $2\pi/\Gamma_{\text{IDOL}}$ are given in Tab. 1. The depth covers the range of the Doppler temperature of the species on the order of 0.1 mK, while the timescale of photon scattering is at least on the order of seconds, which is a reasonable level for our purpose. In particular, the beam radius of $w_0 \sim 60 \mu\text{m}$ is preferred so that the potential depth is maximized and the atom loading efficiency as well.

In order to check the performance of the system, the width of the lattice beam is evaluated. The beam width immediately before the reflection mirror is measured using the so-called double knife edge method. Similar to the conventional knife edge method, the beam is partially blocked with a mechanical slit (Thorlabs VA100CP/M), and the transmitted power is measured for various slit widths. Assuming again that the beam has an ideal Gaussian spatial profile, the transmitted power P_T as a function of slit width a can be described by

$$P_T = P_0 \text{erf}\left(\frac{a}{\sqrt{2}w_z}\right), \quad (4)$$

where P_0 is the total power before the slit, and w_z is the beam radius at the slit. A fit of P_T to the data with w_z as a fit parameter yields the beam radius.

Figure 2 shows the result of such a measurement, where the laser beam from the seed optical system is used in order to avoid exposure to high powers. Two extreme values of f_{ZFC} are examined, each in the horizontal and vertical axes. An additional parameter d is included in the model to account for the displacement of the slit center from the beam propagation axis.

The beam radius at the slit position w_z is observed to lie in the range from 0.98 mm to 1.82 mm, which can be easily converted to the beam waist w_0 as

$$w_0 = \frac{\lambda f_{\text{L}}}{\pi w_z}, \quad (5)$$

and thus yields the measured range

$$56 \mu\text{m} \leq w_0 \leq 103 \mu\text{m}. \quad (6)$$

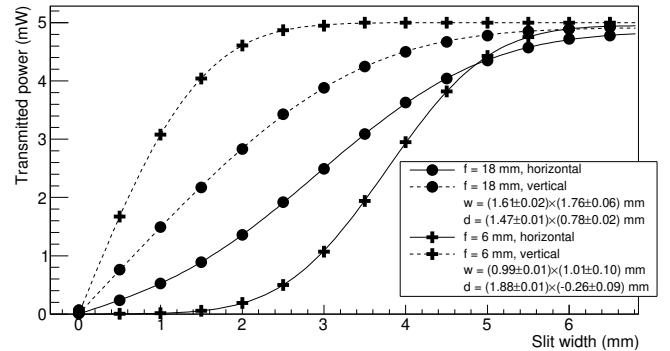


Figure 2: Results of the double knife edge measurement. Lines are fits to Eqs. 4 with an additional offset parameter d . Red and blue correspond to the two focal lengths of the ZFC f_{ZFC} , and solid and dotted correspond to the axis being measured. The displayed values of w are the measured beam radii at the slit position.

This shows that the optical system is properly configured to focus the beam, and the planned waist $w_0 \sim 60 \mu\text{m}$ is accessible. The wider end of the range seems to be thinner than the planned range (Eq. 2), which may be due to the shift of the beam axis when f_{L} is changed.

In conclusion, we have constructed an optical system that enables the generation of an optical lattice trap of depth 0.2 mK for the ^{210}Fr atom. This system is applicable for stable alkali atoms such as Rb and Cs, which will be used to study laser cooling and trapping techniques that would play an essential role in the high-sensitivity electron EDM search.

Acknowledgements

This work has been supported by JSR Fellowship, University of Tokyo, and JSPS KAKENHI grant number 21J12044.

References

- [1] T. E. Chupp, P. Fierlinger, M. J. Ramsey-Musolf, and J. T. Singh, *Rev. Mod. Phys.* **91** (2019) 015001.
- [2] N. Shitara, N. Yamanaka, B. K. Sahoo, T. Watanabe, and B. P. Das, *J. High Energ. Phys.* **2021** (2021) 124.
- [3] R. Grimm, M. Weidemüller, and Y. B. Ovchinnikov, *Adv. At. Mol. Opt. Phys.* **42** (2000) 95.
- [4] N. Ozawa, *et al.*, *CNS Annual Report 2021*, pp. 43–44 (2023).

Development of sustainable $^{24}\text{Mg}^{8+}$ beam production at HyperECR

K. Kamakura, Y. Kotaka, T. Nakagawa^a, J. Ohnishi^a, K. Hatanaka^b,
A. Goto^c, H. Yamaguchi, and Y. Sakemi

Center for Nuclear Study, Graduate School of Science, the University of Tokyo

^a*Nishina Center for Accelerator-Based Science, RIKEN*

^b*Research Center for Nuclear Physics, Osaka University*

^c*Institute of Materials Structure Science, KEK*

1. Introduction

In collaboration with the CRIB spectrometer group, we have been developing a magnesium beam that can be provided for long-term experiments.

CNS 14 GHz HyperECR ion source provides various metal ion beams to the RIKEN AVF cyclotron [1]. The magnesium beam was already been put to practical use, however, its intensity and sustainability had not met the requirements of the experiment group. Therefore, developments in beam production have been put forward. This report discusses two methods for $^{24}\text{Mg}^{8+}$ beam production.

2. Required Beam

The beam current required by the experiment group was 400 pA on target and the duration of the experiment was 10.5 days. Considering the beam transmission from the ion source to the target, the estimated minimum requirement of $^{24}\text{Mg}^{8+}$ beam current was 32 eμA at HyperECR Ion Source.

3. Off-axis Double Crucible

Firstly, the off-axis double crucible method was developed to maximize beam production. Powdered metal magnesium is stored in a couple of two-milliliter crucibles. Each has a single $\phi 1.6$ mm opening. They are placed off-centered against the optical axis as shown in Figure 1. This

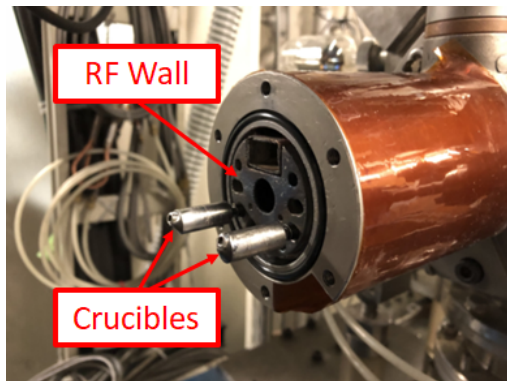


Figure 1: Off-axis double crucible method: In this picture, the plasma chamber is not attached and a couple of off-axis crucibles are exposed. When the whole apparatus is assembled, the RF wall makes the bottom of the plasma chamber. The longitudinal position of the crucibles is adjustable.

unique positioning of the crucibles avoids interfering with the ECR plasma that forms along the optical axis.

Using this method together with the strong-convergence extraction system [2], maximum $^{24}\text{Mg}^{8+}$ beam current of 65 eμA was achieved.

The duration of consecutive beam production is estimated to be around 12 days. However, the consumption rate of the magnesium sample can vary depending on ion source conditions, and it could be just short of 10.5 days of beam time and an additional one day of beam production that is necessary for tuning the ion source and the accelerator prior to the experiment. To replenish the sample, the vacuum inside the plasma chamber and extraction chamber should be broken, and the ion source has to be disassembled. It takes one whole day to reassemble, evacuate, and bake the plasma chamber to restore the beam production.

4. Axially Inserted Crucible

The axially inserted crucible method is developed to reduce the downtime for sample replenishment. A single sample crucible is inserted along the optical axis as shown in Figure 2. Unlike the double crucible method, it is possible to withdraw the crucible through an airlock behind the gas chamber without breaking the vacuum inside the plasma chamber. It allows us to refill the sample crucible with magnesium powder and resume beam production in approximately 3 hours. Moreover, it is easier to deal with troubles with the crucible during the experiments than with the off-axis crucible method. The maximum $^{24}\text{Mg}^{8+}$ beam

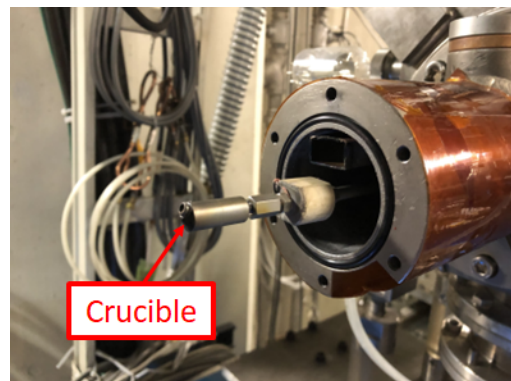


Figure 2: Axially inserted crucible method: A single crucible can be seen placed on the optical axis. RF wall is removed so that the crucible can be withdrawn from the airlock.

current was 40 eμA and 4 days of the consecutive beam was provided by single replenishment.

5. Summary

Two methods for $^{24}\text{Mg}^{8+}$ beam production have been developed. One can provide 65 eμA for 12 days, the other can provide 40 eμA virtually endlessly with 3 hours break every 4 days. In the experiment scheduled in January 2022, the latter method was chosen for sustainability and maintainability. The $^{24}\text{Mg}^{8+}$ beam was successfully produced for 18 days with four breaks to refill the sample crucible.

References

- [1] K. Kamakura *et al.*, CNS Annual Report 2020, 45-46 (2021).
- [2] Y. Ohshiro *et al.*, CNS Annual Report 2019, 53-54 (2020).

Current status of the development of the emittance monitor for high-intensity ion beams accelerated by AVF Cyclotron

Y. Kotaka, K. Kamakura, H. Yamaguchi, N. Imai, Y. Sakemi, J. Ohnishi^a, K. Hatanaka^b,

Center for Nuclear Study, Graduate School of Science, University of Tokyo

^a*RIKEN Nishina Center*

^b*Research Center for Nuclear Physics, Osaka University*

1. Introduction

There are 3 experimental courses in the E7 room of RIKEN Nishina Center. On these courses, the experimental equipments of CNS are installed. When the beam intensity is less than $10 \text{ e}\mu\text{A}$, the overall average beam transport efficiency of those courses is 73 %. However, when the beam intensity is larger than $10 \text{ e}\mu\text{A}$, the overall average beam transport efficiency drops to be 66 %. It is found that the stronger beam intensity tends to lower beam transport efficiency. For improving the beam transport efficiency, the optimization of the beam transport system is necessary. The decrease of the transport efficiency may be caused by the emittance growth. However, high intensity beam emittances cannot be measured by the existing emittance monitor because of the insufficiency of cooling power [1, 2].

We are developing the pepper-pot emittance monitor (PEM) [3, 4] for the high intensity beam. In this fiscal year, the analysis for the beam test, upgrade of optical system of digital camera, and the preparation of next beam test were reported.

2. Analysis of the performance test

The performance test of the prototype PEM was done with ion beam. We set the low performance camera at about $L=500 \text{ mm}$ distance from the window of the PEM. As the condition that entire region of fluorescent plate fitted in a camera view was not found, we decided to take the beam image on a part of fluorescent plate.

The exposed ion beam was $^{24}\text{Mg}^{8+}$ 7.5 MeV/u and the beam power was 23 W which was correspond to 1020 enA. The vector of average beam angles through the holes of pepper-pot mask is shown in Fig. 1. The captured area is from -10 to 20 mm in horizontal and from -17 to 6 mm in vertical because the camera optics cannot be regulated sufficiently. Nevertheless, we tried to analyze the measurements for the performance evaluation. Figure 2 shows the beam trajectory from every hole on the pepper-pot mask and Fig. 3 shows the reconstructed beam profiles at 4500 mm from PEM. Figure 2 and Fig. 3 are calculated by using the vector shown in Fig. 1. It is found that these beam trajectories have nodes at 2500 mm from PEM. But the nodes should be at around 4500 mm from PEM because the standard deviation (SD) of beam position distribution in the x and y directions are respectively 1.9 mm and 1.4 mm, which are calculated from beam profiles shown in Fig. 4 measured by profile monitor set 4500 mm behind the PEM. This may be caused by the measurement accuracy of beam angle. To see this assumption, we supposed the beam trajectory and beam emittance close to the real beam by use of the mea-

sured beam profile at 4500 mm from PEM and calculated the beam trajectory including the assumed beam angle accuracy so as to be close to the beam profile shown in Fig. 3. If the angle accuracy is 2 mrad and the other errors do not exist, Fig. 2 and Fig. 3 are accountable. Next time, we should have beam test after making the camera optics system to cover the entire area of the fluorescent plate.

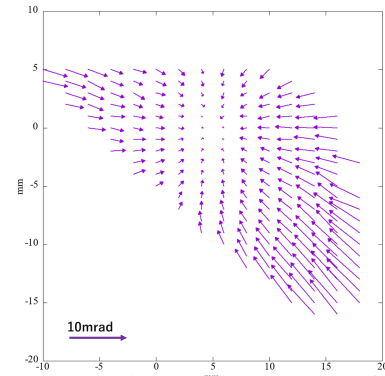


Figure 1: The angular vector at each position of beam through each hole of the pepper-pot mask.

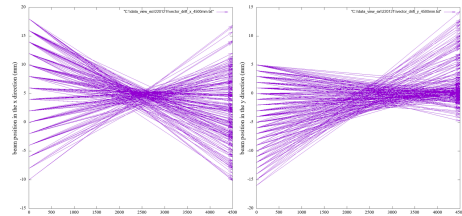


Figure 2: The beam trajectory to a point at 4500 mm from PEM. The left view is x direction and the right view is y direction.

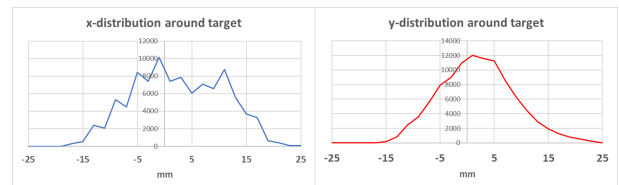


Figure 3: The reconstructed beam profile after transporting 4500 mm from PEM. The left image is x(mm) direction and the right image is y(mm) direction.

3. Optical system of digital camera

The study of the optical system with a tele lens to keep away from the deterioration by radiation is continued [5].

The required conditions for the optical system are to take an entire image of fluorescent plate and to suppress the dis-

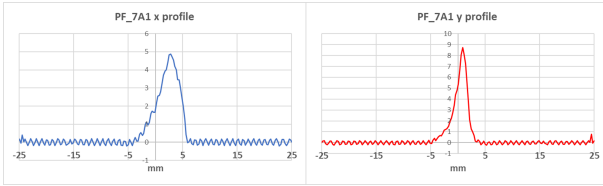


Figure 4: The measured beam profile by beam profile monitor at 4500 mm downstream PEM. The left image is for x (mm) direction and the right image is for y (mm) direction.

tortion of the image caused by lens aberration. This time, we arranged to use another PEM which has the 48 mm diameter of window to see the fluorescent plate. The diameter is namely extended 8 mm compared with the previous PEM. The focal length of tele lens used for study is 100 mm. An achromatizing lens was adopted for the intermediate lens of which focal length is 200 mm because it has an ability to expand the region of the image of fluorescent plate and suppress the distortion of image. The distance between the intermediate lens and window and the distance between digital camera and window are defined as d (m) and L (m), respectively.

The achieved L is 2200 mm, which is longer than last time. At this time, d is 410 mm, which is shorter than last time [5]. The image of fluorescent plate under this condition is shown in Fig. 5. We think L has possibility to expand if a tele lens with longer focal length can be introduced because Fig. 5 indicated the area of fluorescent plate is somewhat smaller than the area of image.

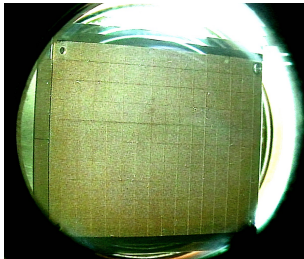


Figure 5: The image is fluorescent plate on condition that L is 2200 mm and d is 410 mm.

The distortion is indicated as the relationship between the fiducial (designed) positions and the difference from the positions on the image against fiducial (designed) positions shown in Fig. 6. The differences are caused by not only distortion, but the error made from drawing lines on the copper plate. The standard deviations of the difference on the horizontal and vertical directions are 0.16 mm and 0.14 mm, respectively.

4. The preparation of the next performance test

The performance test of the prototype PEM with the accelerated beam is planned. We have two required conditions for an accelerator and beam line. The first is that the beam energy is as low as beam can be stopped by a copper plate of which thickness is 0.1 mm. We want to see the difference of angle accuracy in terms of the different hole diameter of pepper-pot mask. The 0.1 mm and 0.3 mm hole diameter of pepper-pot masks are prepared. However, the pepper-pot

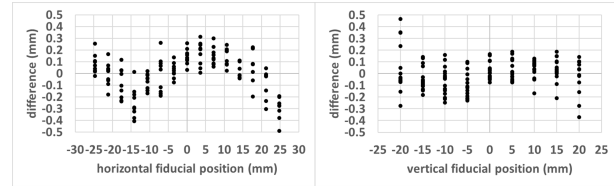


Figure 6: The left and right are the correlation between fiducial positions and the difference from the positions on the image against fiducial positions in the horizontal and vertical directions, respectively.

mask with 0.1 mm hole diameter is made by copper and the thickness is 0.1 mm. Therefore, we need low energy beam. The second is that at least two profile monitors are set in the same straight beam line as the PEM. The σ matrix of transverse beam component (x or y) are calculated statistically by use of 3 profile monitors. As the beam image of the PEM is regarded as profile monitor, two other profile monitors are required to estimate the σ matrix of transverse beam component. The estimated σ matrix is used as the reference which is thought to be correct. The performance of PEM is evaluated by comparing with the estimated σ matrix. One of accelerator facilities to meet our requires is Micro Analysis Laboratory, Tandem accelerator (MALT), The University of Tokyo [6] and we are preparing beam test there.

References

- [1] Y. Kotaka *et al.*, CNS Ann. Rep. 2020 (2022), p.43-44.
- [2] Y. Kotaka *et al.*, Proc. 18th Annual Meeting of PASJ, (2021), p.873-877.
- [3] L. E. Collins and P. T. Stroud, Nucl. Instr. and Meth. **26** (1964), p.157-166.
- [4] T. Hoffmann *et al.*, AIP Conf. Proc. **546**, 432 (2000).
- [5] Y. Kotaka *et al.*, CNS Ann. Rep. 2021 (2023), p.45-46.
- [6] <https://malt.um.u-tokyo.ac.jp/>

Theoretical Nuclear Physics

Gamow-Teller transition described by the Monte-Carlo shell model

K. Yanase^a, N. Shimizu^{a,b}, Y. Tsunoda^b, and Y. Utsuno^{a,c}

^aCenter for Nuclear Study, The University of Tokyo, Hongo Tokyo 113-0033, Japan

^bCenter for Computational Sciences, University of Tsukuba, Tsukuba 305-8577, Japan

^cAdvanced Science Research Center, Japan Atomic Energy Agency, Tokai, Ibaraki 319-1195, Japan

Most of the elements heavier than iron are produced through the rapid neutron capture process(r-process). The r-process path passes through the neutron-rich side of ^{132}Sn . We compute the low-energy nuclear properties contributing to the β -decay half lives by using the Monte-Carlo shell model (MCSM). In this paper, we focus on the southwest region of ^{132}Sn . We employ the same model space with the large-scale shell model calculation in Ref. [1], which consists of the five neutron orbitals between $N = 50$ and 82 and the nine proton orbitals between $Z = 28$ and 82. The effective interaction is taken from the SNV interaction and the remaining part is given by the phenomenological VMU interaction. Moreover, the monopole interaction strengths are decreased by 10% to reproduce the low-energy spectra as shown in Fig. 1.

The upper panel of Fig. 2 shows the Gamow-Teller transition strength of ^{130}Cd . In the MCSM calculation, we adopt several tens of basis vectors optimized for low-energy eigenstates. This prescription is not enough to reproduce the Gamow-Teller transition. We utilize an unitary transformation for the many-body bases to describe the states strongly connected to the ground state of the parent nucleus through the Gamow-Teller transition operator.

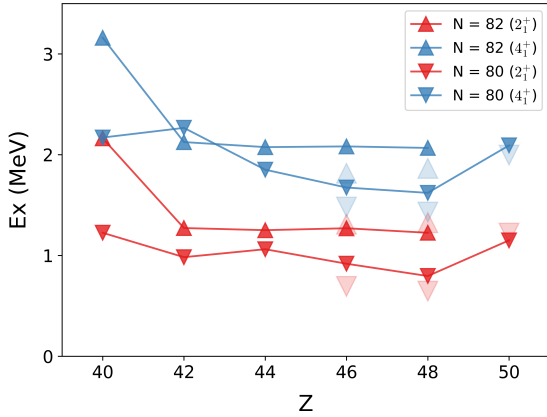


Figure 1: The energy spectra of $N = 80$ and 82 nuclei. The results of MCSM calculations are shown with filled symbols.

The Gamow-Teller transition operator is defined by

$$G_{\pm,\mu} = \sum_{a=1}^A \tau_{\pm}(a) \sigma_{\mu}(a), \quad (1)$$

where $\sigma_{\mu}(a)$ and $\tau_{\pm}(a)$ denote the spin and isospin opera-

tors, and $G_{+,\mu}^{\dagger} = G_{-,\mu}$. Using the commutation relations

$$\sum_{i,j=1}^3 [G_{+,i}, G_{-,j}] = \sum_{a=1}^A 2i\epsilon_{ijk} \sigma_k(a) \tau_+(a) \tau_-(a) + \sum_{a=1}^A \sigma_i(a) \sigma_j(a) \tau_z(a), \quad (2)$$

the sum rule is given as

$$\begin{aligned} & \sum_{\mu,\nu=0,\pm 1} \langle \psi_{J,M} | [G_{+,\mu}, G_{-,\nu}] | \psi_{J,M} \rangle \\ &= \sum_{i=1}^3 \langle \psi_{J,M} | G_{+,i} | \psi_n \rangle \langle \psi_n | G_{-,i} | \psi_{J,M} \rangle \\ & \quad - \sum_{i=1}^3 \langle \psi_{J,M} | G_{-,i} | \psi_n \rangle \langle \psi_n | G_{+,i} | \psi_{J,M} \rangle \\ &= 3(N - Z), \end{aligned} \quad (3)$$

where $|\psi_{J,M}\rangle$ is the ground state and $|\psi_n\rangle$ is the intermediate states of the daughter nucleus. Our goal is to construct a set of basis vectors $\{|\psi_n\rangle\}$ that almost exhausts the sum rule.

In the MCSM calculation, the ground state is expressed with deformed Slater determinants, one of which is given by

$$|\phi\rangle = \prod_{k=1}^{N_f} a_k^{\dagger} |-\rangle, \quad (4)$$

$$a_k^{\dagger} = \sum_{\alpha=1}^{N_{sp}} D_{\alpha k} c_{\alpha}^{\dagger}, \quad (5)$$

where $|-\rangle$ denotes the inert core occupied by a definite number of nucleons. The number of nucleons within the model space is N_f and the number of the single-particle states is N_{sp} .

The deformed Slater determinant is decomposed into the proton and neutron parts as

$$|\phi\rangle = |\phi^{(\pi)}\rangle \otimes |\phi^{(\nu)}\rangle, \quad (6)$$

where

$$|\phi^{(\tau)}\rangle = \prod_{k=1}^{N_{\tau}} a_{\tau,k}^{\dagger} |-\rangle, \quad (7)$$

$$a_{\tau,k}^{\dagger} = \sum_{\alpha=1}^{N_{sp}^{(\tau)}} D_{\alpha k}^{(\tau)} c_{\tau,\alpha}^{\dagger}, \quad (8)$$

for $\tau = \pi, \nu$. Using the QR decomposition algorithm, we can construct the $N_{sp}^{(\pi)} \times N_{sp}^{(\nu)}$ unitary matrix $\bar{D}^{(\tau)}$ extended

from $D^{(\tau)}$. The creation operator can then be extended for $k = 1, 2, \dots, N_{\text{sp}}^{(\tau)}$ as

$$a_{\tau,k}^\dagger = \sum_{\alpha=1}^{N_{\text{sp}}^{(\tau)}} \bar{D}_{\alpha k}^{(\tau)} c_{\tau,\alpha}^\dagger. \quad (9)$$

The Gamow-Teller operator can be expressed as

$$\begin{aligned} G_{-,\mu} &= \sum_{\alpha\beta} \langle \alpha | \tau_- \sigma_\mu | \beta \rangle c_\alpha^\dagger c_\beta \\ &= \sum_{i=1}^{N_{\text{sp}}^{(\pi)}} \sum_{j=1}^{N_{\text{sp}}^{(\nu)}} \langle \pi, i | \sigma_\mu | \nu, j \rangle a_{\pi,i}^\dagger a_{\nu,j}, \end{aligned} \quad (10)$$

where the one-body matrix elements for the new basis vectors are defined by

$$\langle \pi, i | \sigma_\mu | \nu, j \rangle = \sum_{\alpha\beta} \langle \pi, \alpha | \sigma_\mu | \nu, \beta \rangle \bar{D}_{\alpha i}^{(\pi)*} \bar{D}_{\beta j}^{(\nu)}. \quad (11)$$

Considering a basis vector $|\phi\rangle$,

$$G_{-,\mu} |\phi\rangle = \sum_{j=1}^{N_\nu} |\phi_{\mu j}\rangle, \quad (12)$$

where

$$|\phi_{\mu j}\rangle = \prod_{k=1}^{N_\pi} a_{\pi,k}^\dagger b_{\pi,\mu j}^\dagger \prod_{k(\neq j)}^{N_\nu} a_{\nu,k}^\dagger |-\rangle, \quad (13)$$

$$b_{\pi,\mu j}^\dagger = \sum_{\alpha=1}^{N_{\text{sp}}^{(\pi)}} B_{\mu,\alpha j}^{(\pi)} c_{\pi,\alpha}^\dagger, \quad (14)$$

$$B_{\mu,\alpha j}^{(\pi)} = (-1)^{j-1} \sum_{i=N_\pi+1}^{N_{\text{sp}}^{(\pi)}} \bar{D}_{\alpha i}^{(\pi)} \langle \pi, i | \sigma_\mu | \nu, j \rangle. \quad (15)$$

To completely satisfy the sum rule, we need the $3N_\nu$ basis vectors for each $|\phi\rangle$. The total dimension $3N_\nu \times N_{\text{g.s.}}$ becomes large as the number of basis vectors used to describe the ground state denoted by $N_{\text{g.s.}}$. We should economize the computational costs by selecting a small number of basis vectors that almost satisfy the sum rule.

When the ground state is expressed with only one basis vector, the sum rule is given by

$$\langle \phi | G_{+,\mu} G_{-,\mu} | \phi \rangle = \sum_{i,j=1}^{N_\nu} \langle \phi_{\mu i} | \phi_{\mu j} \rangle. \quad (16)$$

This is conserved with the unitary transformation of the neutron single-particle levels

$$\begin{aligned} \sum_{j=1}^{N_\nu} |\phi_{\mu j}\rangle &= \det(U) \sum_{j=1}^{N_\nu} |\phi_{\mu j}\rangle \\ &= \sum_{j=1}^{N_\nu} |\phi'_{\mu j}\rangle. \end{aligned} \quad (17)$$

We utilize the unitary matrix U to diagonalize the matrix (16), and adopt 50 bases from the largest eigenvalue. The lower panel of Fig. 2 shows the Gamow-Teller transition strengths obtained by this prescription, where the sum rule is almost satisfied.

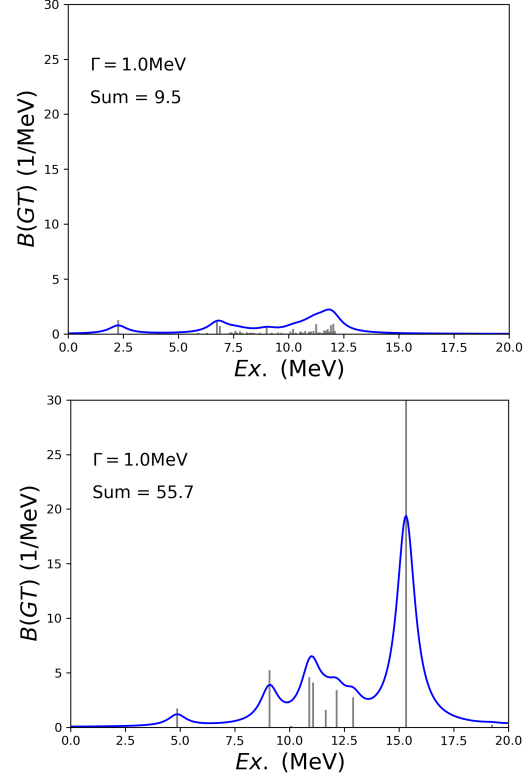


Figure 2: The Gamow-Teller transition strength of ^{130}Cd . The blue lines are the folded strength functions by a Lorentzian function with 1 MeV width.

References

- [1] N. Shimizu, T. Togashi, and Y. Utsuno, PTEP **2021** (2021) 033D01.

Other Activities

The 21th CNS International Summer School CNSSS22

N. Aoi^a, T. Gunji, N. Imai, H. Liang^{b,c}, S. Michimasa, H. Nagahama, T. Otsuka^b, H. Sakai^b, Y. Sakemi, H. Sakurai^{b,c}, N. Shimizu, S. Shimoura, H. Ueno^b, T. Uesaka^b, Y. Utsuno^d, T. Wakasa^e, K. Yako, H. Yamaguchi, K. Yoneda

Center for Nuclear Study, Graduate School of Science, University of Tokyo

^a*RCNP, Osaka University*

^b*RIKEN Nishina Center*

^c*Department of Physics, Univ. of Tokyo*

^d*Advanced Science Research Center, Japan Atomic Energy Agency*

^e*Super Heavy Element Center, Kyushu University*

The 21st CNS International Summer School (CNSSS22) was hosted by the Center for Nuclear Study (CNS) from August 20th to 24th, 2022. The school was co-organized by the JSPS A3-Foresight program and the Super Heavy Element Center at Kyushu University. It received support from the RIKEN Nishina Center and the Research Council of Norway, and was cooperated by the Asian Nuclear Physics Association (ANPhA). The school aimed at fostering graduate students and postdocs by providing basic knowledge and perspectives of nuclear physics.

It is noteworthy that Oslo University joined the organization for the first time. Eleven people participated in the school in-person from Oslo University.

However, due to the Japanese government's anti-COVID measures, we were unable to invite participants from certain Asian countries. Consequently, we opted for a hybrid-style event following two online schools in 2020 and 2021. Additionally, because the University required special anti-measures for in-person meetings on campus, we held the school at Shinrin-koen Heritage Resort. This marked the first time the school was conducted outside the University and RIKEN campus.

As part of our own anti-COVID measures, participants were required to report their body temperatures starting from one week before the school and continuing until its conclusion. Additionally, prior to attending the school, participants had to provide evidence of a negative result from a COVID antibody test. CNS provided the participants with antibody test kits before the start of the school.

The school commenced with a welcome address from Prof. Masahiro Hoshino, the Dean of the School of Science at the University of Tokyo. The program featured lectures delivered by prominent scientists specializing in both experimental and theoretical nuclear physics. Each lecture commenced with a foundational overview and concluded with discussions on the latest developments in the respective field.

The list of the lecturers and the title of lectures are following:

- Prof. Stefan Frauendorf (Nortre Dome USA), (on-line), "Quantal Rotation"
- Prof. Shunsuke Kurosawa (Tohoku Univ, Japan), "Scintillation counter"
- Prof. Satoshi N. Nakamura (Univ. of Tokyo, Japan),

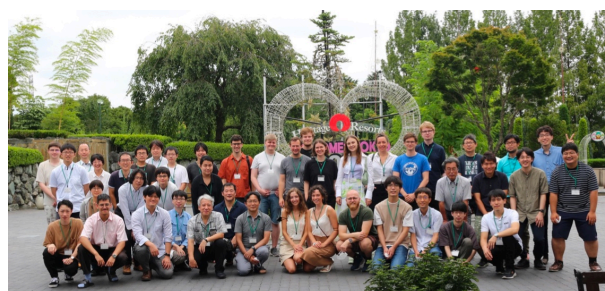


Figure 1: A group photos of the participants of CNSSS22 with the lecturers.

"Hypernuclei"

- Prof. Sunniva Siem (Univ. of Oslo), (on-line), "Experimental Level densities and Photon strength functions, and medical application of nuclear physics"
- Dr. Vetle Ingeberg (Univ of Oslo), "Oslo method"
- Prof. Angela Bracco (Univ. of Milano), (on-line), "Physics with AGATA"
- Dr. Shintaro Go (RIKEN, Japan), "Overview of RIBF/Spectroscopy of exotic nuclei"
- Prof. Yutaka Utsuno (JAEA/CNS, Japan), "Large-scale shell-model calculations: from low-lying spectra to compound states"

Eight lecturers and ninety-nine participants registered at the school. Fifty-one participants attended the school in person, while, similar to the past two years, there were online participants from Malaysia, Vietnam, Korea, China, and India. Each class lasted for 50 minutes, with 10-minute breaks between sessions. The actual average number of participants, including online attendees, was around 70. Figure 1 is a group photo of the in-person participants with the lecturers.

As is tradition, there were three "Young Scientist Sessions" during which graduate students and postdocs delivered oral presentations. In total, there were fourteen oral presentations. Since 2017, the CNSSS Young Scientist Awards (CNSSSYS Awards) have been introduced to recognize outstanding presentations. A few winners were selected from each Young Scientist Session by the members of the organizing committee and the lecturers. The recipients of the third CNSSSYS Awards were:

- Ms. Azusa Inoue (RCNP, Osaka University) “Study of the contribution of the ${}^7\text{Be}(d, p)$ reaction to the ${}^7\text{Li}$ problem in the Big-Bang Nucleosynthesis ”
- Mr. George Hadson-Chang (RIKEN/Univ. of Surrey) “A position sensitive Schottky cavity doublet for use in the Rare RI Ring”

The certificate of the awards were presented to them from the school master, Prof. Sakemi.

The best presenter among them, Ms. Azusa Inoue, was also honored with the APPS-DNP/ANPhA Prize for Young Physicists, sponsored by AAPPS-DNP/ANPhA. She received a certificate as well as the prize money, presented by Prof. W. Liu, the chair of ANPhA.

We are grateful for the support from ANPhA. We extend our thanks to the administrative staff of CNS for their valuable assistance. We also appreciate the dedication of the graduate students and postdocs at CNS for their hard work. Finally, we acknowledge the contributions of all the lecturers and participants to the success of CNSSS22.

Laboratory Exercise for Undergraduate Students

H. Nagahama, S. Nagao^a, K. Yako, S. N. Nakamura^a, M. Fukase, K. Okawa, K. Kawata, R. Mizuno^{a,b}, K. Kokubun^{a,b}, S. Michimasa, N. Imai, Y. Yamaguchi, H. Sakemi, and M. Niikura^b

Center for Nuclear Study, Graduate School of Science, University of Tokyo

^a*Department of Physics, University of Tokyo*

^b*RIKEN Nishina Center*

Nuclear scattering experiments were performed as a laboratory exercise for undergraduate students of the University of Tokyo. This program was aiming at providing undergraduate students with an opportunity to learn how to study subatomic physics by using an ion beam from an accelerator. In 2022, 32 students attended this program.

Four beam times were scheduled in the second semester for third-year students, and 8 students participated in each beam time. The experiments were performed at the RIBF using a 26-MeV alpha beam accelerated by the AVF cyclotron. The alpha beam extracted from the AVF cyclotron was transported to the E7B beam line in the E7 experimental hall. The scattering chamber has two separate target ports which enable us to perform two independent experiments without opening the chamber during the beam time. In each beam time, the students were divided into two groups and took one of the following two subjects:

1. Measurement of elastic scattering of incident alpha particle with ^{197}Au , to learn how to determine nuclear size.
2. Measurement of gamma rays emitted from the cascade decay of highly excited ^{154}Gd and ^{184}Os , to learn the nuclear deformation.

Before the experiment, the students took a course on the basic handling of the semiconductor detectors and electronic circuits at the Hongo campus, and attended a radiation safety lecture at RIKEN. CNS conducted tours to the RI beam factory for the students.

In the $\alpha+^{197}\text{Au}$ measurement, α particles scattered with the Au target with a thickness of $1\ \mu\text{m}$ were detected using a silicon PIN-diode located 15-cm away from the target. A collimator with a diameter of 6 mm was attached on the silicon detector. The energy spectrum of the scattered α particles was recorded by a multi-channel analyzer (MCA) system. The beam was stopped by a Faraday cup located downstream of the scattering chamber. The cross section for the alpha elastic scattering was measured in the angular range of $\theta_{\text{lab}} = 20\text{--}150^\circ$.

The measured cross section was compared with the calculated cross section of the Rutherford scattering. The cross section was also analyzed by the potential model calculation, and the radius of the ^{197}Au nucleus was discussed. Some students obtained the radius of ~ 10 fm by using a classical model where the trajectory of the α particle in the nuclear potential is obtained using the Runge-Kutta method. Others tried to understand the scattering process by calculating the angular distribution using the distorted wave Born

approximation method with a Coulomb wave function and a realistic nuclear potential.

In the measurement of gamma rays, excited states in ^{154}Gd and ^{184}Os nuclei were populated by the $^{152}\text{Sm}(\alpha,2n)$ and $^{182}\text{W}(\alpha,2n)$ reactions, respectively. The gamma rays emitted from the cascade decay of the rotational bands were measured by a high-purity germanium detector located 30-cm away from the target. The energy of the gamma ray were recorded by the MCA system. The gain and the efficiency of the detector system had been calibrated using standard gamma-ray sources of ^{60}Co , ^{133}Ba , and ^{137}Cs . The gamma rays from the 10^+ and 8^+ states in ^{154}Gd and ^{184}Os , respectively, were successfully identified. Based on the energies of the gamma rays, the moment of inertia and the deformation parameters of the excited states were discussed by using a classical rigid rotor model and a irrotational fluid model. The students found that the reality lies between the two extreme models. The initial population among the levels in the rotational band was also discussed by taking the effect of the internal conversion into account.

It was the first time for most of the students to use large experimental equipments. They learned basic things about the experimental nuclear physics and how to extract physics from the data. We believe this program was very impressive for the students. The authors would like to thank Dr. K. Tanaka, the CNS accelerator group, and the RIBF cyclotron crew for their helpful effort in the present program.

Appendices

Symposium, Workshop, Seminar, and PAC

CNS Reports

Publication List

Talks and Presentations

Awards, Press Releases, and Others

Personnel

Symposium, Workshop, Seminar, and PAC

A. Symposium and Workshop

1. OEDO/SHARAQ collaboration meeting 2022
online, August 30, 2022.
2. International Symposium on Nuclear Spectroscopy for Extreme Quantum Systems (NUSPEQ2023)
Plaza Verde, Shizuoka, March 3–7, 2022.

B. CNS Seminar

1. CNS seminar + NSS #570 (Dr. Javier Menéndez)
Date: December 22, 2022

C. Program Advisory Committee for Nuclear-Physics Experiments at RI Beam Factory

1. The 23rd NP-PAC meeting
Date: December 5–7, 2022

CNS Reports

#101 “CNS Annual Report 2021”
Edited by H. Nagahama
March, 2023

Publication List

A. Original Papers

1. L. Yang, C.J. Lin, H. Yamaguchi, A.M. Moro, N.R. Ma, D.X. Wang, K.J. Cook, M. Mazzocco, P.W. Wen, S. Hayakawa, J.S. Wang, Y.Y. Yang, G.L. Zhang, Z. Huang, A. Inoue, H.M. Jia, D. Kahl, A. Kim, M.S. Kwag, M. L. Commara, G.M. Gu, S. Okamoto, C. Parascandolo, D. Pierrousakou, H. Shimizu, H.H. Sun, M.L. Wang, F. Yang, F.P. Zhong, “Breakup of the proton halo nucleus ^8B near barrier energies”, *Nature Communications* **13** 7193 (2022).
2. N. J. Abdulameer *et al.* [PHENIX], “Improving constraints on gluon spin-momentum correlations in transversely polarized protons via midrapidity open-heavy-flavor electrons in $p\uparrow+p$ collisions at $\sqrt{s}=200$ GeV,” *Phys. Rev. D* **107**, no.5, 052012 (2023)
3. N. J. Abdulameer *et al.* [PHENIX], “Low- p_T direct-photon production in Au+Au collisions at $s_{NN}=39$ and 62.4 GeV,” *Phys. Rev. C* **107**, no.2, 024914 (2023)
4. N. J. Abdulameer *et al.* [PHENIX], “Measurements of second-harmonic Fourier coefficients from azimuthal anisotropies in $p+p$, $p+\text{Au}$, $d+\text{Au}$, and He^3+Au collisions at $\sqrt{s_{NN}}=200$ GeV,” *Phys. Rev. C* **107**, no.2, 024907 (2023)
5. U. Acharya *et al.* [PHENIX], “Study of ϕ -meson production in $p+\text{Al}$, $p+\text{Au}$, $d+\text{Au}$, and $^3\text{He}+\text{Au}$ collisions at $\sqrt{s_{NN}} = 200$ GeV,” *Phys. Rev. C* **106**, no.1, 014908 (2022)
6. U. A. Acharya *et al.* [PHENIX], “Measurement of $\psi(2S)$ nuclear modification at backward and forward rapidity in $p + p$, $p + \text{Al}$, and $p + \text{Au}$ collisions at $\sqrt{s_{NN}} = 200$ GeV,” *Phys. Rev. C* **105**, no.6, 064912 (2022)
7. S. Acharya *et al.* [ALICE], “Measurement of anti- ^3He nuclei absorption in matter and impact on their propagation in the Galaxy,” *Nature Phys.* **19**, no.1, 61-71 (2023)
8. S. Acharya *et al.* [ALICE], “Multiplicity dependence of charged-particle jet production in pp collisions at $\sqrt{s} = 13$ TeV,” *Eur. Phys. J. C* **82**, no.6, 514 (2022)
9. S. Acharya *et al.* [ALICE], “Measurement of beauty production via non-prompt D^0 mesons in Pb-Pb collisions at $\sqrt{s_{NN}}= 5.02$ TeV,” *JHEP* **12**, 126 (2022)
10. S. Acharya *et al.* [ALICE], “First study of the two-body scattering involving charm hadrons,” *Phys. Rev. D* **106**, no.5, 052010 (2022)
11. S. Acharya *et al.* [ALICE], “Forward rapidity J/ψ production as a function of charged-particle multiplicity in pp collisions at $\sqrt{s} = 5.02$ and 13 TeV,” *JHEP* **06**, 015 (2022)
12. S. Acharya *et al.* [ALICE], “Neutral to charged kaon yield fluctuations in Pb – Pb collisions at $s_{NN}=2.76$ TeV,” *Phys. Lett. B* **832**, 137242 (2022)
13. U. A. Acharya *et al.* [PHENIX], “Transverse-single-spin asymmetries of charged pions at midrapidity in transversely polarized $p+p$ collisions at $\sqrt{s} = 200$ GeV,” *Phys. Rev. D* **105**, no.3, 032003 (2022)
14. S. Acharya *et al.* [ALICE], “Production of light (anti)nuclei in pp collisions at $\sqrt{s} = 5.02$ TeV,” *Eur. Phys. J. C* **82**, no.4, 289 (2022)
15. S. Acharya *et al.* [ALICE], “Observation of a multiplicity dependence in the p_T -differential charm baryon-to-meson ratios in proton-proton collisions at $\sqrt{s} = 13$ TeV,” *Phys. Lett. B* **829**, 137065 (2022)
16. S. Acharya *et al.* [ALICE], “KS0KS0 and KS0K \pm femtoscopy in pp collisions at $s=5.02$ and 13 TeV,” *Phys. Lett. B* **833**, 137335 (2022)
17. S. Acharya *et al.* [ALICE], “Characterizing the initial conditions of heavy-ion collisions at the LHC with mean transverse momentum and anisotropic flow correlations,” *Phys. Lett. B* **834**, 137393 (2022)

18. U. A. Acharya *et al.* [PHENIX], “Systematic study of nuclear effects in $p + \text{Al}$, $p + \text{Au}$, $d + \text{Au}$, and ${}^3\text{He} + \text{Au}$ collisions at $\sqrt{s_{\text{NN}}} = 200$ GeV using π^0 production,” *Phys. Rev. C* **105**, no.6, 064902 (2022)
19. S. Acharya *et al.* [ALICE], “Investigating charm production and fragmentation via azimuthal correlations of prompt D mesons with charged particles in pp collisions at $\sqrt{s} = 13$ TeV,” *Eur. Phys. J. C* **82**, no.4, 335 (2022)
20. S. Acharya *et al.* [ALICE], “Measurement of prompt D_s^+ -meson production and azimuthal anisotropy in Pb–Pb collisions at $\sqrt{s_{\text{NN}}}=5.02$ TeV,” *Phys. Lett. B* **827**, 136986 (2022)
21. S. Acharya *et al.* [ALICE], “Prompt D^0 , D^+ , and D^{*+} production in Pb–Pb collisions at $\sqrt{s_{\text{NN}}} = 5.02$ TeV,” *JHEP* **01**, 174 (2022)
22. U. A. Acharya *et al.* [PHENIX], “Transverse single spin asymmetries of forward neutrons in $p + p$, $p + \text{Al}$ and $p + \text{Au}$ collisions at $\sqrt{s_{\text{NN}}} = 200$ GeV as a function of transverse and longitudinal momenta,” *Phys. Rev. D* **105**, no.3, 032004 (2022)
23. S. Acharya *et al.* [ALICE], “General balance functions of identified charged hadron pairs of $(\pi, \text{K}, \text{p})$ in Pb–Pb collisions at $s_{\text{NN}}=2.76$ TeV,” *Phys. Lett. B* **833**, 137338 (2022)
24. S. Acharya *et al.* [ALICE], “Measurement of inclusive charged-particle b-jet production in pp and p-Pb collisions at $\sqrt{s_{\text{NN}}} = 5.02$ TeV,” *JHEP* **01**, 178 (2022)
25. S. Acharya *et al.* [ALICE], “Inclusive quarkonium production in pp collisions at $\sqrt{s} = 5.02$ TeV,” *Eur. Phys. J. C* **83**, no.1, 61 (2023)
26. S. Acharya *et al.* [ALICE], “Production of light (anti)nuclei in pp collisions at $\sqrt{s} = 13$ TeV,” *JHEP* **01**, 106 (2022)
27. S. Acharya *et al.* [ALICE], “Prompt and non-prompt J/ψ production cross sections at midrapidity in proton-proton collisions at $\sqrt{s} = 5.02$ and 13 TeV,” *JHEP* **03**, 190 (2022)
28. S. Acharya *et al.* [A Large Ion Collider Experiment and ALICE], “Measurement of the groomed jet radius and momentum splitting fraction in pp and Pb–Pb collisions at $\sqrt{s_{\text{NN}}} = 5.02$ TeV,” *Phys. Rev. Lett.* **128**, no.10, 102001 (2022)
29. S. Acharya *et al.* [ALICE], “Measurements of the groomed and ungroomed jet angularities in pp collisions at $\sqrt{s} = 5.02$ TeV,” *JHEP* **05**, 061 (2022)
30. S. Acharya *et al.* [ALICE], “Polarization of Λ and $\bar{\Lambda}$ Hyperons along the Beam Direction in Pb-Pb Collisions at $\sqrt{s_{\text{NN}}}=5.02$ TeV,” *Phys. Rev. Lett.* **128**, no.17, 172005 (2022)
31. S. Acharya *et al.* [A Large Ion Collider Experiment and ALICE], “Hypertriton Production in p-Pb Collisions at $\sqrt{s_{\text{NN}}}=5.02$ TeV,” *Phys. Rev. Lett.* **128**, no.25, 252003 (2022)
32. S. Acharya *et al.* [ALICE], “Study of very forward energy and its correlation with particle production at midrapidity in pp and p-Pb collisions at the LHC,” *JHEP* **08**, 086 (2022)
33. U. A. Acharya *et al.* [PHENIX], “Kinematic dependence of azimuthal anisotropies in $p + \text{Au}$, $d + \text{Au}$, and ${}^3\text{He} + \text{Au}$ at $\sqrt{s_{\text{NN}}} = 200$ GeV,” *Phys. Rev. C* **105**, no.2, 024901 (2022)
34. S. Acharya *et al.* [ALICE], “Production of $K^*(892)^0$ and $\phi(1020)$ in pp and Pb-Pb collisions at $\sqrt{s_{\text{NN}}} = 5.02$ TeV,” *Phys. Rev. C* **106**, no.3, 034907 (2022)
35. S. Acharya *et al.* [ALICE], “Direct observation of the dead-cone effect in quantum chromodynamics,” *Nature* **605**, no.7910, 440-446 (2022) [erratum: *Nature* **607**, no.7920, E22 (2022)]
36. S. Acharya *et al.* [ALICE], “Measurement of Prompt D^0 , Λ_c^+ , and $\Sigma_c^{0,++}(2455)$ Production in Proton–Proton Collisions at $\sqrt{s} = 13$ TeV,” *Phys. Rev. Lett.* **128**, no.1, 012001 (2022)
37. S. Acharya *et al.* [ALICE], “Charm-quark fragmentation fractions and production cross section at midrapidity in pp collisions at the LHC,” *Phys. Rev. D* **105**, no.1, L011103 (2022)
38. S. Acharya *et al.* [ALICE], “Measurement of $K^*(892)^\pm$ production in inelastic pp collisions at the LHC,” *Phys. Lett. B* **828**, 137013 (2022)

39. S. Acharya *et al.* [ALICE], “Inclusive, prompt and non-prompt J/ψ production at midrapidity in p-Pb collisions at $\sqrt{s_{NN}} = 5.02$ TeV,” JHEP **06**, 011 (2022)
40. S. Acharya *et al.* [ALICE], “Investigating the role of strangeness in baryon–antibaryon annihilation at the LHC,” Phys. Lett. B **829**, 137060 (2022)
41. S. Acharya *et al.* [ALICE], “Production of Λ and K_s^0 in jets in p–Pb collisions at $\sqrt{s_{NN}}=5.02$ TeV and pp collisions at $\sqrt{s}=7$ TeV,” Phys. Lett. B **827**, 136984 (2022)
42. S. Acharya *et al.* [ALICE], “Exploring the $N\Lambda$ – $N\Sigma$ coupled system with high precision correlation techniques at the LHC,” Phys. Lett. B **833**, 137272 (2022)
43. S. Acharya *et al.* [ALICE], “Nuclear modification factor of light neutral-meson spectra up to high transverse momentum in p–Pb collisions at $\sqrt{s_{NN}}=8.16$ TeV,” Phys. Lett. B **827**, 136943 (2022)
44. T. Otsuka, T. Abe, T. Yoshida, Y. Tsunoda, N. Shimizu, N. Itagaki, Y. Utsuno, J. Vary, P. Maris, and H. Ueno, “ α -Clustering in atomic nuclei from first principles with statistical learning and the hoyle state character,” Nat. Commun. **13**, 2234 (2022).
45. E. Ideguchi, T. Kibedi, J. Dowie, H. T. Hoang, Kumar Raju M., G. Lane, L. Bignell, T. K. Eriksen, A. J. Mitchell, A. Akber, B. Combes, B. McCormik, T. Gray, A. Stuchbery, N. Shimizu, and Y. Utsuno, “Electric monopole transition from the superdeformed band in ^{40}Ca ,” Phys. Rev. Lett. **128**, 252501 (2022).
46. N. Shimizu and Y. Tsunoda, “SO(3) quadratures in angular-momentum projection,” Comput. Phys. Commun. **283**, 108583 (2022).
47. D. Little, A. D. Ayangeakaa, R. V. F. Janssens, S. Zhu, Y. Tsunoda, T. Otsuka, B. A. Brown, M. P. Carpenter, A. Gade, D. Rhodes, C. R. Hoffman, F. G. Kondev, T. Lauritsen, D. Seweryniak, J. Wu, J. Henderson, C. Y. Wu, P. Chowdhury, P. C. Bender, A. M. Forney, and W. B. Walters, “Multistep Coulomb excitation of ^{64}Ni : Shape coexistence and nature of low-spin excitations,” Phys. Rev. C **106**, 044313 (2022).
48. V. Tripathi, S. Bhattacharya, E. Rubino, C. Benetti, J. F. Perello, S. L. Tabor, S. N. Liddick, P. C. Bender, M. P. Carpenter, J. J. Carroll, A. Chester, C. J. Chiara, K. Childers, B. R. Clark, B. P. Crider, J. T. Harke, B. Longfellow, R. S. Lubna, S. Luitel, T. H. Ogunbeku, A. L. Richard, S. Saha, N. Shimizu, O. A. Shehu, Y. Utsuno, R. Unz, Y. Xiao, S. Yoshida, and Y. Zhu, “ β^- decay of exotic P and S isotopes with neutron number near 28,” Phys. Rev. C **106**, 064314 (2022).
49. A. Revel, J. Wu, H. Iwasaki, J. Ash, D. Bazin, B. A. Brown, J. Chen, R. Elder, P. Farris, A. Gade, M. Grindler, N. Kobayashi, J. Li, B. Longfellow, T. Mijatovic, J. Pereira, A. Poves, A. Sanchez, N. Shimizu, M. Spieker, Y. Utsuno, and D. Weisshaar, “Large collectivity in ^{29}Ne at the boundary of the island of inversion,” Phys. Lett. B **838**, 137704 (2023).
50. J. A. Lay, A. Vitturi, L. Fortunato, Y. Tsunoda, T. Togashi, and T. Otsuka, “Two-particle transfer processes as a signature of shape phase transition in Zirconium isotopes,” Phys. Lett. B **838**, 137719 (2023).
51. H.F. Li, S. Naimi, T.M. Sprouse, M.R. Mumpower, Y. Abe, Y. Yamaguchi, D. Nagae, F. Suzaki, M. Wakasugi, H. Arakawa, W.B. Dou, D. Hamakawa, S. Hosoi, Y. Inada, D. Kajiki, T. Kobayashi, M. Sakaue, Y. Yokoda, T. Yamaguchi, R. Kagesawa, D. Kamioka, T. Moriguchi, M. Mukai, A. Ozawa, S. Ota, N. Kitamura, S. Masuoka, S. Michimasa, H. Baba, N. Fukuda, Y. Shimizu, H. Suzuki, H. Takeda, D.S. Ahn, M. Wang, C.Y. Fu, Q. Wang, S. Suzuki, Z. Ge, Yu.A. Litvinov, G. Lorusso, P.M. Walker, Zs. Podolyak, and T. Uesaka, “First Application of Mass Measurements with the Rare-RI Ring Reveals the Solar r-Process Abundance Trend at $A = 122$ and $A = 123$,” Phys. Rev. Lett. **128**, 152701 (2022)
52. S. Iimura, M. Rosenbusch, A. Takamine, Y. Tsunoda, M. Wada, S. Chen, D.S. Hou, W. Xian, H. Ishiyama, S. Yan, P. Schury, H. Crawford, P. Doornenbal, Y. Hirayama, Y. Ito, S. Kimura, T. Koiwai, T.M. Kojima, H. Koura, J. Lee, J. Liu, S. Michimasa, H. Miyatake, J.Y. Moon, S. Naimi, S. Nishimura, T. Niwase, A. Odahara, T. Otsuka, S. Paschalis, M. Petri, N. Shimizu, T. Sonoda, D. Suzuki, Y.X. Watanabe, K. Wimmer, and H. Wollnik, “Study of the $N=32$ and $N=34$ Shell Gap for Ti and V by the First High-Precision Multireflection Time-of-Flight Mass Measurements at BigRIPS-SLOWRI,” Phys. Rev. Lett. **130**, 012501 (2023)

53. T. Nishi, K. Itahashi, D.S. Ahn, G.P.A. Berg, M. Dozono, D. Etoh, H. Fujioka, N. Fukuda, N. Fukunishi, H. Geisel, E. Haettner, T. Hashimoto, R.S. Hayano, S. Hirenzaki, H. Horii, N. Ikeno, N. Inabe, M. Iwasaki, D. Kameda, K. Kisamori, Y. Kiyokawa, T. Kubo, K. Kusaka, M. Matsushita, and piAF Collaboration “Chiral symmetry restoration at high matter density observed in pionic atoms,” *Nat. Phys.* (2023). <https://doi.org/10.1038/s41567-023-02001-x>
54. M. Rosenbusch, M. Wada, S. Chen, A. Takamine, S. Iimura, D. Hou, W. Xian, S. Yan, P. Schury, Y. Hirayama, Y. Ito, H. Ishiyama, S. Kimura, T. Kojima, J. Lee, J. Liu, S. Michimasa, H. Miyatake J.Y. Moon M. Mukai S. Naimi S. Nishimura T. Niwase T. Sonoda Y.X. Watanabe and H. Wollnik “The new MRTOF mass spectrograph following the ZeroDegree spectrometer at RIKEN ’ s RIBF facility,” *Nuclear Inst. and Methods in Physics Research, A* 1047 (2023) 167824.
55. D. Piatti, E. Masha, M. Aliotta, J. Balibrea-Correa, F. Barile, D. Bemmerer, A. Best, A. Boeltzig, C. Brogini, C.G. Bruno, A. Caciolli, F. Cavanna, T. Chillery, G.F. Ciani, A. Compagnucci, P. Corvisiero, L. Csedreki, T. Davinson, R. Depalo, A. di Leva, Z. Elekes, F. Ferraro, E.M. Fiore, A. Formicola, Zs. Fülöp, G. Gervino, A. Guglielmetti, C. Gustavino, Gy. Gyürky, G. Imbriani, M. Junker, M. Lugaro, P. Marigo, R. Menegazzo, V. Mossa, F.R. Pantaleo, V. Paticchio, R. Perrino, P. Prati, D. Rapagnani, L. Schiavulli, J. Skowronski, K. Stöckel, O. Straniero, T. Szücs, M.P. Takács, S. Zavatarelli, “First direct limit on the 334 keV resonance strength in $^{22}\text{Ne}(\alpha,\gamma)^{26}\text{Mg}$ reaction,” *Eur. Phys. J A* **58**, 194 (2022).
56. L. Lalanne, O. Sorlin, A. Poves, M. Assié, F. Hammache, S. Koyama, D. Suzuki, F. Flavigny, V. Girard-Alcindor, A. Lemasson, A. Matta, T. Roger, D. Beaumel, Y. Blumenfeld, B. A. Brown, F. De Oliveira Santos, F. Delaunay, N. de Séreville, S. Franchoo, J. Gibelin, J. Guillot, O. Kamalou, N. Kitamura, V. Lapoux, B. Mauss, P. Morfouace, M. Niikura, J. Pancin, T. Y. Saito, C. Stodel, and J-C. Thomas, “Structure of ^{36}Ca under the Coulomb Magnifying Glass,” *Phys. Rev. Lett.* **129**, 122501 (2022).
57. N. Ozawa, H. Nagahama, and Y. Sakemi, “Francium ion source with novel methods of target heating and beam characterization,” *Rev. Sci. Instrum.* **94**, 023306 (2023).
58. K. S. Tanaka, K. Harada, T. Hayamizu, R. Kita, R. Kono, K. Maruta, H. Nagahama, N. Ozawa, Y. Sakemi, and R. Sugimori, “An accelerator experiment for junior and senior high school students to improve students’ involvement in fundamental physics,” *Phys. Edu.* **57**, 045013 (2022).
59. 早川勢也, 山口英斉, 梶野敏貴, 「ビッグバン元素合成—『トロイの木馬法』で迫る『リチウム問題』」, *日本物理学会誌* **77**, 547–552 (2022).
60. N. Shimizu, “Recent Progress of Shell-Model Calculations, Monte Carlo Shell Model, and Quasi-Particle Vacua Shell Model,” *Physics* **4**, 1081 (2022).
61. Y. Utsuno, “Probing different characteristics of shell evolution driven by central, spin-orbit, and tensor forces,” *Physics* **4**, 185–201 (2022).

B. Proceedings

1. Xingqun Yao, Motohiko Kusakabe, Toshitaka Kajino, Silvio Cherubini, Seiya Hayakawa, Hidetoshi Yamaguchi, “Supernova nucleosynthesis, radioactive nuclear reactions and neutrino-mass hierarchy”, *EPJ Web Conf.* **260**, 01007 (2022).
2. H. Yamaguchi, S. Hayakawa, N.R. Ma, H. Shimizu, K. Okawa, L. Yang, D. Kahl, M. La Cognata, L. Lamia, K. Abe, O. Beliuskina, S.M. Cha, K.Y. Chae, S. Cherubini, P. Figuera, Z. Ge, M. Gulino, J. Hu, A. Inoue, N. Iwasa, A. Kim, D. Kim, G. Kiss, S. Kubono, M. La Commara, M. Lattuada, E.J. Lee, J.Y. Moon, S. Palmerini, C. Parascandolo, S.Y. Park, V.H. Phong, D. Pierrousakou, R.G. Pizzone, G.G. Rapisarda, S. Romano, C. Spitaleri, X.D. Tang, O. Trippella, A. Tumino, N.T. Zhang, Y.H. Lam, A. Heger, A.M. Jacobs, S.W. Xu, S.B. Ma, L.H. Ru, E.Q. Liu, T. Liu, C.B. Hamill, A. St J. Murphy, J. Su, X. Fang, M.S. Kwag, N.N. Duy, N.K. Uyen, D.H. Kim, J. Liang, A. Psaltis, M. Sferrazza, Z. Johnston, Y.Y. Li, “Experimental studies on astrophysical reactions at the low-energy RI beam separator CRIB”, *EPJ Web Conf.* **260**, 03003 (2022).

3. J. Hu, H. Yamaguchi, Y.H. Lam, A. Heger, D. Kahl, A.M. Jacobs, Z. Johnston, S.W. Xu, N.T. Zhang, S.B. Ma, L.H. Ru, E.Q. Liu, T. Liu, S. Hayakawa, L. Yang, H. Shimizu, C.B. Hamill, A. St J. Murphy, J. Su, X. Fang, K.Y. Chae, M.S. Kwag, S.M. Cha, N.N. Duy, N.K. Uyen, N.K. Kim, D.H., R.G. Pizzone, M. La Cognata, S. Cherubini, S. Romano, A. Tumino, J. Liang, A. Psaltis, M. Sferrazza, D. Kim, Y.Y. Li, S. Kubono, “First measurement of $^{25}\text{Al}+p$ resonant scattering relevant to the astrophysical reaction $^{22}\text{Mg}(\alpha, p)^{25}\text{Al}$ ”, EPJ Web Conf. **260**, 05001 (2022).
4. M. L. Sergi, L. Lamia, G. G. Rapisarda, M. Mazzocco, S. Cherubini, G. D’Agata, A. Di Pietro, J. P. Fernandez-Garcia, P. Figuera, M. Fisichella, G. L. Guardo, M. Gulino, S. Hayakawa, M. La Cognata, M. Lattuada, A. A. Oliva, S. Palmerini, R. G. Pizzone, S. M.R. Puglia, S. Romano, R. Sparta, C. Spitaleri, D. Torresi, and A. Tumino, “Trojan Horse Method for n-induced reaction investigations at astrophysical energies”, in *Particles and Nuclei International Conference 2021 (PANIC2021)*, Proc. of Science, **380**, 342, (2022).
5. H. Yamaguchi, S. Hayakawa, N.R. Ma, H. Shimizu, K. Okawa, Q. Zhang, L. Yang, D. Kahl, M. La Cognata, L. Lamia, K. Abe, O. Beliuskina, S.M. Cha, K.Y. Chae, S. Cherubini, P. Figuera, Z. Ge, M. Gulino, J. Hu, A. Inoue, N. Iwasa, A. Kim, D. Kim, G. Kiss, S. Kubono, M. La Commara, M. Lattuada, E.J. Lee, J.Y. Moon, S. Palmerini, C. Parascandolo, S.Y. Park, V.H. Phong, D. Pierrotsakou, R.G. Pizzone, G.G. Rapisarda, S. Romano, C. Spitaleri, X.D. Tang, O. Trippella, A. Tumino, N.T. Zhang, Y.H. Lam, A. Heger, A.M. Jacobs, S.W. Xu, S.B. Ma, L.H. Ru, E.Q. Liu, T. Liu, C.B. Hamill, A. St J. Murphy, J. Su, X. Fang, M.S. Kwag, N.N. Duy, N.K. Uyen, D.H. Kim, J. Liang, A. Psaltis, M. Sferrazza, Z. Johnston, Y.Y. Li, “RIB induced reactions: Studying astrophysical reactions with low-energy RI beam at CRIB”, EPJ Web Conf. **275**, 01015 (2023).
6. Kodai Okawa, Minju Kim, Kyungyuk Chae, Seiya Hayakawa, Satoshi Adachi, Soomi Cha, Thomas William Chillery, Tatsuya Furuno, Gyungmo Gu, Shutaro Hanai, Nobuaki Imai, David Kahl, Takahiro Kawabata, Chan-hee Kim, Dahee Kim, Sohyun Kim, Shigeru Kubono, Minsik Kwag, Jiatai Li, Nanru Ma, Shin’ichiro Michimasa, Uyen Nguyen Kim, Duy Nguyen Ngoc, Kohsuke Sakanashi, Hideki Shimizu, Oana Sirbu, Hidetoshi Yamaguchi, Rin Yokoyama, Qian Zhang, “Direct measurement of the $^{26}\text{Si}(\alpha, p)^{29}\text{P}$ reaction at CRIB for the nucleosynthesis in the x-ray bursts”, EPJ Web Conf. **275**, 02009 (2023).
7. H. Murakami for the ALICE Collaboration, “Thermal radiation and direct photon production measurements with dielectrons in Pb–Pb and pp collisions,” Strangeness in Quark Matter (SQM 2022), Jun. 13-17, 2022, Busan, Korea, EPJ Web of Conferences 276, 06011 (2023)
8. D. Sekihata for the ALICE Collaboration, “Thermal radiation and direct photon production in Pb–Pb and pp collisions with dielectrons in ALICE,” International Conference on High Energy Physics, July. 06-13, 2022, Bologna, Italy, PoS(ICHEP2022)452
9. Shutaro Hanai, Shinsuke Ota, Reiko Kojima, Masanori Dozono, Nobuaki. Imai, Shin’ichiro Michimasa, Susumu Shimoura, Juzo Zenihiro, Kento Inaba, and Yuto Hijikata “DEVELOPMENT OF FAST-RESPONSE TRACKING DETECTOR FOR HIGH-INTENSITY ION BEAMS,” RADIATION DETECTORS AND THEIR USES Proceedings of the 36th Workshop on Radiation Detectors and Their Uses in KEK, pp.24–34, 2023.
10. S. Motoki, Y. Kazeki, N. Hiroki, O. Naoya, N. Shintaro, N. Teruhito, U. Daisuke, F. Mirai, N. Keisuke, H. Tomohiro, H. Hiromitsu, S. Yasuhiro, and M. Yasuyuki, “Development of Neutralization Apparatus and Francium Source for the Francium Electric Dipole Moment Search,” JPS Conf. Proc. **37**, 20605 (2022).
11. K. Nakamura, S. Nagase, T. Nakashita, T. Hayamizu, T. Aoki, H. Nagahama, N. Ozawa, M. Sato, K. Yamane, M. Fukase, D. Uehara, A. Takamine, and Y. Sakemi, “Development of a Laser Frequency Stabilization and an Optical Transmission System for the Francium Electric Dipole Moment Search,” J. Phys. Conf. Ser **2249**, 012010 (2022).

C. Theses

1. D. Uehara: “Study of neutral desorption reactions on metal surface for realization of laser cooled neutral francium source” Master thesis, the University of Tokyo, March 2021.
2. M. Fukase: “Development of a radio frequency dipole mass filter for the francium permanent electric dipole moment search” Master thesis, the University of Tokyo, March 2021.

3. N. Ozawa: “Source of cold francium atoms aimed at a search for the permanent electric dipole moment” PhD thesis, the University of Tokyo, March 2022.

Talks and Presentations

A. International Conference

1. H. Yamaguchi (oral, invited), “RIB induced reactions: Studying astrophysical reactions with low-energy RI beam at CRIB”, The 11th European Summer School on Experimental Nuclear Astrophysics (Santa Tecla School, ESSENA 2022), INFN-LNS, Catania, Italy, June 12–19, 2022.
2. H. Yamaguchi (oral, invited), “New evaluation of $^{22}\text{Mg}(\alpha, p)$ reaction rate and X-ray burst light curve”, UKAKUREN-RCNP Conference on AstroNuclear Physics (ANP2022), Osaka University, Toyonaka, Osaka, Japan, July 20–21, 2022.
3. H. Yamaguchi (oral, invited), “Big-Bang Li problem and nuclear reactions”, International Workshop “Origin of Elements and Cosmic Evolution: From Big-Bang to Supernovae and Mergers” (OECE2022), Beihang University, Beijing, China, Jul. 20–22, 2022.
4. S. Hayakawa (oral, invited), “New measurement of the $^7\text{Be} + n$ reactions and its impact on the primordial ^7Li abundance”, The 16th International Symposium on Origin of Matter and Evolution of Galaxies (OMEG16), Hanoi, Vietnam, Oct. 24–28, 2022.
5. H. Yamaguchi (oral, invited), “Studies on RI-involving astrophysical reactions at CRIB”, ECT* Workshop “Key Reactions in Nuclear Astrophysics”, ECT*, Trento, Italy, Dec. 12–16, 2022.
6. H. Yamaguchi (oral), 「X線バーストにおける重要不安定核反応の実験的検証 / Experimental investigation of relevant unstable-nucleus reactions in X-ray bursts」, RIBF ULIC Mini Workshop-39 星の進化と爆発天体における核反応の物理 (Physics of nuclear reactions in stellar evolution and explosive stellar objects), RIKEN, Wako, Saitama, Japan, February 20–21, 2023.
7. K. Okawa (poster), “Direct measurement of the $^{26}\text{Si}(\alpha, p)^{29}\text{P}$ reaction for the nucleosynthesis in the X-ray bursts,” FoPM International Symposium, Ito International Research Center, Hongo Campus, February 6–8, 2023.
8. S. Hayakawa (oral), “Nuclear astrophysics at the low-energy RI beam separator CRIB,” RIBF Users Meeting 2022, Web meeting hosted by RIKEN, Wako, Saitama, Japan, September 7–9, 2022.
9. T. Gunji (invited) for the ALICE Collaboration, “Recent results from the ALICE experiment at the LHC and its future prospects,” The 15th Asia Pacific Physics Conference (APPC15), August 21–26, online
10. T. Gunji (invited), “Hunting for dark photons,” GSI EMMI RRTF, Real and virtual photon production at ultra-low transverse momentum and low mass at LHC, 8/1–8/5, GSI
11. T. Gunji (invited), “High-energy nuclear physics in Japan and view on EIC,” EIC Asia Workshop, 3/16–3/18, RIKEN
12. H. Murakami for the ALICE collaboration, “Thermal radiation and direct photon production in Pb–Pb and pp collisions with dielectrons,” Strangeness in Quark Matter (SQM 2022), hybrid, Jun. 13–17, 2022, Busan, Korea
13. D. Sekihata for the ALICE collaboration, “Thermal radiation and direct photon production in Pb–Pb and pp collisions with dielectrons in ALICE,” International Conference on High Energy Physics, July. 06–13, 2022, Bologna, Italy
14. Y. Utsuno (invited), “Recent findings about shell evolution in the neutron-rich Ca region,” RIKEN Workshop on Physics of RI: Recent Progress and Perspectives, Wako, Japan, May 30–June 1, 2022.
15. Y. Utsuno (invited), “Large-scale shell-model calculations: from low-lying spectra to compound states,” A3F-CNS Summer School 2022, Kumagaya, Japan, August 20–24, 2022.
16. Y. Utsuno (invited), “Overview of shell-model results for the 3rd SEASTAR campaign,” REIMEI Workshop on Unveiling nuclear shells and correlations in exotic nuclei through knockout reactions, Darmstadt, Germany, October 10–12, 2022.
17. K. Yanase (oral), “Theoretical uncertainty on the nuclear Schiff moments of ^{129}Xe and ^{199}Hg ,” The 14th International Workshop on Fundamental Physics Using Atoms (FPUA2022), Fukuoka, Japan, November 24–25, 2022.

18. Y. Utsuno, N. Shimizu, and Y. Tsunoda (invited), “Large-scale shell-model approach to nuclear collective motion,” 66th DAE Symposium on Nuclear Physics, Guwahati, India, December 1–5, 2022.
19. K. Yanase (invited), “Shell-model study for the Nuclear Schiff moments of ^{129}Xe and ^{199}Hg ,” KMI workshop: Searches for Electric Dipole Moments: From Theory to Experiment, Nagoya, Japan, March 2–4, 2023.
20. Y. Utsuno (invited), “The nuclear shell model,” INTPART School 2023, Onna, Japan, February 20–March 7, 2023.
21. S. Michimasa (invited) “Direct mass measurements around neutron-rich Ca region at SHARAQ,” Physics of RI: Recent progress and perspectives RIKEN Nishina Center, Saitama, Japan, May 30 – June 1, 2022.
22. S. Michimasa (invited) “Present Status of OEDO/FY2020-2022” OEDO/SHARAQ collaboration meeting 2022, Web meeting hosted by CNS, Wako, Saitama, Japan, Aug. 30, 2022.
23. N. Imai (invited) “SHARAQ18” OEDO/SHARAQ collaboration meeting 2022, Aug. 30, 2022, Web meeting hosted by CNS, Wako, Saitama, Japan.
24. S. Hanai (invited) “SHARAQ13” OEDO/SHARAQ collaboration meeting 2022, Web meeting hosted by CNS, Wako, Saitama, Japan, Aug. 30, 2022.
25. S. Michimasa (invited) “OEDO-SHARAQ system: multifaceted performances in low-energy RI production and high-resolution spectroscopy,” The 19th International Conference on Electromagnetic Isotope Separators and Related Topics (EMIS XIX), RISP/IBS, Daejeon, Korea, Oct. 3–7, 2022.
26. S. Michimasa (invited) “Mass measurements of exotic nuclei at OEDO-SHARAQ,” The International Symposium on Nuclear Spectroscopy for Extreme Quantum Systems (NUSPEQ2023), Numazu, Sizuoka, Japan, Mar. 7–9, 2023.
27. T. Chillery (poster) “Treating Radioactive Waste: Measurement of $^{93}\text{Zr}+d$ Reactions at 30 MeV/u,” The International Symposium on Nuclear Spectroscopy for Extreme Quantum Systems (NUSPEQ2023), Numazu, Sizuoka, Japan, Mar. 7–9, 2023.
28. N. Kitamura (poster) “In-beam γ -ray spectroscopy of ^{32}Mg ” The International Symposium on Nuclear Spectroscopy for Extreme Quantum Systems (NUSPEQ2023), Numazu, Sizuoka, Japan, Mar. 7–9, 2023.
29. R. Yokoyama (poster) “New implantation detectors for decay spectroscopy at fragmentation facilities” The International Symposium on Nuclear Spectroscopy for Extreme Quantum Systems (NUSPEQ2023), Numazu, Sizuoka, Japan, Mar. 7–9, 2023.
30. S. Hanai (poster) “Direct mass measurement of neutron-deficient Fe isotopes” The International Symposium on Nuclear Spectroscopy for Extreme Quantum Systems (NUSPEQ2023), Numazu, Sizuoka, Japan, Mar. 7–9, 2023.
31. J. Li (poster) “Study of heavy-ion fusion reactions in inverse kinematic systems using low-energy ^{136}Xe beam,” The International Symposium on Nuclear Spectroscopy for Extreme Quantum Systems, Numazu, Sizuoka, Japan, Mar. 7–9, 2023.
32. S. Hanai (invited) “Direct measurement of the masses of Fe isotopes around the proton dripline,” RIBF users meeting, Web meeting hosted by RIKEN Nishina Center, Wako, Saitama, Japan, Sep. 22, 2022.
33. T. Chillery (invited) “Recent Studies on Heavy-Isotope Nucleosynthesis Using (d,p) Transfer Reactions at OEDO-SHARAQ,” RIBF users meeting, Web meeting hosted by RIKEN Nishina Center, Wako, Saitama, Japan, Sep. 22, 2022.
34. J.T. Li (oral), “Study of the fusion reaction in inverse kinematics with the low-energy ^{136}Xe beams,” UT-Tsinghua University Joint mini workshop, Tsinghua University, Beijing, China, Mar. 13, 2023.
35. S. Hanai (poster) “Development of a fast response PPAC for high-intensity heavy-ion beams,” The 19th International Conference on Electromagnetic Isotope Separators and Related Topics (EMIS XIX), RISP/IBS, Daejeon, Korea, Oct. 3–7, 2022.
36. K. Yako (oral), “Double and single charge exchange reactions on ^{48}Ca by ^{12}C beam at 250A MeV,” YKIS2022b, Kyoto, May 23–27, 2022.

37. A. Sakaue (poster), “The Search for double Gamow–Teller giant resonance at RIBF BigRIPS,” Annual meeting of A3 Foresight Program, Nuclear Physics in the 21st century, Osaka, February 13–15, 2023.
38. A. Sakaue (poster), “The search for double Gamow–Teller giant resonance with the ($^{12}\text{C}, ^{12}\text{Be}(0_2^+)$) reaction,” NUSPEQ2023, Numazu, March 7–9, 2023.
K. Kawata (poster), “The production of high-spin isomers around ^{52}Fe in fragmentation reaction of ^{58}Ni and ^{59}Co beams at 350 MeV/u,” NUSPEQ2023, Numazu, March 7–9, 2023.
39. K. Nakamura (oral), “400-m-Long Polarization-Maintaining Fibers for Magneto-Optical Trapping of Francium Atoms,” The 15th Pacific Rim Conference on Lasers and Electro-Optics (CLEO-PR 2022), Online, Aug 2, 2022.
40. H. Nagahama (invited), “Searching for the permanent electric dipole moment using laser cooled francium atoms,” 6th Workshop on the Physics of fundamental Symmetries and Interactions at low energies and the precision frontier (PSI2022), Paul Scherrer Institute, Switzerland, October 19, 2022.
41. M. Fukase (invited), “Search for permanent EDM by using Fr atoms,” 14th International Workshop on Fundamental Physics Using Atoms (FPUA2022), Kyushu University, Fukuoka, Japan, November 24, 2022.

B. Domestic Conference

1. 鎌倉恵太 (ポスター発表), 「14 GHz Hyper ECR イオン源を用いた ECR プラズマの研究」, 第 19 回日本加速器学会年会, オンライン講演, 2022 年 10 月 18–21 日
2. 大川皓大 (口頭発表), 「X 線バースト中の元素合成における $^{26}\text{Si}(\alpha, p)^{29}\text{P}$ 反応の直接測定」, 日本物理学会 2022 年秋季大会, 岡山理科大, 2022 年 9 月 6–8 日.
3. S. Hayakawa (oral), “Activity report of CRIB”, RIBF Users Meeting 2022, Session 3, オンライン開催, 2022 年 9 月.
4. 早川勢也 (口頭発表), “Measurement of the $^7\text{Be} + n$ reactions by Trojan Horse method updating primordial ^7Li abundance”, 宇宙核物理の展開 UKAKUREN-RCNP Conference on AstroNuclear Physics (ANP2022), , 大阪大学-オンラインハイブリッド開催, 2022 年 7 月.
5. 山口英斉 (口頭発表), 「軽い原子核の直鎖クラスター状態の実験的検証」, シンポジウム「原子核クラスター物理の新たな進展と展望」, 日本物理学会 2023 年春季大会, オンライン, 2023 年 3 月 25 日.
6. H. Murakami for the ALICE collaboration, “Direct photon production in proton-proton collisions at $\sqrt{s_{\text{NN}}} = 13$ TeV via interanl conversion technique with ALICE,” 日本物理学会 2022 年秋季大会 岡山理科大学 (岡山キャンパス)
7. 関畑大貴, 「電磁・ソフトプローブを通じた QGP 物理の結果と展望」, 2023 年 3 月 22 日 日本物理学会 2023 年春季大会 (online) 実験核物理・理論核物理領域 合同シンポジウム: 次世代の高エネルギー原子核衝突: 何が理解され、何を理解すべきか?
8. 馬場仁志 for the ALICE collaboration, 「機械学習を用いた、ALICE-TPC 検出器における空間電荷効果の補正」, 日本物理学会 2022 年秋季大会 岡山理科大学 (岡山キャンパス)
9. T. Gunji (invited), “Future Prospects of Quark Cluster Physics using ultra-relativistic heavy-ions,” 第 8 回クラスター階層領域研究会, 2023 年 2 月 9 日-2 月 11 日, 大阪大学吹田キャンパス接合科学研究所
10. T. Gunji (invited), 「LHC-ALICE 実験の新しいデータ収集系」, RCNP 研究会「原子核実験の次世代データ収集システム基盤開発にむけて」, 2022 年 5 月 16–17 日, 大阪大学吹田キャンパス
11. T. Gunji (invited), 「WG4 (オンラインフィルタリング・演算加速器) 報告と展望」, 原子核実験の先端データ収集システム—標準化と将来—, 2023 年 3 月 17 日
12. T. Gunji (invited), 「ALICE 実験における Vertex Trackers」, シリコンプラットフォーム研究会, KEK, 2022 年 8 月 9 日
13. 宇都野穰 (招待講演), 「大規模殻模型計算—現実的な原子核構造を得るには」, 研究会「宇宙核物理の展開」, 大阪府豊中市 (大阪大学), 2022 年 7 月 19–21 日.

14. 宇都野穰, 清水則孝, 井手口栄治, 青井考 (口頭発表), 「大規模殻模型計算と3準位模型による ^{40}Ca の超変形状態からのE0遷移の理解」, 日本物理学会 2022 年秋季大会, 岡山県岡山市 (岡山理科大学), 2022 年 9 月 6-8 日.
15. 柳瀬宏太 (招待講演), 「原子核殻模型によるキセノン原子核の核行列要素の理論計算」, 二重ベータ崩壊核行列要素実験理論合同研究会, 大阪府吹田市 (大阪大学核物理研究センター), 2022 年 10 月 3-4 日.
16. 柳瀬宏太, 清水則孝, 角田佑介, 宇都野穰 (口頭発表), 「モンテカルロ殻模型による $N=82$ 付近のベータ崩壊半減期の理論計算」, 日本物理学会 2023 年春季大会, オンライン, 2023 年 3 月 22-25 日.
17. N. Kitamura (invited), 「高性能波形ディジタイザの需要調査と今後の開発方針」, 原子核実験の先端データ収集システム—標準化と将来—, 大阪大学核物理研究センター, Mar. 17, 2023
18. R. Yokoyama (invited), 「原子核の複数粒子放出過程」, 第四回若手放談会, エキゾチック核物理の未来, 理研神戸・融合連携イノベーション推進棟, Mar. 15-17, 2023
19. R. Yokoyama (invited), 「核破碎・分裂反応式不安定核生成施設における β 核分光のためのシンチレーション検出器」, Scintillator for Medical, Astroparticle and Environmental Radiation Technologies, Tokushima University, Dec. 17-19, 2022.
20. N. Imai (invited), “Study of the neutron capture rate on the unstable nuclei via the surrogate reactions,” Workshop for the nucleosynthesis in the universe from the neutron capture, University of Tokyo, Tokyo, Japan, Feb. 9 – 10, 2023.
21. T. Chillery (oral), “Measurement of $^{130}\text{Sn}(d,p)$ Reaction for Neutron-Capture Rate in r-process Nucleosynthesis,” JPS Autumn 2022 meeting, Okayama, Sept. 6-8, 2022.
22. 阪上朱音 (口頭発表), 「 $(^{12}\text{C}, ^{12}\text{Be}(0_2^+))$ 反応を用いた二重ガモフ・テラー巨大共鳴状態の探索」, 日本物理学会 2022 年秋季大会, 岡山理科大学, 2022 年 9 月 6-8 日.

C. Lectures

1. Y. Sakemi, H. Yamaguchi: “Nuclear Physics III”, Summer, 2022.
2. K. Yako (with M. Ishino): “Experimental Techniques in Particle and Nuclear Physics”, Autumn, 2022.
3. H. Yamaguchi: “Hadron Physics” at Rikkyo University, Summer, 2022.
4. T. Gunji: “Physics Seminar”, Autumn, 2022.
5. K. Yako: “Classical Mechanics A for Undergraduate Students”, Summer, 2022.
6. H. Nagahamas, K. Yako: “Physics Experiment II”, Autumn, 2022.
7. H. Yamaguchi, T. Gunji, S. Michimasa: “Experience Seminar for Freshmen and Sophomore”, Autumn, 2022.

D. Awards

1. S. Hanai, ANPha award in The International Symposium on Nuclear Spectroscopy for Extreme Quantum Systems (NUSPEQ2023), Numazu, Sizuoka, Japan, Mar. 7–9, 2023.
2. A. Sakaue, Poster award for young scientists, Annual meeting of A3 Foresight Program, Nuclear Physics in the 21st century, Osaka, February 13–15, 2023.

Press Releases

Personnel

Director

SAKEMI, Yasuhiro

*Professor, Graduate School of Science
Center for Nuclear Study*

Scientific Staff

YAKO, Kentaro

Associate Professor

IMAI, Nobuaki

Associate Professor

GUNJI, Taku

Associate Professor

YAMAGUCHI, Hidetoshi

Lecturer

MICHIMASA, Shin'ichiro

Assistant Professor

NAGAHAMA, Hiroki

Assistant Professor

KITAMURA, Noritaka

Assistant Professor

Visiting Scientists

UTSUNO, Yutaka

JAEA

NISHIMURA, Daiki

Tokyo City University

KAJINO, Toshitaka

NAOJ

HAMAMOTO, Ikuko

Lund University

HWANG, Jongwon

IBS

NAKAGAWA, Takahide

RIKEN

SHIMOURA, Susumu

RIKEN

SHIMIZU, Noritaka

University of Tsukuba

OTA, Shinsuke

RCNP

DOZONO, Masanori

Kyoto University

Technical Specialist

KOTAKA, Yasuteru

Technical Assistant

YAGYU, Masayoshi

Project Research Associates

HAYAKAWA, Seiya

SEKIHATA, Daiki

YOKOYAMA, Rin

Post Doctoral Associates

NAKAMURA, Keisuke

KAMAKURA, Keita

MA, Nanru

YANASE, Kota

CHILLERY, Thomas William

SAITO, Takeshi

Academic Specialist

KOJIMA, Reiko

Assistant Teaching Staff

SEKIGUCHI, Yuko

KAWATA, Keita

SAKAUE, Akane

MASUOKA, Shoichiro

MURAKAMI, Hikari

Graduate Students

SHIMIZU, Hideki

OZAWA, Naoya

HANAI, Shutaro

NAGASE, Shintaro

KOHARA, Ryotaro

LI, Jiatai

UEHARA, Daisuke

OKAWA, Kodai

BABA, Hitoshi

FUKASE, Mirai

SINDO, Shujiro

Administration Staff

SHIMANE, Noriko

YAMAMOTO, Ikuko

KOTAKA, Aki

KISHI, Yukino

Committees

Steering Committee

HOSHINO, Masahiro	<i>Department of Earth and Planetary Physics, Graduate School of Science, UT</i>
YAMAMOTO, Satoshi	<i>Department of Physics, Graduate School of Science, UT</i>
OGATA, Masao	<i>Department of Physics, Graduate School of Science, UT</i>
NAKAMURA, Satoshi N.	<i>Department of Physics, Graduate School of Science, UT</i>
WAKASA, Tomotsugu	<i>Department of Physics, Graduate School of Science, Kyushu University</i>
MORI, Toshinori	<i>International Center for Elementary Particle Physics, UT</i>
TAKAHASHI, Hiroyuki	<i>Department of Nuclear Engineering and Management, Graduate School of Engineering, UT</i>
SAKEMI, Yasuhiro	<i>Center for Nuclear Study, Graduate School of Science, UT</i>
YAKO, Kentaro	<i>Center for Nuclear Study, Graduate School of Science, UT</i>

